Structure and Function of Human Metabolic Enzyme IMP Dehydrogenase

Anika Lauren Burrell

A dissertation

submitted in partial fulfillment of the

requirements for the degree of

Doctor of Philosophy

University of Washington

2022

Reading Committee:

Justin M. Kollman, Chair

Alexander R. Paredez

Neil P. King

Program Authorized to Offer Degree:

Biochemistry

University of Washington

Abstract

Structure and Function of Human Metabolic Enzyme IMP Dehydrogenase

Anika Lauren Burrell

Chair of the Supervisory Committee:
Justin M. Kollman
Biochemistry

Many essential metabolic enzymes self-assemble into filamentous polymers which serve as a layer of allosteric regulation. One example is the highly conserved enzyme Inosine-5'-monophosphate dehydrogenase (IMPDH) that catalyzes the first committed step in GTP synthesis and dynamically forms filamentous ultrastructures in response to metabolic demands. The human IMPDH1 isoform is of particular interest because mutations in IMPDH1 lead to blindness in humans. Although IMPDH1 has two unique splice variants in the retina, very little is known about how the retinal variants are structurally or allosterically different from the canonical variant. A series of cryo-EM structures that demonstrate how the retinal splice variants control filament assembly to tune allosteric regulation. We also develop a transgenic zebrafish model to study IMPDH1-associated blindness. We anticipate these findings to be a foundation for understanding how mutations in the enzyme IMPDH1 lead to retinal degeneration in humans. Furthermore, we have shown that a well-established means of metabolic regulation - tissue-specific splice variants - can add an additional layer of allosteric regulation on top of filament assembly to finely tune complex enzyme regulation.

Acknowledgements

I am incredibly grateful to my thesis advisor and mentor, Dr. Justin Kollman - for his guidance, support, and always challenging me to be a better scientist. I will forever appreciate your dedication to the importance of pastels and lack of trapped white space. You have shown me how to always ask engaging questions, the importance of celebrating successes, but most of all how to be a good boss. I would like to thank the past and present members of the Kollman Laboratory for their encouragement, clever ideas, and thoughtful questions. Specifically Joel Quispe and Drs. Matthew Johnson, Eric Lynch, Kelli Hvorecny, John Calise, Sasha Dickinson for always taking the time to teach. I would also like to thank Dr. Susan Brockerhoff for welcoming into your lab and along with Drs. Whitney Cleghorn and Michelle Giarmarco for showing me how to be a diligent and productive scientist. Also, I am extremely fortunate to have joined the Ultimate frisbee community during graduate school, they provide me the balance, challenge, and support I need to be a thoughtful and driven scientist. Finally, words will never be enough to thank my parents and my partner Roy. Mom and Dad, you have always made sure every door is open to me and supported me in every path I have chosen - thank you for everything.

List of Figures

Supplemental

List of Tables

Supplemental

Chapter 1: Introduction

1.1 Metabolic Filaments

Classically, intermediate metabolism has been viewed as a kind of soup of enzymes and substrates, partially organized by sequestration into membrane-bound compartments and limited primarily by diffusion within those compartments. More recently, however, a significant level of physical organization of intermediate metabolism has been uncovered, where dynamic reorganization of enzymes into discrete cellular structures is linked to changes in metabolic conditions. These structures include multienzyme aggregates that colocalize different enzymes in a pathway, and filamentous polymers that form by self-assembly of a single enzyme[1,2].

Several dozen different metabolic enzymes are now known to form filamentous polymers in cells (for a comprehensive recent review, see[3,4]). Among the best described of these metabolic filaments are inosine-5′-monophosphate dehydrogenase (IMPDH) and CTP synthase (CTPS), key regulatory enzymes in the purine and pyrimidine nucleotide biosynthesis pathways, respectively. Here, we focus on IMPDH.

How metabolic enzyme polymerization arose during evolution is not well understood. However, theoretical and experimental models suggest that single amino acid alterations can be sufficient to drive otherwise diffuse enzymes to assemble[5,6]. This may be especially true for metabolic enzymes, which are frequently homo-oligomeric proteins, and therefore the effect of individual mutations can be amplified by their presence in each subunit. Indeed, many proteins, and particularly metabolic enzymes, have been found to form large assemblies in proteomic and imaging-based screens in yeast[7–10].

1.2 Physiological role of IMPDH

IMPDH is an essential enzyme in purine biosynthesis where it catalyzes the first committed step in GTP synthesis (Fig. 1.1a). The enzyme converts inosine-5′-monophosphate (IMP) to xanthosine monophosphate (XMP) using NAD^+ as a cofactor through a multi-step catalysis reaction that requires major rearrangements of active site loops and is well characterized[11]. In cells, IMPDH assembles into large filamentous ultrastructures, and recent *in vitro* work has defined the mechanism of IMPDH self-assembly into filaments, and shown that assembly plays a role in allosteric regulation[12–16].

1.3 Human IMPDH

In humans, there are two isoforms of IMPDH that share 84% sequence identity: IMPDH2 is found in many tissues and is up-regulated in proliferating cells while IMPDH1 plays a housekeeping role and is expressed at similar levels in most tissues[17–19]. In a few tissues including the retina, spleen, and resting peripheral blood mononuclear cells, there is minimal IMPDH2 expression and IMPDH1 is the predominant isoform[19–21].

IMPDH quaternary structure is linked to activity and regulation by adenine and guanine nucleotides. The monomer is composed of a catalytic domain and a regulatory cystathionine β-synthase domain, and constitutively assembles into tetramers through interactions of the catalytic domains[22] (Fig. 1.1b,c). IMP is converted to XMP in an NAD^+ dependent reaction in the catalytic domain[11]. The regulatory domain has three allosteric nucleotide binding sites for adenine and guanine nucleotides[12,14,23] (Fig. 1.1c). Site 1 has a preference for ATP/ADP, site 2 binds ATP/ADP and GTP/GDP competitively and site 3 exclusively binds GTP/GDP. Binding of nucleotides in sites 1 and 2 drives dimerization of the regulatory domains and formation of octamers, and the balance between ATP and GTP binding dictates whether octamers adopt an extended/active conformation or a compressed/inactive conformation (Fig. 1.1c)[13,14]. GTP binding at both competitive site 2 and the GTP-only site 3 induces two conformational changes in IMPDH2: compression of the octamer and flexing of the catalytic domains from an active 'flat' to a partially inactive 'bowed' conformation. These changes inactivate IMPDH2 by preventing essential loop movements in the core of the enzyme[12,15,24]. Nucleotide-dependent assembly of IMPDH2 into filaments stabilizes the flat tetramer conformation, but does not prevent compression, allowing filamentous IMPDH2 to remain partially active even at high GTP concentrations, consistent with the role of IMPDH2 in expanding guanine nucleotide pools during proliferation[13,15] (Fig. 1.1d).

1.4 IMPDH filaments in cells

In vertebrate cells, IMPDH forms filaments in response to the high demand for guanine nucleotides[25–27]. Activation of T-cells also drives the assembly of IMPDH into filaments[28,29]. Given that the human isoforms have a high degree of sequence similarity and most antibodies cannot distinguish between isoforms, it is challenging to determine which isoform(s) are in these ultrastructures in cells in immunofluorescence experiments[25,30–36]. Immunogold labeling of fixed cells suggest that IMPDH ultrastructures are made up of shorter filaments that laterally interact to form bundles[37,38]. *In vitro*, both IMPDH isoforms assemble into single stranded filaments[13,14,39]; why these single stranded structures tend to aggregate into bundles in cells remains unclear, and may be the result of macromolecular crowding, or be driven by interactions with other cellular factors. Thorough characterization of IMPDH filaments *in vitro* has revealed that nucleotide binding to the regulatory domain promotes self-assembly of filaments made of stacked octamers (Fig 1.1d)[13,14,39]. IMPDH2 filaments serve a regulatory function, allowing the protein to resist GTP-feedback inhibition[15] while canonical IMPDH1 filaments have no effect on activity or inhibition[16].

1.5 IMPDH co-localization with other enzymes

IMPDH is reported to directly interact with many other enzymes. Using pulldowns, studies have found that IMPDH2 interacts with many proteins but the functional consequences of these interactions remains to be investigated[40,41,42,43,44]. One recently discovered interaction is the SARS-CoV-2 protein nonstructural protein 14 (Nsp14)[40,41] which we speculate might be a mechanism in regulating IMPDH2's role in the immune response[28,29]. IMPDH interacts with two-cancer related proteins: the ankyrin domain containing protein 9 (ANKRD9) [42,43] and co-localizes with Ras-related C3 botulinum toxin substrate 1 (RAC1) in protrusions of invading cells[45.] Nucleotide biosynthesis is upregulated in many proliferating cancers so one hypothesis is that these interactions are a mechanism to up-regulated purine biosynthesis. Finally IMPDH filaments in cells co-localize with CTPS filaments[30,33,46], the rate-limiting enzyme in pyrimidine biosynthesis that also forms allosterically regulated filaments in cells. This interaction is particularly intriguing because it suggests there is cross talk between the enzymes responsible for the different branches of nucleotide biosynthesis. Together these protein interactions suggest that interaction with IMPDH is a mechanism of regulating nucleotide biosynthesis but more work will need to be done to identify how these interactions regulate IMPDH activity or nucleotide levels.

1.6 Blindness-associated IMPDH1 mutations

Mutations in IMPDH1 lead to autosomal dominant retinal degeneration in humans, a condition known as retinitis pigmentosa or Leber congenital amaurosis, but the molecular mechanism of disease remains unknown[47–51] (Fig 1.2) The activity of the mutant enzymes is normal, but some mutations reduce sensitivity to GDP inhibition[14], change filament assembly parameters[31,39], affect phosphorylation[52], and disrupt association with nucleic acids[51,53,54], yet not all mutations have the same effect. These observations have led to proposed mechanisms of disease including defective ability to bind single stranded DNA[55], protein aggregation[49], or disruption of phosphoregulation[52] but there is not yet a cohesive theory for the molecular mechanism of disease (Table 1.1).

Despite expression of IMPDH1 in almost all tissues[19,21] and the ubiquitous need to maintain balanced purine pools, the retina is the only affected tissue. This may be due to the specific purine demands in the retina[56]. Photoreceptors have an unusually high demand for ATP, particularly in the dark[57], and cyclic guanosine monophosphate (cGMP) is the key signaling molecule in the phototransduction cascade[58–60]. Furthermore, the retina is uniquely dependent on IMPDH1, because expression of both IMPDH2 and the major purine salvage enzyme HPRT are very low in the tissue[21,49]. The complex dependence of photoreceptor function on balanced purine production may lead to severe consequences[61,62].

1.7 IMPDH1 in the retina

IMPDH1 is the major isoform in the retina. In mammals, retinal IMPDH1 is expressed as two major splice variants[21,63,64]. Both mammalian IMPDH1 retinal splice variants maintain the core canonical protein, but additional exons add residues to the C-terminus or both the C- and N-termini (Fig. 1.3). The retinal variants are named for the number of amino acids. In humans, the shorter retinal variant is IMPDH1(546) which has five residues at the canonical C-terminus replaced by 37 new mostly unstructured residues[21] IMPDH1(546) is the more common retinal variant in humans[21]. The other human retinal variant IMPDH1(595) has the same C-terminal extension, plus an additional 49 residues at the N-terminus most of which is predicted to be unstructured, except a short, predicted helix near the canonical N-terminus [21,63,64] (Fig 1.4). Mouse and human retinal variants have reduced sensitivity to GTP inhibition compared with the canonical variant[16,65,66]. The N- and C-terminal retinal splice variant extensions independently contribute to the reduced sensitivity to feedback inhibition by GTP[16] which is consistent with the high guanine nucleotide demand in photoreceptors[56].

Three phosphorylation sites were recently described in retinal IMPDH1[52] (Fig. 1.5a). One phosphorylation site, T159/S160, is preferentially phosphorylated upon light exposure (Fig. 1.5b) but it is not clear which residue is phosphorylated. Therefore, the potential effect at each site must be considered. The phosphorylation site T159/S160 is in the regulatory domain where T159 points directly into nucleotide site 1 while S160 is near both site 1 and site 2, suggesting that phosphorylation at T159/S160 prevents nucleotide binding in site 1 and possibly site 2. Indeed, the phosphomimetic mutations T159D/E and S160D/E in canonical IMPDH1 resist GTP inhibition[52], suggesting phosphorylation at these sites disrupts GTP binding which may affect octamer conformation or filament assembly[23,39]. *In vivo*, increased phosphorylation at site T159/S160 is associated with increased supramolecular assembly[52]. Future studies to determine if phosphorylation at T159/S160 disrupts nucleotide binding and if it influences protein conformation would be informative. The second phosphorylation site S416 is on a loop near the active site whose movement is necessary for catalytic activity[11] (Fig 1.5c), and the phosphomimetic mutation S416D severely decreases V_{max}[52]. The third phosphorylation site S477 is preferentially phosphorylated in the dark. S477 is located at the filament assembly large interface (IMPDH1(546) extended filament and both IMPDH1(595) extended and compressed filaments)[16] and we predict phosphorylation here would disrupt filament assembly (Fig. 1.5d). This site is particularly compelling because it is not involved in the interface of the GTP-bound IMPDH1(546) filament[16]. The consequences of these phosphorylations on filament assembly have yet to be characterized *in vitro*. Flux through the *de novo* purine biosynthesis pathway increases with light, and the observed light-dependent phosphorylation patterns[52] suggest a mechanism for regulating IMPDH1 activity. In this context, phosphorylation of T159/S160 after a period of bright light exposure likely promotes retinal IMPDH1 to resist GTP inhibition and increase flux to guanine nucleotides while this flux is reduced in the dark by phosphorylation at S477 which we suspect contributes to the disassembly of IMPDH1 ultrastructures into more readily inhibited tetramers.

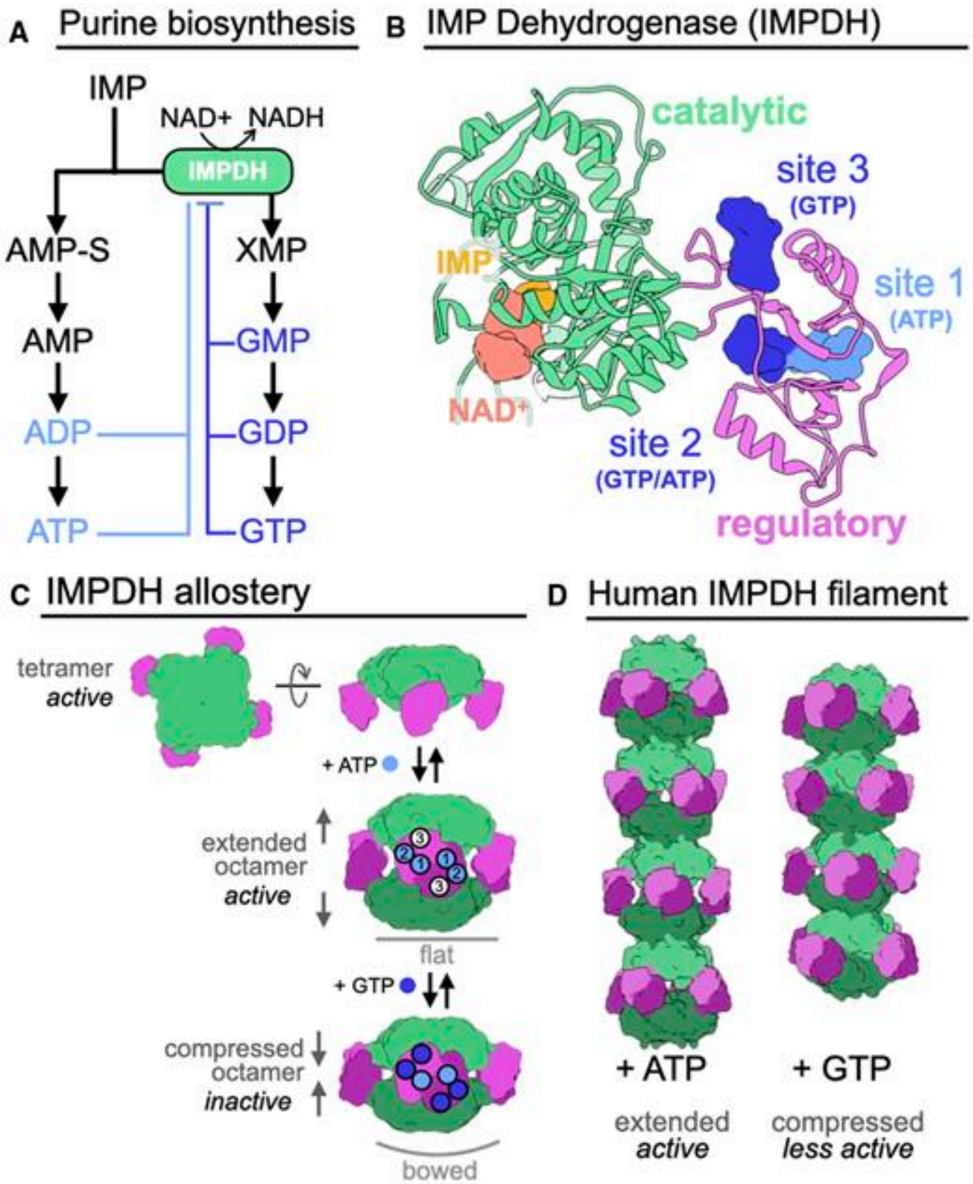

Figure 1.1: IMPDH structure and function.

a, Purine biosynthesis pathway. **b**, IMPDH monomer (6u9o) has a catalytic domain (green) that binds IMP and NAD$^+$ in the active site, and a regulatory domain (pink) with three allosteric nucleotide binding sites. **c**, IMPDH is a tetramer in solution and can adopt a flat or bowed conformation. Side view of tetramers are depicted, so that only two monomers are visible. **d**, ATP (sites 1&2) or GTP (sites 2&3) binding promotes octamer assembly. **e**, IMPDH2 octamers can assemble into filaments of stacked octamers.

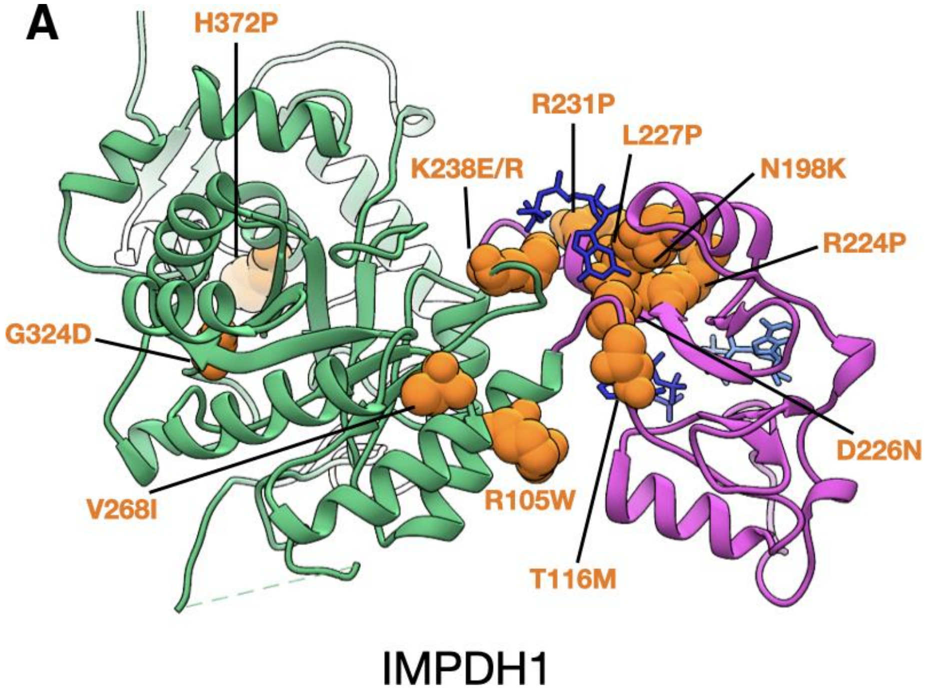

Figure 1.2: IMPDH1 disease mutations
IMPDH (7rfg) monomer with the catalytic domain in green and regulatory domain in pink. Regulatory domain is bound to two GTP molecules in dark blue and one ATP in light blue.

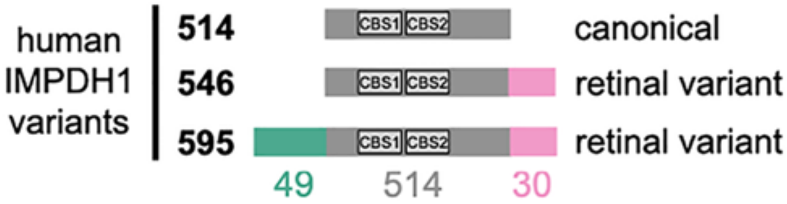

Figure 1.3: IMPDH1 human retinal variants
Representation of IMPDH1 variant sequences.

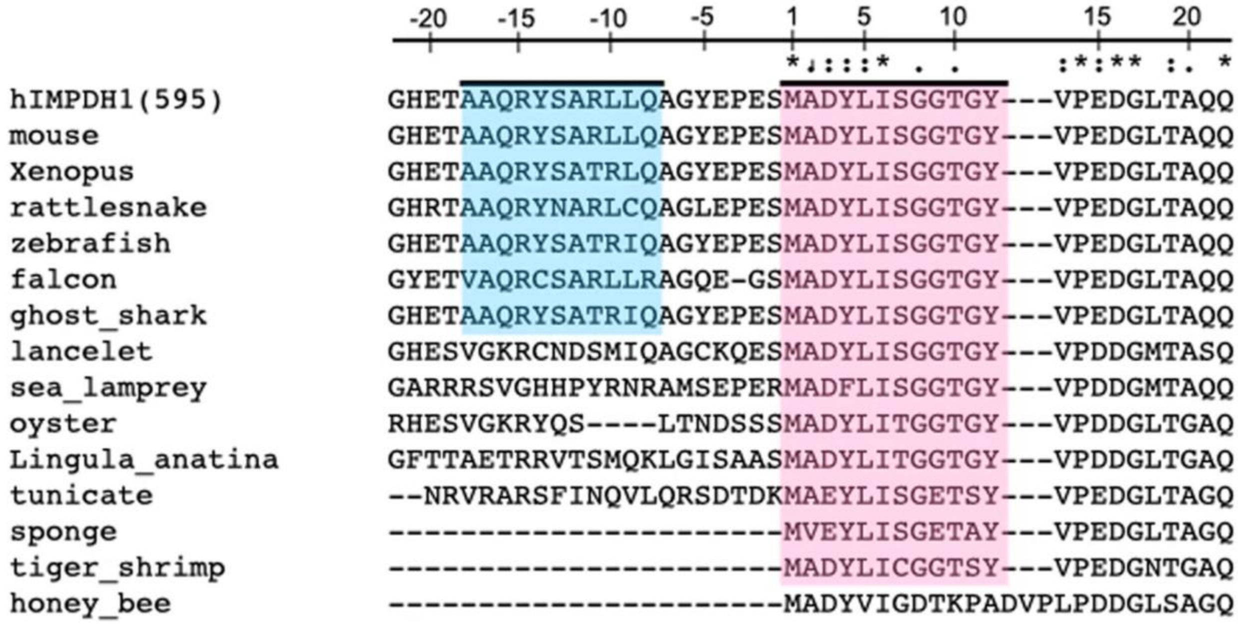

```
                                          *::::* . .     :*:** :. *
hIMPDH1(595)        GHETAAQRYSARLLQAGYEPESMADYLISGGTGY---VPEDGLTAQQ
mouse               GHETAAQRYSARLLQAGYEPESMADYLISGGTGY---VPEDGLTAQQ
Xenopus             GHETAAQRYSATRLQAGYEPESMADYLISGGTGY---VPEDGLTAQQ
rattlesnake         GHRTAAQRYNARLCQAGLEPESMADYLISGGTGY---VPEDGLTAQQ
zebrafish           GHETAAQRYSATRIQAGYEPESMADYLISGGTGY---VPEDGLTAQQ
falcon              GYETVAQRCSARLLRAGQE-GSMADYLISGGTGY---VPEDGLTAQQ
ghost_shark         GHETAAQRYSATRIQAGYEPESMADYLISGGTGY---VPEDGLTAQQ
lancelet            GHESVGKRCNDSMIQAGCKQESMADYLISGGTGY---VPDDGMTASQ
sea_lamprey         GARRRSVGHHPYRNRAMSEPERMADFLISGGTGY---VPDDGMTAQQ
oyster              RHESVGKRYQS----LTNDSSSMADYLITGGTGY---VPDDGLTGAQ
Lingula_anatina     GFTTAETRRVTSMQKLGISAASMADYLITGGTGY---VPDDGLTGAQ
tunicate            --NRVRARSFINQVLQRSDTDKMAEYLISGETSY---VPEDGLTAGQ
sponge              ----------------------MVEYLISGETAY---VPEDGLTAGQ
tiger_shrimp        ----------------------MADYLICGGTSY---VPEDGNTGAQ
honey_bee           ----------------------MADYVIGDTKPADVPLPDDGLSAGQ
```

Figure 1.4: IMPDH1 Sequence Alignment
Evolutionary conservation of the helix in the N-terminus of the longer retinal splice variant (blue) and the first 12 canonical residues particularly tyrosine 12 (pink).

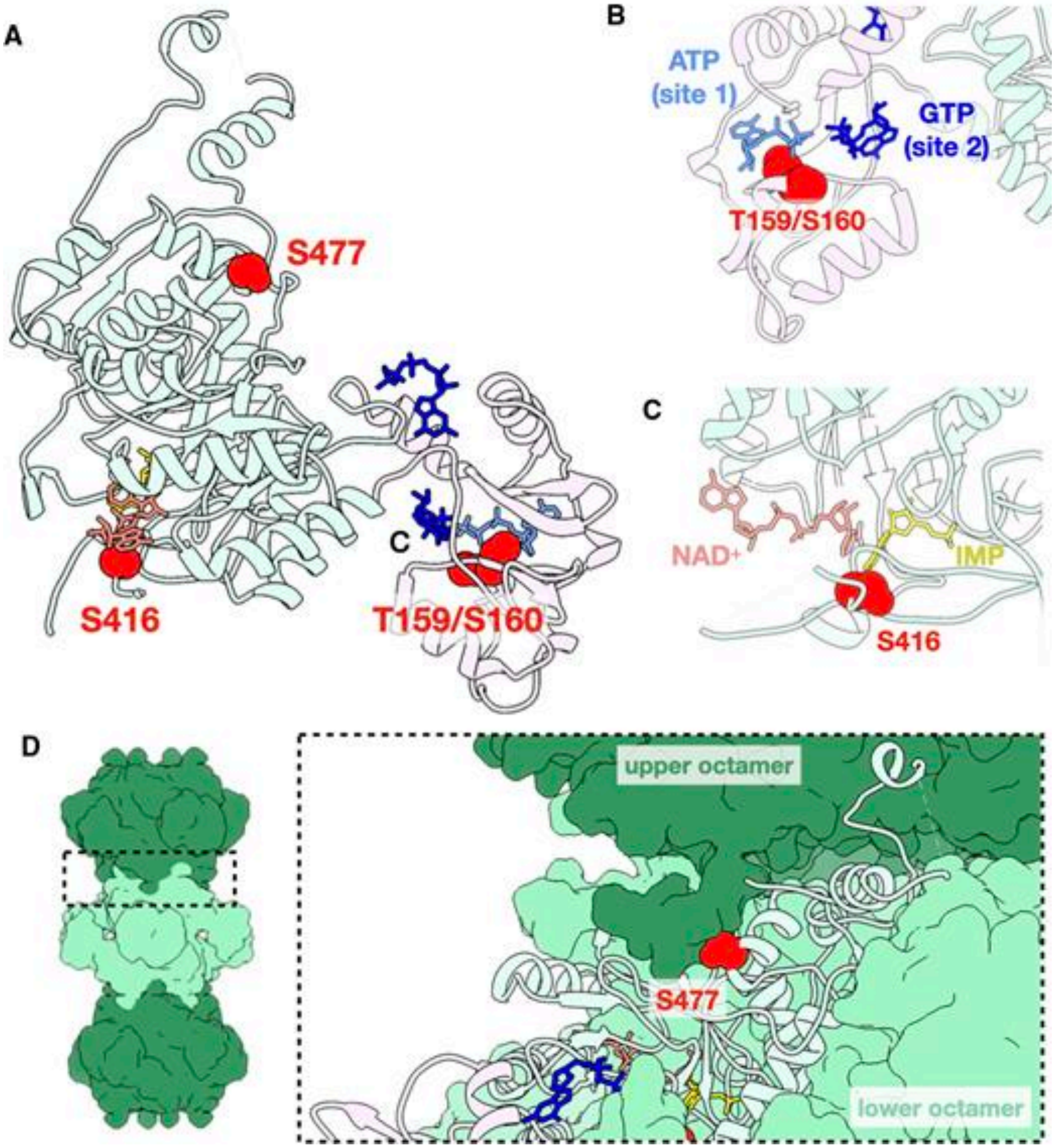

Figure 1.5: IMPDH1 retinal phosphorylation sites[52]

A, IMPDH1 monomer (7rgd) with retinal phosphorylation sites[52] shown in red spheres. **B**, Zoomed in view of phosphorylation site S416 showing its proximity to the active site with NAD$^+$ in salmon and IMP in gold. **C**, Phosphorylation site T159/S160 is between nucleotide binding sites 1 and 2 in the regulatory domain and might disrupt binding at either/both site(s). **D,** Surface representation of IMPDH filament and zoom in of the interface between octamers where phosphorylation site S477 is nestled.

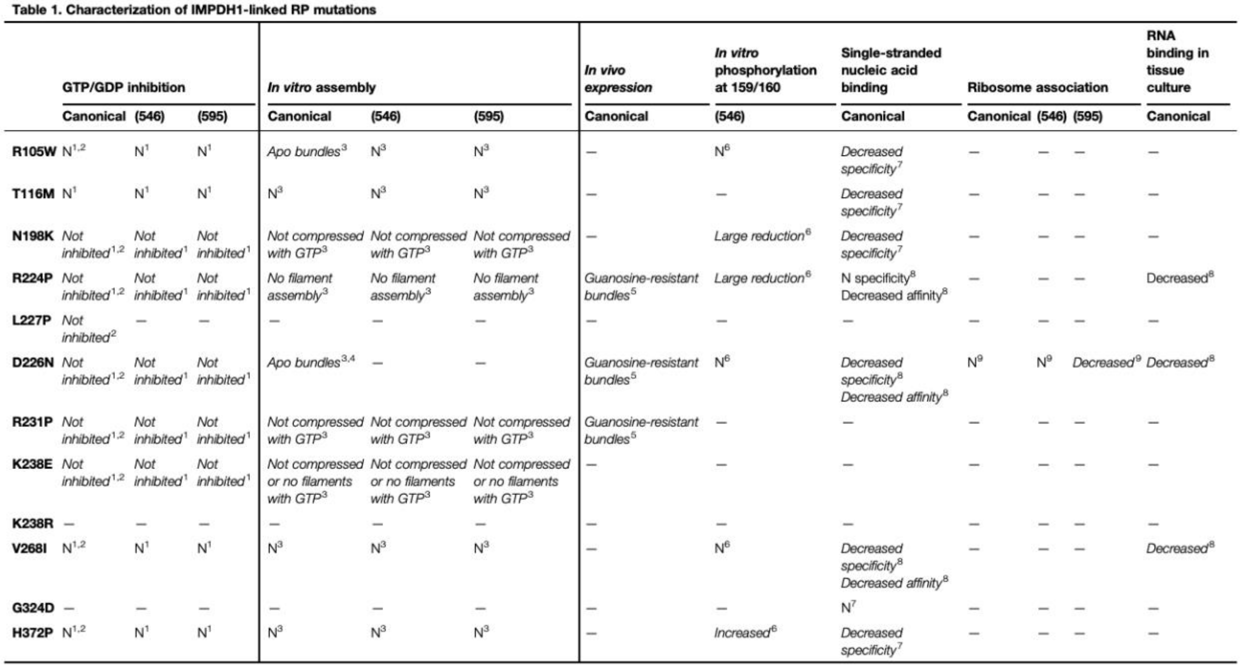

Table 1. Characterization of IMPDH1-linked RP mutations

	GTP/GDP inhibition			*In vitro* assembly			*In vivo* expression	*In vitro* phosphorylation at 159/160	Single-stranded nucleic acid binding	Ribosome association			RNA binding in tissue culture
	Canonical	**(546)**	**(595)**	**Canonical**	**(546)**	**(595)**	**Canonical**	**(546)**	**Canonical**	**Canonical**	**(546)**	**(595)**	**Canonical**
R105W	N[1,2]	N[1]	N[1]	*Apo bundles*[3]	N[3]	N[3]	–	N[6]	*Decreased specificity*[7]	–	–	–	–
T116M	N[1]	N[1]	N[1]	N[3]	N[3]	N[3]	–	–	*Decreased specificity*[7]	–	–	–	–
N198K	*Not inhibited*[1,2]	*Not inhibited*[1]	*Not inhibited*[1]	*Not compressed with GTP*[3]	*Not compressed with GTP*[3]	*Not compressed with GTP*[3]	–	*Large reduction*[6]	*Decreased specificity*[7]	–	–	–	–
R224P	*Not inhibited*[1,2]	*Not inhibited*[1]	*Not inhibited*[1]	*No filament assembly*[3]	*No filament assembly*[3]	*No filament assembly*[3]	*Guanosine-resistant bundles*[5]	*Large reduction*[6]	N specificity[8] Decreased affinity[8]	–	–	–	Decreased[8]
L227P	*Not inhibited*[2]	–	–	–	–	–	–	–	–	–	–	–	–
D226N	*Not inhibited*[1,2]	*Not inhibited*[1]	*Not inhibited*[1]	*Apo bundles*[3,4]	–	–	*Guanosine-resistant bundles*[5]	N[6]	*Decreased specificity*[8] *Decreased affinity*[8]	N[9]	N[9]	*Decreased*[9]	*Decreased*[8]
R231P	*Not inhibited*[1,2]	*Not inhibited*[1]	*Not inhibited*[1]	*Not compressed with GTP*[3]	*Not compressed with GTP*[3]	*Not compressed with GTP*[3]	*Guanosine-resistant bundles*[5]	–	–	–	–	–	–
K238E	*Not inhibited*[1,2]	*Not inhibited*[1]	*Not inhibited*[1]	*Not compressed or no filaments with GTP*[3]	*Not compressed or no filaments with GTP*[3]	*Not compressed or no filaments with GTP*[3]	–	–	–	–	–	–	–
K238R	–	–	–	–	–	–	–	–	–	–	–	–	–
V268I	N[1,2]	N[1]	N[1]	N[3]	N[3]	N[3]	–	N[6]	*Decreased specificity*[8] *Decreased affinity*[8]	–	–	–	*Decreased*[8]
G324D	–	–	–	–	–	–	–	–	N[7]	–	–	–	–
H372P	N[1,2]	N[1]	N[1]	N[3]	N[3]	N[3]	–	*Increased*[6]	*Decreased specificity*[7]	–	–	–	–

Table 1.1: Characterization of IMPDH1-linked RP mutations
Summary of the conditions IMPDH1 disease mutations have been tested. Dashed line indicates there are no published results, bold text indicates a finding that is indistinguishable from wildtype, N stands for ‘normal’, while italic text indicates a behavior different from wildtype.

1 [16]
2 [14]
3 - unpublished - Burrell & Kollman
4 [39]
5 [67]
6 [52]
7 [51]
8 [55]
9 [53]

Chapter 2: Human IMPDH splice variants tune filament assembly

2.1 IMPDH1 filaments assemble filaments *in vitro*

We tested the effects of the allosteric regulators ATP and GTP on IMPDH1 filament assembly and found broad similarities between IMPDH1 and IMPDH2. Using negative stain electron microscopy (EM), we found that, like IMPDH2, IMPDH1 assembles into filaments of stacked octamers in the presence of ATP or GTP (Fig. 2.1a). The ATP-bound IMPDH1 filaments have a 110 Å rise and the GTP-bound IMPDH1 filaments have a 95 Å rise, consistent with extended/active and compressed/inactive octamers seen in IMPDH2 filaments[13]. We previously engineered a separation of function point mutation in IMPDH2 at the filament assembly interface, Tyr12Ala, which disrupts polymerization but does not affect enzyme activity[13,15]. The Y12A mutation also inhibits polymerization of IMPDH1, suggesting both isoforms assemble with similar interfaces (Fig. 2.1a).

Previous studies have shown that IMPDH1 forms ultrastructures in cells, but the question remains whether the cellular ultrastructures assemble by the same mechanism as filaments in vitro[67]. To test this, we transiently transfected human embryonic kidney 293 (HEK293) cells with IMPDH1-myc, and induced filament assembly by treatment with the IMPDH inhibitor mycophenolic acid (MPA), a standard assay for cellular filament assembly[25,30,31]. In cells, IMPDH filaments appear to bundle together to assemble large ultrastructures several micrometers in length[37]. Staining with an anti-myc antibody shows strong induction of ultrastructure assembly with WT IMPDH1, but not with IMPDH1-Y12A, suggesting that the ultrastructures observed in cells are composed of filaments with an architecture similar to those we observe in vitro (Fig. 2.1b).

2.2 IMPDH1 filaments remain sensitive to feedback inhibition

We characterized the substrate kinetics of IMPDH1 and IMPDH2 and found them to be nearly identical (Supp. Table 2.1). However, we found a large difference in sensitivity to GTP inhibition, with the GTP half-maximum inhibitory concentration (IC_{50}) fourfold lower for IMPDH1 than for IMPDH2 (Fig. 2.1c,d)[14]. Consistent with our previous results[15], the non-assembly mutant IMPDH2-Y12A has a lower IC_{50} than the WT enzyme, but the same mutation has no effect on GTP affinity in IMPDH1 (Fig. 2.1c,d).

It is notable that IMPDH1-WT and Y12A mutants in both isoforms have similar GTP sensitivity and are mostly inhibited at high GTP concentrations, while IMPDH2-WT retains basal activity even at GTP concentrations six times higher than the IC_{50} (Supp. Fig. 2.1). This suggests conservation of the intrinsic allosteric regulation, with the difference being that polymerization reduces the inhibitory effect of GTP in IMPDH2 but appears to have no role in tuning the response of IMPDH1. This was surprising given the similarity of GTP-bound IMPDH1 and IMPDH2 filaments in our low-resolution negative stain imaging (Fig. 2.1a), so we next turned to higher resolution cryogenic-EM (cryo-EM) of IMPDH1 filaments to provide insight into differences in inhibition behavior.

2.3 Cryo-EM reveals IMPDH1 forms polymorphic filaments

We determined the structure of the IMPDH1 extended filament bound to ATP, IMP and NAD$^+$ by cryo-EM, using the approach we developed to solve structures of IMPDH2 filaments, which have a rigid assembly interface between octamers but are more flexible within the octamer[15]. This single-particle approach allows for high resolution structures of different regions of the filament by combining density subtraction, focused classification and focused refinement of two different regions of IMPDH1 filaments: full octamers and the interface between stacked octamers (Supp. Fig. 2.2) that together represent the necessary information for the entire IMPDH1 filament. Because all substrates and cofactors are present in this reconstruction, the enzyme was actively turning over when prepared for cryo-EM analysis, so the active site likely contains a mixture of bound substrates and products; nonetheless, the active site was well-resolved in the final cryo-EM map (Supp. Fig. 2.3). This approach yielded octamer- and interface-focused reconstructions at 3.1 and 2.6 Å resolution, respectively (Fig. 2.2a-c and Table 2.1) for extended IMPDH1 filaments.

The extended filament structure is highly conserved between IMPDH1 and IMPDH2. Like IMPDH2, the IMPDH1 extended filament is composed of D4 symmetric stacked octamers with filament assembly contacts made between catalytic domains of opposing octamers. Each octamer has a rise of 113 Å and right-handed helical rotation of 30° between octamers. The interface buries a total of 10,600 Å^2 (1,320 Å^2 per monomer) (Fig. 2.2d) and is formed by residues 2–12 from the N terminus of one monomer that sit in a groove between two helices in the catalytic domain of the opposing monomer (Fig. 2.2e,f). Tyr12, which breaks filament assembly when mutated to alanine, packs against Arg356 on the opposing monomer (Fig. 2.2f). This filament architecture results in a tetramer in the flat conformation (Fig. 2.2g) similar to IMPDH2 (0.964 Å root mean-squared deviation (r.m.s.d.) for alpha carbons over the catalytic domains of the tetramer) (Supp. Table 2.2). Overall, the filament interface and protomer conformations of IMPDH1 filaments are nearly identical to the IMPDH2 filament[15].

The only major difference between isoforms in the extended filament appears to be the degree of flexibility in the octamer subunit. Active IMPDH2 shows extreme heterogeneity with mixed partially extended and partially compressed conformations in the same filament, due to flexibility between the catalytic and regulatory domains[15]. The interface-centered reconstruction reached a higher resolution than the octamer-focused reconstruction, likely due to some limited flexibility between domains. However, after extensive classification in the octamer-centered reconstruction we found that almost all protomers in the IMPDH1 filament structure are in the fully extended conformation and relatively homogenous despite the enzyme actively making product. This may reflect a higher degree of cooperativity in the conformational state of IMPDH1 relative to IMPDH2.

We next solved a cryo-EM structure of the IMPDH1 compressed filament bound to GTP, ATP and IMP, and found it assembles with a completely different architecture, with different interface contacts that lead to different helical symmetry (Fig. 2.3a-d and Table 2.1). The filament is still made up of D4 symmetric octamers but the N-terminal residues of one monomer now contact a different groove in the catalytic domain of the monomer in the opposing octamer (Fig. 2.3e). This change in interaction leads to a large shift in helical geometry where the rotation between stacked octamers increases from 30° to 74°. The major contacts are between Tyr12 and Glu15 on the N terminus and Glu487 and Lys489 on the opposing monomer (Fig. 2.3e,f). The involvement of Tyr12 in this interface explains why the Tyr12Ala point mutation also prevents assembly of this filament (Fig. 2.1a). The surface area buried by the interface is 75% smaller: 2,800 Å^2 buried at the octamer–octamer interface (350 Å^2 per monomer) for the compressed IMPDH1 filament compared to 10,600 Å2 for the extended IMPDH1 filament interface (Figs. 2.2d and 2.3d). We refer to this new interface as the 'small interface' and the previously characterized interface in all IMPDH2 filaments and extended IMPDH1 as the 'large interface'.

The GTP-bound IMPDH1 filament accommodates a bowed tetramer that is mostly inhibited (Fig. 2.3g). In contrast, GTP binding causes compression of IMPDH2, but filament contacts constrain the catalytic tetramers in a flat conformation, yielding a partially active flat, compressed state (Supp. Fig. 2.1a and 2.4a). A free IMPDH2 octamer is not restrained and able to adopt a bent, compressed state that is completely inhibited (Supp. Fig. 2.1 and 2.4a). GTP-bound IMPDH1 in filaments is nearly identical to the IMPDH2 free octamer bowed tetramer (Supp. Fig. 2.4a,b) that is also mostly inhibited (Supp. Fig. 2.1a). The conformational change can best be visualized by looking at protomers arranged diagonally to each other in the catalytic tetramer (chains A and C). Relative to the IMPDH1 extended octamer flat conformation, there is a rotation of 6.5° between these two protomers in the compressed bowed conformation, resulting in an r.m.s.d. of 3.8 Å (Supp. Table 2.2). This finding that the IMPDH1 compressed filament accommodates a bowed tetramer provides an explanation for why IMPDH1 filaments do not appear to directly affect regulation by GTP. For IMPDH1, GTP binding causes compression, but shifting filament assembly contacts also accommodates the bowed tetramer conformation, yielding a bowed, compressed state that is mostly inhibited.

2.4 Human retinal splice variants assemble filaments

We tested the effects of the allosteric regulators ATP and GTP on filament assembly of both IMPDH1 retinal variants (Fig. 2.4a,b) and found the response to be similar to canonical IMPDH1. In addition, we engineered a variant IMPDH1(563) that only has the N-terminal extension, to specifically test its effect on filament assembly. Both retinal variants assemble filaments of stacked octamers in the presence of ATP or GTP, and IMPDH1(563) has a propensity to spontaneously assemble in the absence of ligands (Fig. 2.4b). ATP-bound IMPDH1 retinal variant filaments have a roughly 110 Å rise and GTP-bound a roughly 95 Å rise, which is consistent with the IMPDH1 canonical filaments, and it behaves like the retinal variants in negative stain EM. The mutation Tyr12Ala disrupts filament assembly in all the variants (Supp. Fig. 2.5).

2.5 Retinal splice variants are less sensitive to feedback inhibition

The *K*0.5 values for IMP and NAD$^+$ for the IMPDH1 retinal splice variants are very similar to each other and to the canonical variant[68] (Supp. Table 2.3). However, the retinal variants have higher IC$_{50}$s for inhibition by GTP (Fig. 2.4c-e). IMPDH1(563) is three times less sensitive to GTP inhibition, IMPDH1(546) is almost five times less sensitive and IMPDH1(595) six times less sensitive when compared to the canonical variant. These findings are consistent with previous results from the mouse IMPDH1 retinal splice variants[65].

The sensitivity of IMPDH1 retinal variants and IMPDH2 to GTP is similar (Supp. Table 2.3); given the role of filament assembly in tuning GTP sensitivity in IMPDH2, we tested the effect of the Y12A non-assembly mutant on inhibition of IMPDH1 variants. All variants had increased sensitivity to GTP inhibition when the Y12A mutation was introduced (Fig. 2.4c-e). However, for IMPDH1(563), which only has the N-terminal extension, the GTP IC_{50} dropped to canonical levels, indicating that the effect of the N-terminal extension on IC_{50} is dependent on the ability to assemble filaments. Thus, the retina-specific N- and C-terminal additions appear to have distinct mechanisms that function independently to increase the GTP IC_{50}.

2.6 Retinal splice variants alter filament architecture

To gain insight into the mechanisms by which the splice variants alter GTP sensitivity, we determined structures of IMPDH1(595) and IMPDH1(546) in multiple ligand states by cryo-EM (Fig. 2.5a-c and Supp. Fig. 2.6c-f). The IMPDH1(546) extended structure is bound to the same ligand combination as the IMPDH1(514) extended structure (IMP, NAD^+ and ATP) while IMPDH1(595) was solved in the presence of ATP alone to determine whether substrates affect conformational homogeneity in the filament. In the extended state, both variants closely resemble extended canonical filaments, with the enzyme in the fully extended, flat tetramer conformation and the large assembly interface between octamers (Fig. 2.5c, Supp. Fig. 2.6c). In both extended structures, most of the retinal C-terminal extension could not be resolved. Extended canonical IMPDH1 can be resolved to residue 514, while extended IMPDH1(595) could only be modeled to residue 504 and IMPDH1(546) to residue 515. In both IMPDH1(595) structures, there was clear density for a short alpha helix near the filament interface, composed of residues −22 to −4 (Fig. 2.5d). This helix packs between the catalytic core of the enzyme and the canonical N-terminal 15 residues that form the large interface (Fig. 2.5e,f). In this position it also makes contacts with the neighboring protomer in the same tetramer with the major contact between residues Tyr-5 and His288 of the neighbor (Fig. 2.5g,h). The N-terminal end of the variant helix also contacts its symmetry mate on the monomer across the interface with Gln-21 or Gln-15 (Fig. 2.5f). The helix appears to be positioned to stabilize the residues involved in the large interface filament interactions, and to stabilize the flat conformation of the catalytic tetramer.

We next solved structures of IMPDH1(595) in a compressed filament at 3.7 Å resolution by cryo-EM. Unlike the canonical enzyme, IMPDH1(595) is maintained in the large interface and flat tetramer conformation in the compressed, GTP-bound state. The overall interface and position of the helix from the N-terminal extension are very similar to the extended filament described above (1.5 Å r.m.s.d. among $C\alpha$s of all eight catalytic domains at the interface when aligned on a single chain). Thus, the role of the N-terminal extension appears to be stabilizing the large interface, and through that stabilizing the flat enzyme conformation that is less sensitive to GTP inhibition. We would predict that the additional interactions at the interface would increase affinity for assembly and decrease the critical concentration for filament assembly. This explains why the effect of the N-terminal extension is dependent on filament assembly (Fig. 2.4e).

We then wondered how the C-terminal extension contributes to decreased GTP sensitivity. So, we solved a 3.6 Å cryo-EM structure of the compressed IMPDH1(546) filament, which only has the C-terminal extension (Supp. Fig. 2.6a-f). In the compressed octamer conformation, bound to

GTP/ATP/IMP/NAD$^+$, IMPDH1(546) assembles with the small interface and in a bowed conformation, very similar to canonical IMPDH1 (Supp. Fig. 2.6g). For both retinal compressed filament structures, we included all ligands (GTP/ATP/IMP/NAD$^+$) when we had previously left out NAD$^+$ for IMPDH1(514) with the prediction it might lead to a more rigid overall structure but it resulted in very little effect. In all other structures of compressed IMPDH, the conformation of the tetramer in the flat conformation, partially inhibited or bowed conformation or mostly inhibited has explained whether it is more or less sensitive to GTP inhibition. Even though IMPDH1(546) is less sensitive to GTP inhibition than the canonical variant (Fig. 2.4c), its tetramer is still in the bent conformation, which we had associated with mostly complete inhibition (Supp. Fig. 2.6g). Therefore, we suspect the C-terminal extension prevents full octamer compression to resist GTP inhibition. In canonical IMPDH1 bound to GTP, Arg512 and Glu510 near the C-terminus make ionic interactions with residues in protomers on the opposite face of the octamer, stabilizing the compressed conformation. In IMPDH1(546) these residues change to Thr510 and Leu512 (Supp. Fig. 2.7). Disrupting these interactions likely disfavors octamer compression, potentially explaining why IMPDH1(546) resists GTP inhibition. A second possibility is that the remaining 31 residues that are not resolved in any of our IMPDH1(546) are highly flexible, and their presence near the core of the enzyme may sterically hinder compression.

2.7 Discussion

IMPDH ultrastructure assembly has been observed in many cell types and in vitro assembly of IMPDH2 has been thoroughly characterized[15,25,30,31]. Here, we showed that canonical IMPDH1 assembles filaments in both extended and compressed conformations (Figs. 2.1-3 and 6c). Other well-characterized filament-forming metabolic enzymes such as IMPDH2 and CTPS2 also switch enzyme conformations in the polymer, and constraints imposed by fixed assembly contacts give rise to filament-dependent changes in allosteric regulation[15,69] (Fig. 2.6b). IMPDH1, on the other hand, changes both enzyme conformation and the nature of assembly contacts in transitioning between activity states. Thus, filament assembly of canonical IMPDH1 does not impose conformational constraints, explaining why we did not observe any differences in allosteric regulation in the filament compared to free enzyme (Fig. 2.1d).

This raises the question about the physiological function of canonical IMPDH1 filaments. Although we show that IMPDH1 assembles filaments in cells in response to inhibitors (Fig. 2.1b), how cellular filaments might influence metabolic flux is unclear. One possibility is that IMPDH1 filaments play some role other than direct tuning of enzyme activity, such as signaling or scaffolding of other enzymes[46,70]. Another possibility is that cellular factors shift the balance between the extended and compressed filament conformations, for example through posttranslational modifications or protein–protein interactions. There is precedent for the latter in the enzyme acetyl-CoA carboxylase, which assembles active filaments of one architecture, but binding to the regulator breast cancer type 1 susceptibility protein (BRCA1) stabilizes a different architecture with inactive enzyme[71]. Similarly, interactions with regulatory proteins may preferentially stabilize one IMPDH1 filament state. Indeed, in immunofluorescence experiments using antibodies that recognize both isoforms, IMPDH filaments colocalize with other enzymes in purine biosynthesis[70], with the regulatory protein Ankyrin Repeat Domain 9 (ANKRD9)[43] and with CTPS[46]. Future studies to identify interactors and probe the functional consequences of those interactions will provide valuable insight into the role of canonical IMPDH1 filament assembly in a physiological context.

This work also sheds light on the role of IMPDH1 filaments in regulating enzyme activity in the retina. The retina has extremely high purine nucleotide demands: maintenance of ion gradients across photoreceptor membranes consumes up to 10^8 molecules of ATP per second per cell and cGMP is essential for phototransduction[58–60]. IMPDH1 is the only isoform expressed in photoreceptors[21], where it plays a critical role in balancing purine nucleotide pools. Two splice variants that add residues to the N and C termini of IMPDH1 are predominant in the retina[21], and we found that both splice variants are less sensitive to GTP inhibition[65] (Fig. 2.4c,d).

The N- and C-terminal retinal splice variant extensions independently increase the IC_{50} for GTP, consistent with the need for IMPDH1 to meet high guanine nucleotide demand in the retina[56]. Two structural rearrangements occur in IMPDH inhibition: the tetramer is in a bowed conformation and the octamer is fully compressed. We find that each retinal variant extension prevents one of these. The N-terminal extension effect is completely dependent on the ability of the protein to form filaments (Fig. 2.4e), as it tunes filament assembly so the inhibited protein assembles into the large interface filament that can only accommodate the flat/partially active tetramer. This prevents transitioning to the small filament interface, so that at high GTP concentrations the filament remains in a compressed and flat conformation that is partially active (Fig. 2.6d). The C-terminal extension, on the other hand, appears to destabilize the compressed conformation, either through changes at the compressed interface or through steric interference by the disordered region (Supp. Fig 2.7). The overall effect of the splice variants is to increase IMPDH1 activity under high GTP concentrations. Meeting this demand with IMPDH1 splice variants instead of IMPDH2 may provide unique regulatory advantages, through protein–protein interactions with, or posttranslational modifications of the flexible N- and C-terminal extensions.

Future studies of IMPDH1 retinal variants will be necessary to understand the layers of IMPDH1 regulation in the retina. One complication is the simultaneous presence of multiple splice variants[21,63]. The tetramerization and filament assembly contacts are identical among the variants so it is likely they coassemble into heterogeneous tetramers, octamers or filaments. A second complication is the interplay between three known phosphorylation sites[52], assembly state and metabolic output. Phosphorylation site Ser477 is situated at the assembly interface of the large interface filament observed in the compressed retinal variant IMPDH1(595), bolstering previous speculation[52] that phosphorylation at Ser477 may disrupt filament assembly, increasing GTP-feedback inhibition (Fig. 2.4d). Phosphomimetics at two phosphorylation sites, Thr159 and Ser150, decreased sensitivity to GTP inhibition in canonical IMPDH1[52], but functional effects have yet to be characterized in the splice variants. Our structural and in vitro characterization of the IMPDH1 retinal variants has laid the groundwork for these future studies.

Studies of IMPDH1 retinopathy mutants in the physiological context of the retina will be necessary to determine the molecular mechanisms of disease. Mutations are heterozygous and autosomal dominant[47–51], so assembly of WT and mutant enzymes into heterogeneous structures made of different splice variants expressed at different levels is likely to further complicate effects on metabolic output. For example, coassembly of class I mutants and WT enzymes would likely prevent GTP-induced inhibitory conformational changes for all the copies in mixed oligomers.

Many metabolic regulatory enzymes self-assemble into filamentous polymers[4,72]. In most cases filament assembly serves as an additional layer of allosteric regulation, taking advantage of existing allostery but imposing constraints on accessibility of different conformations[4,72]. For example, assembly of human CTPS1 into filaments stabilizes a conformation with higher specific activity to increase flux[73], while CTPS2 assembles filaments that couple structural transitions to increase cooperativity of enzyme regulation[69]. Yeast glucokinase 1 was recently shown to assemble filaments that inactivate the enzyme, providing a mechanism to reduce overinvestment in early steps of glycolysis on sudden transition to nutrient rich environments[74]. Acetyl-CoA carboxylase filaments regulate activity by locking the enzyme into an active or inactive assembly[75]. Here, we have shown that another well-established means of metabolic regulation—tissue-specific splice variants—can add an additional layer of allosteric regulation on top of filament assembly to finely tune complex enzyme regulation (Fig. 2.6).

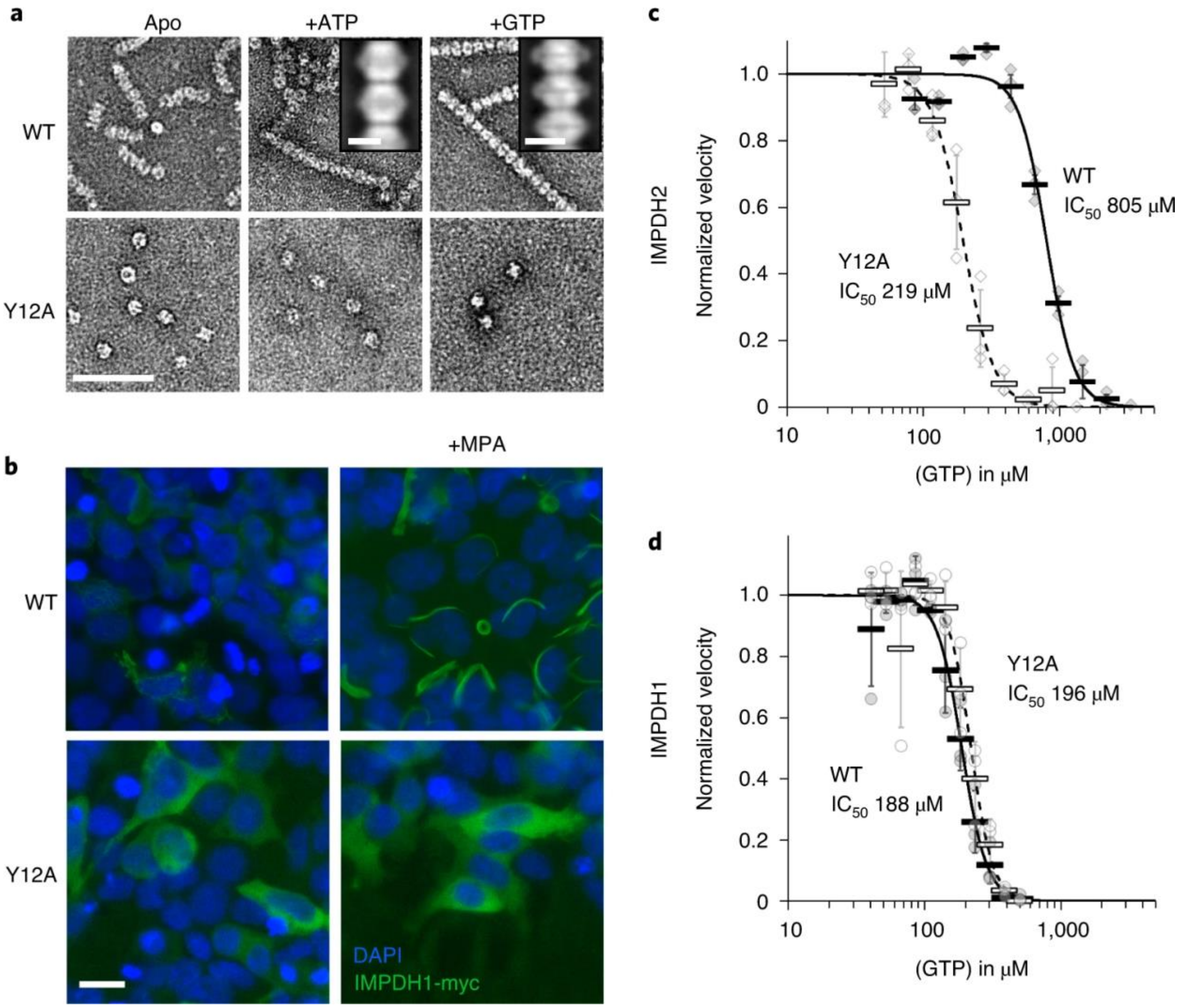

Figure 2.1: IMPDH1 assembles filaments and is sensitive to GTP inhibition.
a, Negative stain EM of purified human IMPDH1. Addition of ATP or GTP promotes filament assembly of WT. Non-assembly mutation Y12A breaks both ATP- and GTP-dependent assembly. Insets are negative stain 2D class averages. Scale bar, 100 nm. **b**, Anti-myc immunofluorescence of HEK293 cells transfected with IMPDH1-myc constructs (green). DAPI staining in blue. Cells were either left untreated or treated with 10 μM MPA to induce IMPDH2 filament assembly. Scale bar, 20 μm. **c,d**, GTP inhibition curves of IMPDH2 (**c**) or IMPDH1-WT (**d**) (solid line) and the respective non-assembly Y12A protein (dashed line). Individual data points are shown as diamonds (IMPDH2) or circles (IMPDH1), where filled are WT and empty Y12A. Reactions were performed in triplicate and data are presented as mean values for each concentration is shown as a bold rectangle (filled is WT, empty is Y12A) ± standard deviation for $n = 3$ error bars. Reactions performed with 1 μM protein, 1 mM ATP, 1 mM IMP, 300 μM NAD$^+$ and varying GTP.

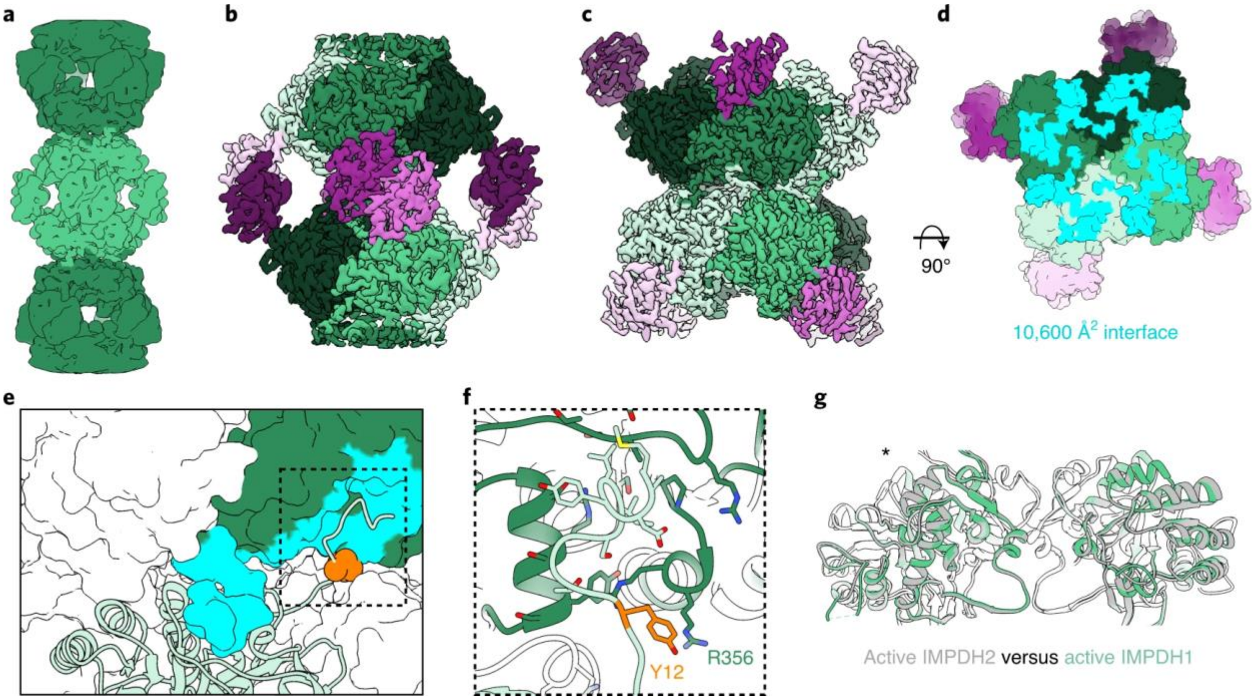

Figure 2.2: Structure of extended IMPDH1 filaments (ATP/IMP/NAD$^+$ bound)
a, Low-pass filtered cryo-EM reconstruction colored by octamer. **b**, Octamer-centered single-particle reconstruction of the filament at 3.1 Å, with catalytic domains in different shades of green and regulatory domains in shades of pink. **c**, Interface-centered single-particle reconstruction of the filament at 2.6 Å. **d**, View of the top of an octamer from inside the filament. Surface representation of the atomic model at the assembly interface, with buried residues in cyan. **e**, Surface representation of the filament interface with one monomer in ribbon (light green). Tyr12 is shown in orange spheres. The monomer it contacts across the octamer interface is green with residues forming the interface in cyan. **f**, Close-up ribbon view of the interface where Tyr12 in orange contacts Arg356 in the opposing monomer. **g**, Comparison of the catalytic tetramers of active IMPDH2 ATP/IMP/NAD$^+$ (PDB 6u8s) (gray) to active IMPDH1 ATP/IMP/NAD$^+$ (green). Aligned on monomers with an asterisk.

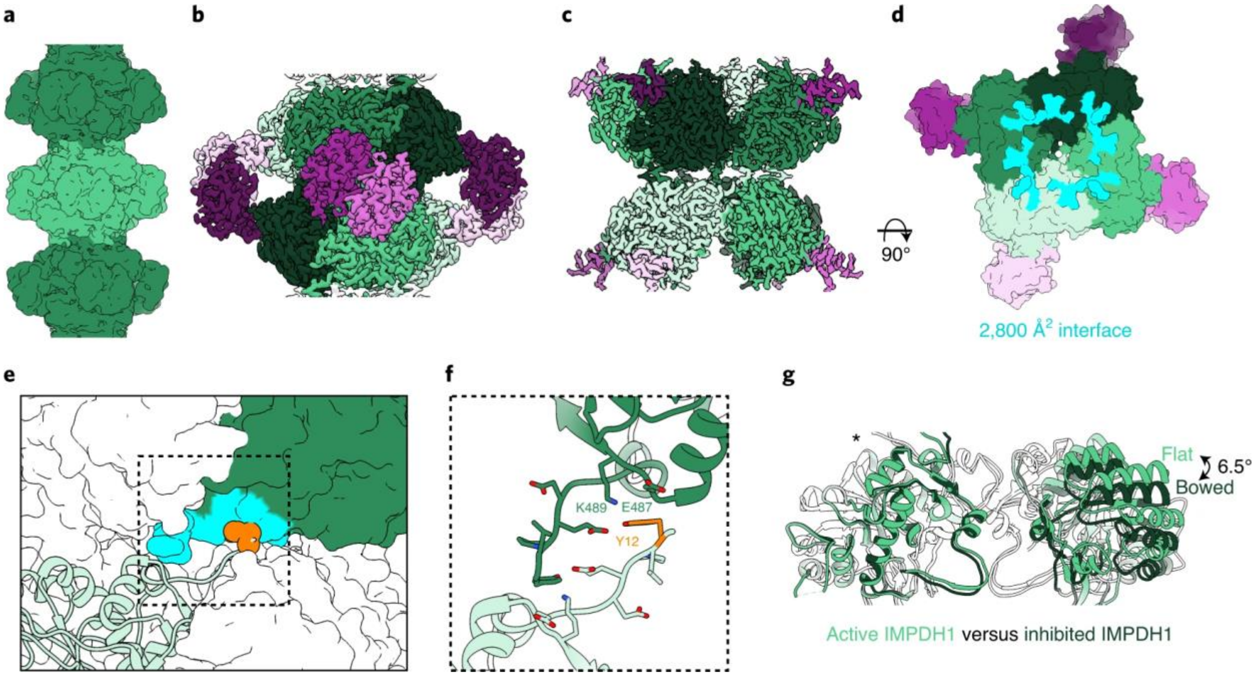

Figure 2.3: Inhibited IMPDH1 assembles with an alternative filament architecture (GTP/ATP/IMP bound).

a, Low-pass filtered cryo-EM reconstruction colored by octamer. **b**, Octamer-centered single-particle reconstruction at 2.6 Å of the filament, with catalytic domains in different shades of green and regulatory domains in shades of pink. **c**, Interface-centered single-particle reconstruction of the filament at 2.6 Å. **d**, View of the top of an octamer from inside the filament. Surface representation of the atomic model at the assembly interface, with buried residues in cyan. **e**, Surface representation of filament interface with one monomer in ribbon (light green). Tyr12 is shown in orange spheres. The monomer it contacts across the octamer interface is green with residues forming the interface in aqua. **f**, Close-up ribbon view of the interface where Tyr12 in orange contacts Glu487 and Lys489 in the opposing monomer. **g**, Comparison of the catalytic tetramers of active IMPDH1 (light green) to mostly inhibited IMPDH1 (dark green), show that the GTP-bound structure is in the bowed conformation. Aligned on monomers with an asterisk.

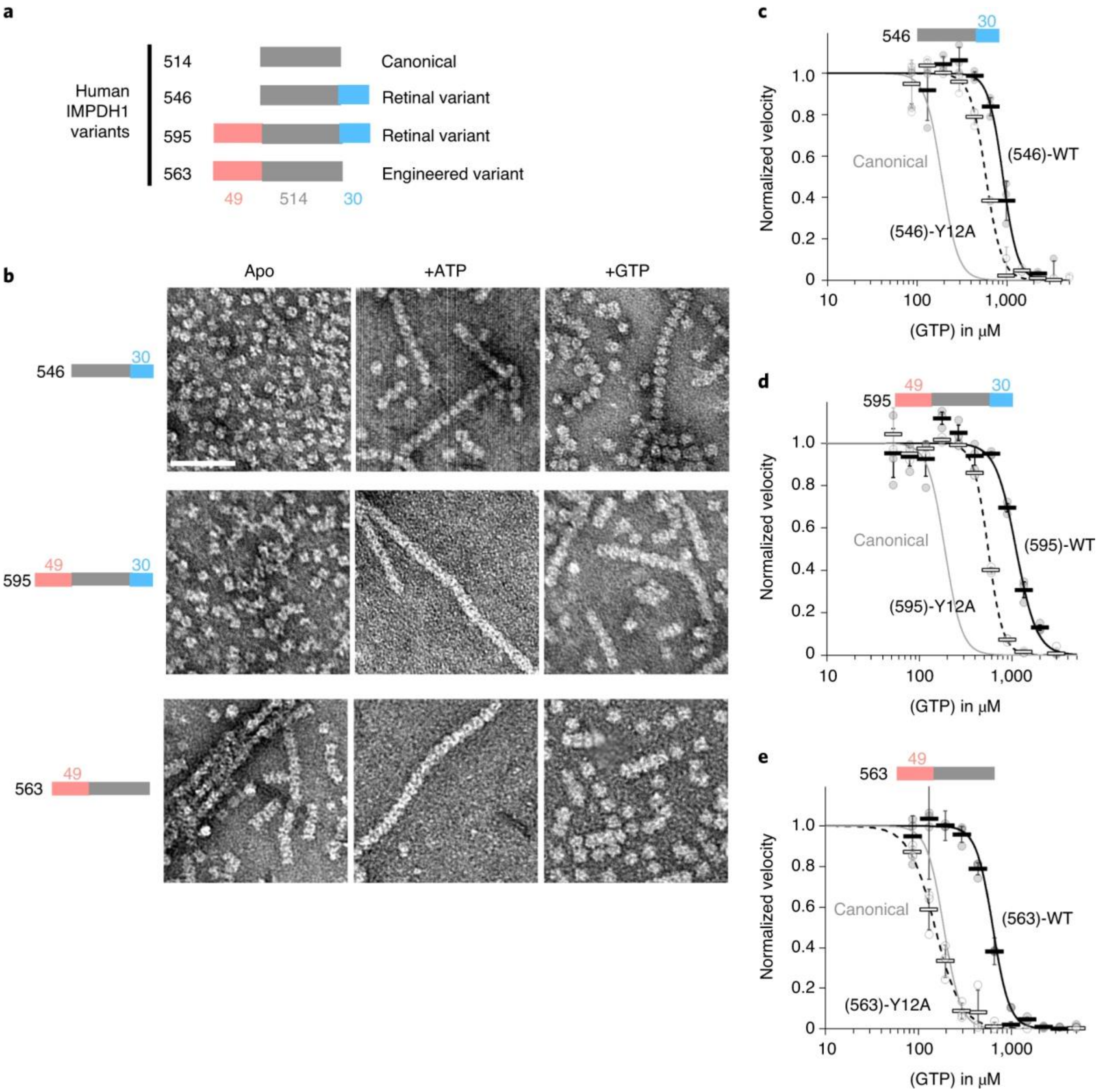

Figure 2.4: IMPDH1 retinal variants assemble filaments that resist GTP inhibition.
a, Representation of IMPDH1 variant sequences. **b**, Negative stain EM of purified IMPDH1 variants in apo and nucleotide-bound states. Scale bar, 100 nm. **c–e**, GTP inhibition curves of IMPDH1 variants (black solid line) and the respective non-assembly Y12A protein (black dashed line) compared to IMPDH1 canonical (solid gray line). **c**, Retinal variant IMPDH1(546). **d**, Retinal variant IMPDH1(595). **e**, Engineered variant IMPDH1(563). Individual data points are shown as circles, where filled are WT and empty Y12A. Reactions were performed in triplicate and the average for each concentration is shown as a bold rectangle (filled WT, empty Y12A). Error bars show the standard deviation for *n* = 3. Reactions performed with 1 μM protein, 1 mM ATP, 1 mM IMP, 300 μM NAD$^+$ and varying GTP.

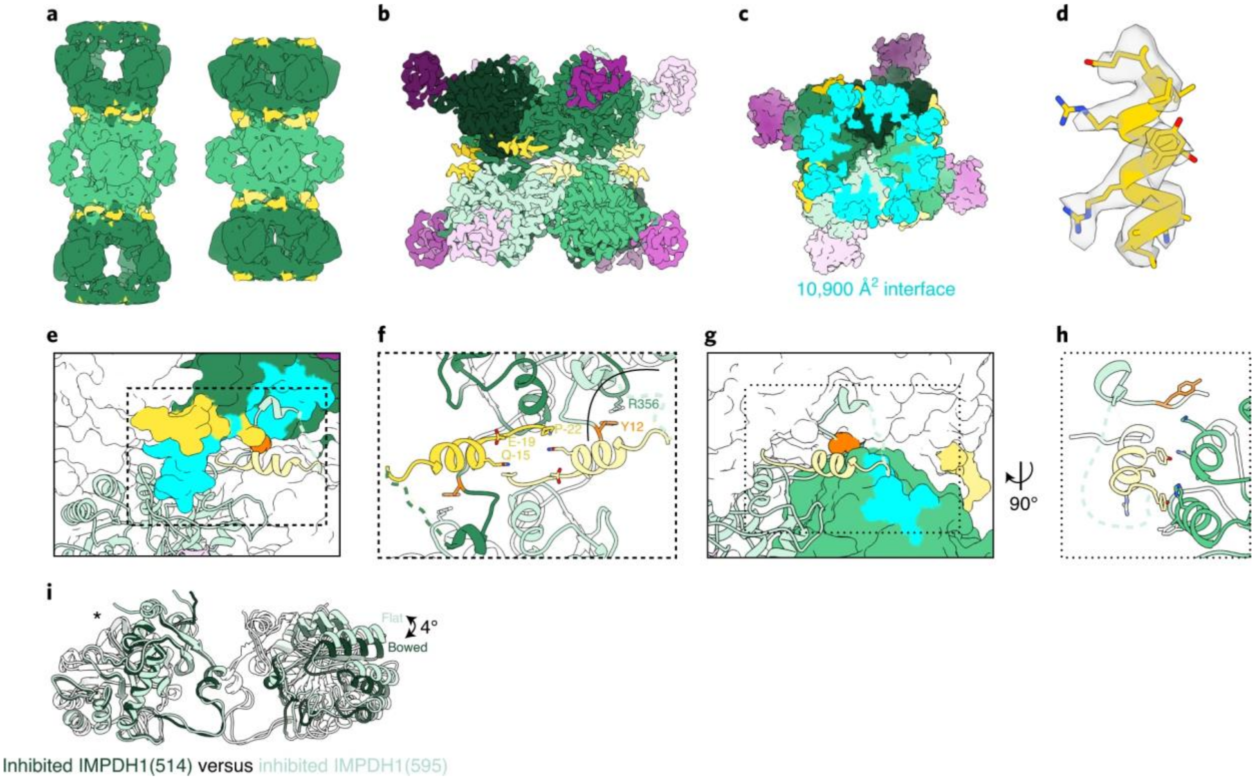

Figure 2.5: IMPDH1 retinal variant (595) constrains filament architecture.

a, Low-pass filtered cryo-EM reconstruction of the IMPDH1(595) extended filament (bound to ATP) and compressed filament (bound to GTP, ATP, IMP, NAD$^+$). **b–k**, Compressed IMPDH1(595) filament (bound to GTP, ATP, IMP, NAD$^+$). b, Interface-focused cryo-EM filament reconstruction. Eight monomers are colored with catalytic domain (green), regulatory domain (pink) and variant helix (yellow). **c**, View of the top of an octamer from inside the filament. Surface representation of the atomic model at the assembly interface, with buried residues in cyan. **d**, Additional N-terminal helix residues −18 to −7 in yellow in density. **e**, Surface representation of interface with one monomer in ribbon (light green). Additional N-terminal helix in yellow. The monomer it contacts across the octamer interface is colored dark green/pink with residues the ribbon monomer contacts in aqua. Tyr12 is shown in orange spheres. **f**, Close-up view of the interface contacts. **g**, Surface representation of interface with one monomer in ribbon (light green). Additional N-terminal helix in yellow. The neighbor monomer in the tetramer is colored green with residues the ribbon monomer contacts in aqua. Y12 is shown in orange spheres. **h**, Close-up view of the new N-terminal helix contacts with the adjacent monomer in the tetramer. **i**, Comparison of the catalytic tetramers of inhibited IMPDH1(514) GTP/IMP/NAD$^+$ (dark green) to inhibited IMPDH1(595) GTP/ATP/IMP/NAD$^+$ (light green). Aligned on monomers with an asterisk.

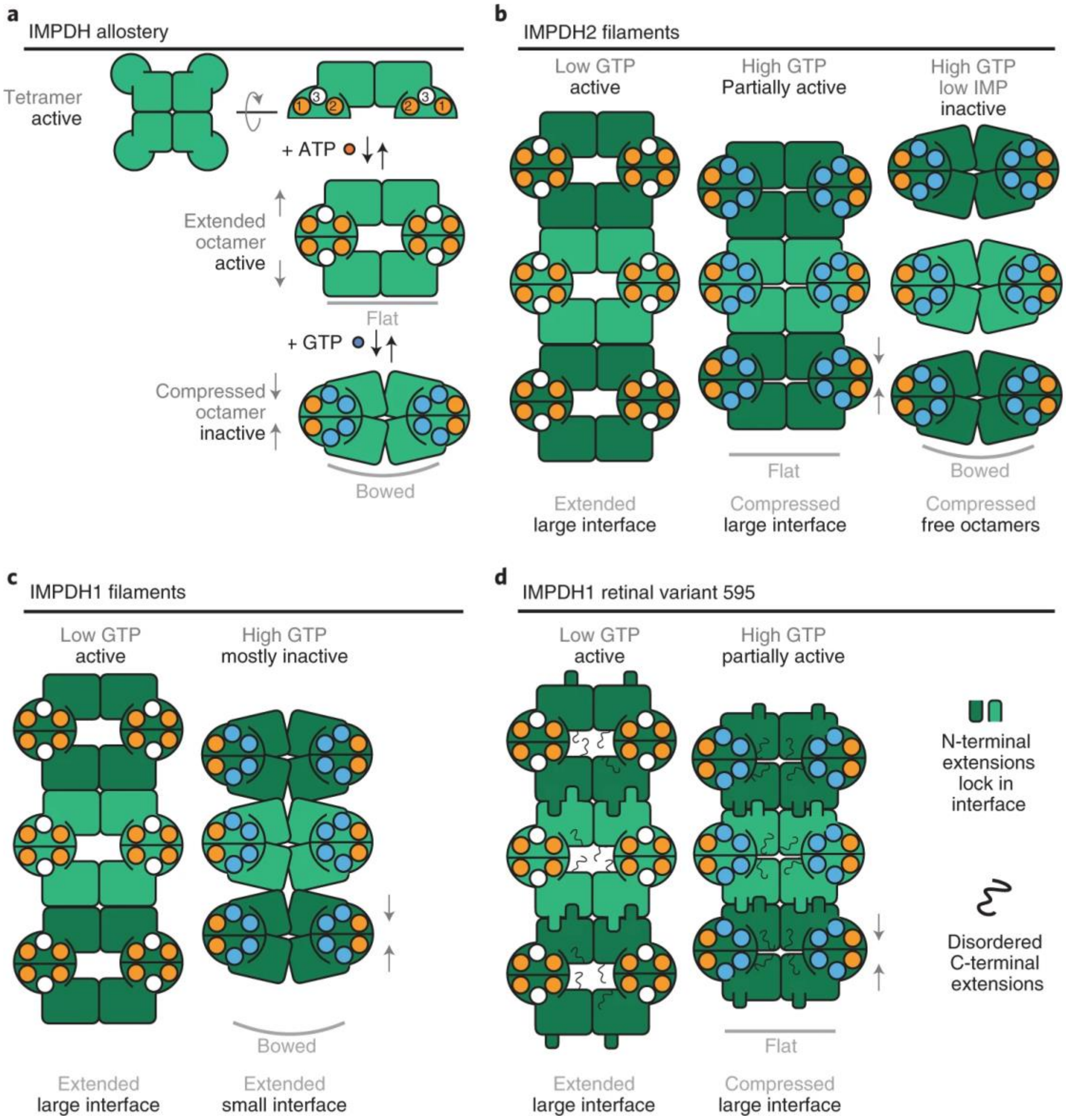

Figure 2.6: Model of IMPDH1 assembly and filament role in regulation.
a, ATP binding to sites 1 and 2 promotes formation of an extended octamer where the tetramer is in the flat conformation. GTP binding to sites 2 and 3 promotes formation of a compressed octamer that prefers the bowed tetramer conformation. **b**, In the presence of ATP, IMPDH2 assembles extended filaments. Binding of GTP leads to the assembly of partially inhibited filaments where the tetramer is in a flat conformation. In the presence of very high GTP, the tetramer is completely inhibited and enters a bowed conformation that promotes disassembly of filament into free octamers. **c**, For canonical IMPDH1, binding of ATP drives assembly of a filament composed of extended octamers. In the presence of GTP, canonical IMPDH1 assembles into a filament with the small interface made of fully compressed octamers that are mostly inhibited and have the bowed tetramer conformation. **d**, For IMPDH1 retinal variant 595, the binding of ATP drives assembly of a filament composed of extended octamers. Binding of GTP drives assembly of a filament composed of compressed octamers that are partially inhibited and have the strained tetramer confirmation. In both filaments, the N-terminal extension adds buried surface area to the large interface and the C-terminal extension is disordered.

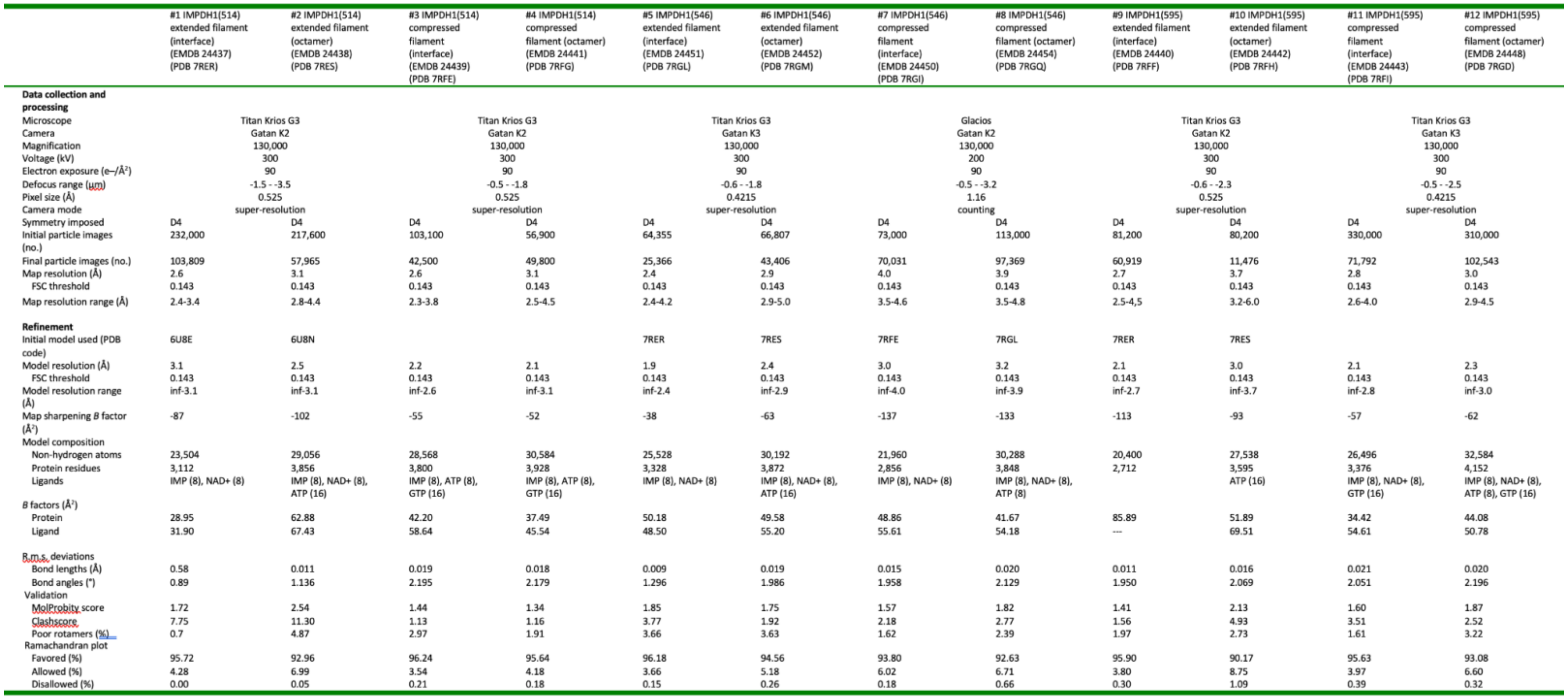

	#1 IMPDH1(514) extended filament (interface) (EMDB 24437) (PDB 7RER)	#2 IMPDH1(514) extended filament (octamer) (EMDB 24438) (PDB 7RES)	#3 IMPDH1(514) compressed filament (interface) (EMDB 24439) (PDB 7RFE)	#4 IMPDH1(514) compressed filament (octamer) (EMDB 24441) (PDB 7RFG)	#5 IMPDH1(546) extended filament (interface) (EMDB 24451) (PDB 7RGL)	#6 IMPDH1(546) extended filament (octamer) (EMDB 24452) (PDB 7RGM)	#7 IMPDH1(546) compressed filament (interface) (EMDB 24450) (PDB 7RGI)	#8 IMPDH1(546) compressed filament (octamer) (EMDB 24454) (PDB 7RGQ)	#9 IMPDH1(595) extended filament (interface) (EMDB 24440) (PDB 7RFF)	#10 IMPDH1(595) extended filament (octamer) (EMDB 24442) (PDB 7RFH)	#11 IMPDH1(595) compressed filament (interface) (EMDB 24443) (PDB 7RFI)	#12 IMPDH1(595) compressed filament (octamer) (EMDB 24448) (PDB 7RGD)
Data collection and processing												
Microscope	Titan Krios G3		Titan Krios G3		Titan Krios G3		Glacios		Titan Krios G3		Titan Krios G3	
Camera	Gatan K2		Gatan K2		Gatan K3		Gatan K2		Gatan K2		Gatan K3	
Magnification	130,000		130,000		130,000		130,000		130,000		130,000	
Voltage (kV)	300		300		300		200		300		300	
Electron exposure (e–/Å²)	90		90		90		90		90		90	
Defocus range (μm)	-1.5 - -3.5		-0.5 - -1.8		-0.6 - -1.8		-0.5 - -3.2		-0.6 - -2.3		-0.5 - -2.5	
Pixel size (Å)	0.525		0.525		0.4215		1.16		0.525		0.4215	
Camera mode	super-resolution		super-resolution		super-resolution		counting		super-resolution		super-resolution	
Symmetry imposed	D4	D4	D4	D4	D4	D4	D4	D4	D4	D4	D4	D4
Initial particle images (no.)	232,000	217,600	103,100	56,900	64,355	66,807	73,000	113,000	81,200	80,200	330,000	310,000
Final particle images (no.)	103,809	57,965	42,500	49,800	25,366	43,406	70,031	97,369	60,919	11,476	71,792	102,543
Map resolution (Å)	2.6	3.1	2.6	3.1	2.4	2.9	4.0	3.9	2.7	3.7	2.8	3.0
FSC threshold	0.143	0.143	0.143	0.143	0.143	0.143	0.143	0.143	0.143	0.143	0.143	0.143
Map resolution range (Å)	2.4-3.4	2.8-4.4	2.3-3.8	2.5-4.5	2.4-4.2	2.9-5.0	3.5-4.6	3.5-4.8	2.5-4,5	3.2-6.0	2.6-4.0	2.9-4.5
Refinement												
Initial model used (PDB code)	6U8E	6U8N			7RER	7RES	7RFE	7RGL	7RER	7RES		
Model resolution (Å)	3.1	2.5	2.2	2.1	1.9	2.4	3.0	3.2	2.1	3.0	2.1	2.3
FSC threshold	0.143	0.143	0.143	0.143	0.143	0.143	0.143	0.143	0.143	0.143	0.143	0.143
Model resolution range (Å)	inf-3.1	inf-3.1	inf-2.6	inf-3.1	inf-2.4	inf-2.9	inf-4.0	inf-3.9	inf-2.7	inf-3.7	inf-2.8	inf-3.0
Map sharpening *B* factor (Å²)	-87	-102	-55	-52	-38	-63	-137	-133	-113	-93	-57	-62
Model composition												
Non-hydrogen atoms	23,504	29,056	28,568	30,584	25,528	30,192	21,960	30,288	20,400	27,538	26,496	32,584
Protein residues	3,112	3,856	3,800	3,928	3,328	3,872	2,856	3,848	2,712	3,595	3,376	4,152
Ligands	IMP (8), NAD+ (8)	IMP (8), NAD+ (8), ATP (16)	IMP (8), ATP (8), GTP (16)	IMP (8), ATP (8), GTP (16)	IMP (8), NAD+ (8)	IMP (8), NAD+ (8), ATP (16)	IMP (8), NAD+ (8)	IMP (8), NAD+ (8), ATP (8)		ATP (16)	IMP (8), NAD+ (8), GTP (16)	IMP (8), NAD+ (8), ATP (8), GTP (16)
B factors (Å²)												
Protein	28.95	62.88	42.20	37.49	50.18	49.58	48.86	41.67	85.89	51.89	34.42	44.08
Ligand	31.90	67.43	58.64	45.54	48.50	55.20	55.61	54.18	---	69.51	54.61	50.78
R.m.s. deviations												
Bond lengths (Å)	0.58	0.011	0.019	0.018	0.009	0.019	0.015	0.020	0.011	0.016	0.021	0.020
Bond angles (°)	0.89	1.136	2.195	2.179	1.296	1.986	1.958	2.129	1.950	2.069	2.051	2.196
Validation												
MolProbity score	1.72	2.54	1.44	1.34	1.85	1.75	1.57	1.82	1.41	2.13	1.60	1.87
Clashscore	7.75	11.30	1.13	1.16	3.77	1.92	2.18	2.77	1.56	4.93	3.51	2.52
Poor rotamers (%)	0.7	4.87	2.97	1.91	3.66	3.63	1.62	2.39	1.97	2.73	1.61	3.22
Ramachandran plot												
Favored (%)	95.72	92.96	96.24	95.64	96.18	94.56	93.80	92.63	95.90	90.17	95.63	93.08
Allowed (%)	4.28	6.99	3.54	4.18	3.66	5.18	6.02	6.71	3.80	8.75	3.97	6.60
Disallowed (%)	0.00	0.05	0.21	0.18	0.15	0.26	0.18	0.66	0.30	1.09	0.39	0.32

Table 2.1: Cryo-EM data collection, refinement, and validation statistics

Chapter 3: IMPDH forms dynamic filaments in zebrafish retina

3.1 Introduction

Zebrafish are widely used to study human mutations causing retinal degeneration[76–83]. In this study, we provide fundamental information on *Impdh1* in the zebrafish retina. We determine the primary splice variant present in the retina and show its exclusive expression and ability to form filaments in rods and cones. We demonstrate biochemical and structural similarity between the zebrafish and human retinal variant of IMPDH1, uncover dynamic changes in photoreceptor filaments throughout the day, and use metabolomics to elucidate an important role for Impdh1 in purine nucleotide homeostasis in photoreceptors. Our study provides the foundation for using zebrafish to determine Impdh1 function in normal and diseased retina.

3.2 IMPDH expression in zebrafish retina

Using primers that recognize all reported major splice variants for *Impdh1a*, *1b*, and *2* (Table 3.1), we found that peak expression of *Impdh1a* and *Impdh1b* transcript levels in the zebrafish retina occur at different times during the day; *Impdh1a* shows highest expression at light onset (9 AM) and *impdh1b* peaks at dark onset (11 PM). To test whether expression patterns might be circadian, we also analyzed expression in fish retina in darkness after a 24 h dark incubation. In general, the changes in expression were maintained in constant darkness, however, there was a light-dependent increase in the expression for *Impdh1a*, which we did not detect for *Impdh1b*. *Impdh2* expression remained constant over a 24-h period (Fig. 3.1A)). Using the maximal mRNA levels for each gene (*1a*, *1b*, and *2*), we found that *Impdh1a* is the most abundant IMPDH transcript in the zebrafish retina, with more than 9-fold the level of *Impdh1b* and more than 32-fold the level of *Impdh2* (Fig. 3.1B).

We then used primer combinations of four *Impdh1a* splice variants listed in NCBI to determine which transcript is primarily expressed (Table 3.1). We found that the predominant transcript variant (tv) is X1, and we identified a new transcript which we designate as X4 (Fig. 3.1C,D). Using unique N-terminal and C-terminal primers to distinguish the predicted variants, we found that X1 is expressed ~150 times more than the X2 to 4. To further confirm our findings, we developed two antibodies that detect the C-terminus of X1, X3, and *Impdh1a* (544) and the N-terminus of X1 and X2. These antibodies are specific and verified that only the X1 (624 aa) variant is expressed at significant levels in the zebrafish retina (Fig. 3.1E). No protein was detected in the fish strain *Impdh1asa23234*, which contains a splice site mutation in *Impdh1a* that introduces a premature stop codon[84]. The diurnal change in mRNA expression was partially recapitulated in protein levels on Western blots (Fig. 3.1F).

3.3 Zebrafish retinal variant is similar to human retinal variant

Structural features and filament assembly properties are broadly conserved between zebrafish *Impdh1a* (544) and human IMPDH1[16] (Fig. 3.2A). Negative stain EM reveals that, like human IMPDH1, addition of ATP or GTP stimulates filament assembly of *Impdh1a*(544) and *Impdh1a_tvX1*. Both ATP and GTP drive assembly of filaments made of stacked octamers[25,27,30]. Previous studies have shown that IMPDH octamers are in an extended conformation in the active state, and that GTP binding induces a compressed and inactive conformation[15,16]. Similarly, both zebrafish *Impdh1a*(544) and *Impdh1a_tvX1* filaments are in the active/extended state with a rise 111 Å and 107 Å, respectively, when bound to ATP or the inhibited/compressed state with a rise of 86 Å and 100 Å, respectively, when bound to GTP. At this resolution, the zebrafish protein was very similar to the human retinal variants. The designed non-assembly point mutation Y12A breaks assembly of both *Impdh1a* variants[13,16,85].

Human IMPDH1 retinal variants include N- and C-terminal extensions that play significant roles in modulating GTP-feedback sensitivity and structure[16]. Zebrafish *Impdh1a*(544) includes the C-terminal extension but not the N-terminal extension, whereas *Impdh1a_tvX1* has both (Fig. 3.2B,C). Critical amino acids in both termini of the human retinal variants are conserved in the zebrafish proteins (Fig. 3.2B,C). Human IMPDH1 forms polymorphic filaments, whereas the N-terminal helix in the retinal spice variant IMPDH1(595) controls filament assembly and only permits one filament architecture that resists GTP inhibition[16]. This N-terminal helix is conserved in the zebrafish *Impdh1a_tvX1*, and we hypothesize the helix plays the same role in controlling assembly of the zebrafish protein. In humans, the C-terminal extension decreases sensitivity to GTP, but the mechanism of action is still unknown. The C-terminal end is conserved between human and zebrafish, which suggests a conserved function.

We found that zebrafish *Impdh1a_tvX1* resists GTP inhibition in a similar fashion to the human retinal variants[16] (Fig 3.2D). Zebrafish *Impdh1a* has an IC_{50} for GTP of 460 µM, whereas *Impdh1a_tvX1* is more than tenfold less sensitive to GTP, with an IC_{50} of 4900 µM. When the non-assembly mutation Y12A is introduced to *Impdh1a_tvX1*, the IC_{50} for GTP drops to near *Impdh1a* levels (780 µM). This pattern is similar to the human IMPDH1 retinal variant, in which the effect of the N-terminal extension on decreasing GTP sensitivity is dependent on filament assembly[16].

3.4 Zebrafish retinal variants forms filaments in photoreceptors

Using our antibody to the C-terminus of *Impdh1a_tvX1*, we next analyzed the cellular distribution of protein in the retina. We used immunohistochemistry (IHC) and high-resolution confocal imaging to localize *Impdh1a_tvX1* in WT zebrafish retinas. As in Western blots, our antibody was highly specific and labeled WT retinas (Fig. 3.3A) but not retinas from a fish strain with a splice site mutation, *impdh1asa23234* and consequently no IMPDH1a protein (Fig. 3.3B; also see Fig 3.1E[84]).

In WT retinas, *Impdh1a_tvX1* is expressed only in rods and cones (Fig. 3.3C,D). In both rods and cones, filaments are easily detected in the cell body and synapse and in outer segments of cones although at much lower levels (arrow pointing to outer segment filament, Fig. 3.3C'). The retina shown in Figure 3.3D,D' is bleached, so filaments in rod cell bodies (co-stained with rod marker 4C12 (magenta), and outlined with dotted white box) are visible and not hidden by melanin within the retinal pigment epithelium.

To quantify the relative expression levels of *Impdh1a_tvX1* in rods and cones, we used zebrafish mutants that lack cones[86] or rods due to degeneration[87]. Analysis by qPCR at a single time point determined that ~50% of the retina's *Impdh1a* transcript and ~27% of the retina's *Impdh1b* transcript is expressed in cones (Fig. 3.3E). As expected, the remaining ~50% *Impdh1a* expression is in rods (Fig. 3.3F). An insignificant amount of *Impdh2* is expressed in either rods or cones. Although the relative abundance in each cell type may change throughout the day, we conclude that *Impdh1a_tvX1* is robustly expressed in both rod and cone photoreceptors, consistent with our ability to easily detect filaments in both cell types.

3.5 Photoreceptor filaments are dynamic

The retinal variant of human IMPDH1 and zebrafish *Impdh1* (*Impdh1a_tvX1*) stabilizes a filament conformation that resists allosteric inhibition by GTP (Fig 3.2 and[16]). This suggests that filaments may dynamically localize to regions of high GTP demand. To analyze this, we quantified filament length throughout the inner segment (IS) portion of the cell at four different times of the day, 11 AM, 5 PM, 11 PM, and 5 AM, in both rods and cones. For the synapse, we quantified the overall change in fluorescence intensity at these timepoints because the high concentration of *Impdh1a_tvX1* in this region of the cell made it difficult to resolve filaments even with image deconvolution. We distinguished rods from cones using the 4C12 antibody (rods) and a transgenic strain expressing GFP specifically in cone photoreceptors (Fig. 3.4A and Table 3.2).

We detected Impdh1a_tvX1 in the IS of both rods and cones at all timepoints (Fig. 3.4B). In cones, Impdh1a_tvX1 aggregates were more elongated (filamentous) during the day and more rounded (circular) at night (Fig. 3.4C, left). In contrast, rod ISs had smaller changes in filament shape throughout the day (Fig. 3.4C, right), with the most elongated filaments at 5 PM. However, even at 5 PM, the filaments in rods tended to have higher circularity than in cones, indicating an overall increase in filament length in cone ISs compared with rod ISs (Fig. 3.4D). At the synapse, the overall fluorescence intensity of *Impdh1a_tvX1* decreased at night compared with daytime in both rods and cones (Fig. 3.4E,F). These results are summarized in a schematic in Figure 3.4G.

3.6 Loss of retinal variant alters nucleotide homeostasis

Given the abundance and selectivity of *Impdh1a_tvX1* in zebrafish photoreceptors, we hypothesized an important role for this enzyme. To determine this, we analyzed the essential splice site mutant *Impdh1asa23234* [84], which lacks the *Impdh1a* protein both in Western blots and in IHC (see Figs. 3.1E and 3.3B). Thus, the sa23234 allele generates a gene knock-out (*impdh1a* KO). We sequenced the *Impdh1asa23234* transcript and found, as predicted, that an intron was retained leading to a premature stop codon (Fig. 3.5A,B). Further, consistent with previous studies demonstrating negative feedback regulation of IMPDH transcription[88], we found a significant upregulation of *Impdh1asa23234* transcript in homozygotes (Fig. 3.5C). In contrast, *impdh1b* and *impdh2* expression were not substantially altered by the loss of Impdh1a protein (Fig. 3.5D,E).

The retinal layers were intact and photoreceptor size and organization appeared normal in the KO compared with WT at 18 months (Fig. 3.5F,M - left and middle panels). As a control, we verified that Impdh1a protein remained absent in the KO at this age (Fig. 3.5G). Cone photoreceptor number and outer nuclear layer (rod layer) thickness were not significantly different between WT and KO (Fig. 3.5I,J). This is consistent with near normal expression of a single rod and cone-specific transcript in KO compared with WT retina (Fig. 3.5K).

Because mitochondrial DNA replication continues in differentiated cells independent of nuclear DNA replication, we carefully analyzed photoreceptor mitochondrial morphology in IHC and transmission electron microscopy (TEM) in the KO compared with WT. Overall photoreceptor mitochondrial distribution, morphology, and cristae looked normal (Fig. 3.5H,M right). We also did not detect changes in mitochondrial DNA copy number using qPCR in either fed or fasted animals (Fig. 3.5L).

To determine whether there was an imbalance in purine nucleotide synthesis pathways (Fig. 3.6A), we compared total metabolite levels in retinas from *impdh1a* KO with WT (Fig. 3.6B,C). We found a striking imbalance in purine nucleotides consistent with the predominant expression of this rate limiting enzyme. Guanine levels were reduced by more than 2-fold, but remarkably the steady state cGMP levels under ambient illumination were not affected. Increases in ribulose 5-phosphate also suggest that nucleotide synthesis pathways are disrupted because of the loss of *impdh1a*.

3.7 Discussion

The main findings from our study are the following: (1) *Impdh1a_tvX1* is the most abundant *impdh* transcript in zebrafish retina, (2) key structural and biochemical features are conserved between the zebrafish and human predominant retinal isoforms, (3) in retina, Impdh1a_tvX1 is only present in rods and cones where it forms abundant and dynamic filaments, and (4) loss of Impdh1a function significantly alters nucleotide balance in retina but does not cause degeneration. Zebrafish are firmly established as a powerful genetic model with highly conserved photoreceptor physiology[89,90]. Our new and significant findings presented here provide the foundation to genetically dissect the cause of IMPDH1-induced retinopathy using zebrafish.

Based on previous work[85,91,92], we predicted that zebrafish photoreceptors primarily express Impdh1a, however, none of these studies determined which transcript variant predominates. We sought to identify the specific transcript expressed because tissue and cell-type specific functions often depend on the expressed isoform[93,94]. Gene duplications, which are common in zebrafish, provide gene specialization (subfunctionalization)[95]. Our findings presented in Figures 3.1 and 3.3 show that for the study of Impdh1 in the retina, the zebrafish offers excellent cell class specificity of gene expression; we detect a predominant single transcript variant (X1) of *impdh1a* that is expressed specifically in rods and cones. In contrast, the *impdh1b* gene is more broadly expressed throughout the zebrafish[85] and at lower levels in the retina. We also confirm that in the retina, the Impdh1 paralogs show alternating circadian patterns of expression with nearly tenfold daily changes, whereas Impdh2 does not[91]. Although protein levels showed a similar trend, the changes are smaller than for mRNA consistent with the complicated temporal and spatial relationships between protein and mRNA levels[96].

We have demonstrated that key structural and functional properties of IMPDH1 splice variants are conserved between the well-characterized human enzyme and zebrafish. Human IMPDH1 assembles polymorphic filaments upon binding the allosteric effectors ATP and GTP[16,96]. These structural features are conserved in zebrafish *Impdh1a* and *Imph1a_tvX1*, and the point mutation Y12A disrupts assembly in both species, suggesting that the assembly mechanism is also conserved (Fig. 3.2A). In humans, IMPDH1 retinal splice variants have specific structural features in the N- and C-terminal splice extensions that reduce sensitivity to GTP inhibition. These sequences are conserved in zebrafish, with the C-terminal extension part of Impdh1a (544) and the N-terminal extension added in the splice variant Impdh1a_tvX1 (Fig 3.2B,C). In humans, the effect of the N-terminal extension in reducing GTP sensitivity is dependent on filament assembly, as it functions to bias assembly into a hyperactive filament conformation[16]. To test conservation of this property, we introduced the non-assembly Y12A mutation in Impdh1a_tvX1 and found that this increased sensitivity to GTP to the level of Impdh1a, which lacks the N-terminal extension, indicating that the effect of the N-terminal extension is dependent on polymerization of the zebrafish enzyme (Fig. 3.2D). Thus, the regulation of Impdh1a_tvX1 by polymerization and N- and C-terminal extensions mirrors their effects in human IMPDH1, bolstering the case for the zebrafish retina as a relevant and appropriate model to study the role of IMPDH1 in the retina.

Impdh1a_tvX1 forms robust filaments in both rods and cones (Figs. 3.3 and 3.4). This is consistent with recent findings in mice and zebrafish[14,52,85] although Impdh filaments, as measured by the appearance of aggregates, were only detected in mouse photoreceptors after exposure to bright light and then only in outer segments and not elsewhere in the cell [52]. This increase in filaments within the outer segment correlated with elevated cGMP synthesis in the whole retina and led Plana-Bonamaisó *et al.*[52] to propose that filaments in photoreceptor outer segments are required for continued cGMP production during phototransduction. Recent work with the human retinal variant and our work presented here on the zebrafish retinal variant (Fig. 3.2) show that filaments favor a conformation that resists GTP inhibition, which would be predicted to increase guanine synthesis[16].

Here, we detailed filament dynamics during normal day-night light cycles (Fig. 3.4). Our results show that under normal lighting conditions, few filaments were detected in outer segments. In contrast, the filaments are abundant in synapses and throughout the cell body, around both the nucleus and mitochondria in both rods and cones. These results suggest an important role for nucleotide synthesis throughout the cell, consistent with the role of guanine nucleotides in many cellular processes and the robust vesicular trafficking characteristic of photoreceptors. In *Xenopus laevis*, 80 million rhodopsin molecules are transported/day from the inner to outer segment[97], and synaptic vesicle release in photoreceptors is graded thus requiring large numbers of vesicles[98]. However, the recycling of guanine nucleotides that occurs in these processes and in phototransduction might not require significant new synthesis of guanine. Filament formation could also provide a scaffold to organize signaling molecules[72]. Increased filaments in cones during the day could support more guanine synthesis and is consistent with the extended photopic range of cones compared with rods[99]. Reduced filament signals at night at the synapse could reflect the known disassembly of the ribbon that occurs in zebrafish cone pedicles[100].

The overall morphology of the Impdh1a KO retina using IHC and TEM appeared largely normal (Fig. 3.5). We demonstrate that this is not because of increased transcription of either *impdh1b* or *impdh2*. This suggested that either *impdh1a* is not responsible for significant guanine production in photoreceptors or that although guanine production is perturbed in the KO, the photoreceptors are able to regulate the key signaling molecule associated with cell degeneration, cGMP. To analyze the importance of *impdh1a* contribution to guanine production, we conducted metabolomic analyses comparing WT and *impdh1a* KO retinas. We detected large changes in guanine in KO retinas compared with WT, consistent with a significant role for Impdh1a_tvX1 in *de novo* purine synthesis in photoreceptors, but notably cGMP levels were normal (Fig. 3.6). We also found no change in mtDNA copy number due to the reduced guanine levels in the KO, even when guanine was potentially removed as a food source in fasted animals. Previous work in mice found that the loss of Impdh1 also did not cause significant loss of photoreceptors at least through 10 months, although ERGs revealed a reduction in the dark-adapted a-wave responses starting at 5 months[49]. A careful physiological analysis done at different ages under different illumination conditions may also reveal subtle changes in the photoresponse in the zebrafish KO. The increase in ribulose-5-phosphate may reflect a change in nucleotide metabolism from the pentose phosphate pathway. The key enzymes such as phosphoribosylpyrophosphate synthetase and amidophosphoribosyltransferase are inhibited by both guanine and adenine containing nucleotides[101]. Future experiments analyzing metabolic flux with different fuels will dissect the regulation of purine synthesis in photoreceptors.

Gene amplification

Target/NCBI reference sequence	Forward Primer (5' □ 3')	Reverse Primer (5' □ 3')
impdh1a/NM_001002177.1	ACAGAGAACAGATTGGTGGATCCATGGCTGATTACCTGATCAGCGG	GAGTGCGGCCGCTTAGCTGCTGTGTTTAGTGACGGC
impdh1b/NM_001014369.2	ACAGAGAACAGATTGGTGGATCCATGGCAGACTATCTGATAAGCGGAGGAA	GAGTGCGGCCGCTTAGTAAAGACGCTTCTCGAAGGAGTGAAGTC
impdh2/NM_201464.1	ACAGAGAACAGATTGGTGGATCCATGGCGGACTATTTAATCAGCGG	CTCGAGTGCGGCCGCTTAAAACAGGCGCTTCTCATAGCTGT
impdh1a_tvX1/XM_005159004.4 *impdh1a_tvX2*/XM_005159008.4	TTTGGGGAAATCAGTCCAAC	GAAGCCCGAACAAAACAAAA
impdh1a_tvX3/XM_009293441.2	GAAGCCCGAACAAAACAAAA	GGAGACCCTTCATCCACAGC
impdh1a_tvX4/MZ851785	GGAGACCCTTCATCCACAGC	GTTGAGAAATGAGCGCCTCT

Genotyping

Target/NCBI reference sequence	Forward Primer (5' □ 3')	Reverse Primer (5' □ 3')
impdh1a^sa23234	GACGCCACTCATTTCCTCTC	CTTTCCGGACCTCGTTAGC
rho^fl9	CCCTTCGAAGAGGAAGAGG	TCGAGAGTGTCTGGAAGGAGA

qPCR

Target/NCBI reference sequence	Forward Primer (5' □ 3')	Reverse Primer (5' □ 3')
impdh1a (all variants)	CATTGCAGGAATTCAACACG	GAACTCCACCCTCAACCTGA
impdh1b (all variants) Set 1	AGCAAACTAGTCGGCATCGT	GGCAGGAGCGACTACAAGAT
impdh1b (all variants) Set 2	ATCTGATAAGCGGAGGAACG	CCAGGCAAGATCAGGAAGTC
impdh2 (all variants)	TCTGGAGACGGCCTTACCTA	ATAGGCGACGAGATCAGTGG
impdh1a_tvX1 & *X2* (N-term)	AATGGCCCGTTTACTCACAG	GTAATCAGCCATGCTCTCTGG
impdh1a_tvX3 & *X4* (N-term)	GGCGAATATTCAGCAGAAGG	ATCACCGATGGCAAAGAGTT
impdh1a_tvX1 & *X3* (C-term)	CATTGCAGGAATTCAACACG	TAAATGGCAAAAAAGAATATGA
impdh1a_tvX2 & *X4* (C-term)	CATTGCAGGAATTCAACACG	ATAACCGTTTCTCGTAAGAAT
es1 NM_131039.1	TCACAACACCCGTGAACCTT	GGTCTCCCACATGAAGGTCG
gnat1 NM_131868.2	AGTGCATACGACATGGTGCT	GATGTGGTGGCGAAGTAACG

Table 3.1: Primers

Name	Target	Species	Clonality	Manufacturer	Catalog #	IHC Dilution	WB Dilution
Impdh1aC	Impdh1a C-terminus	Rabbit		in-house	N/A	1:5000	1:500
Impdh1aN	Impdh1a N-terminus	Rabbit		in-house	N/A	N/A	1:500
4C12	unknown rod epitope	Mouse	mAb	Fadool lab	gift	1:200	1:200
MTCO1	complex IV mitochondria	Mouse	mAb	Abcam	ab14705	1:1000	1:1000
GFP	transgenic GFP	Chicken	pAb	Abcam	ab13970	1:5000	N/A
HOESCHT	nuclei			Invitrogen	H3569	5 uM	N/A

Table 3.2: Antibodies/dyes

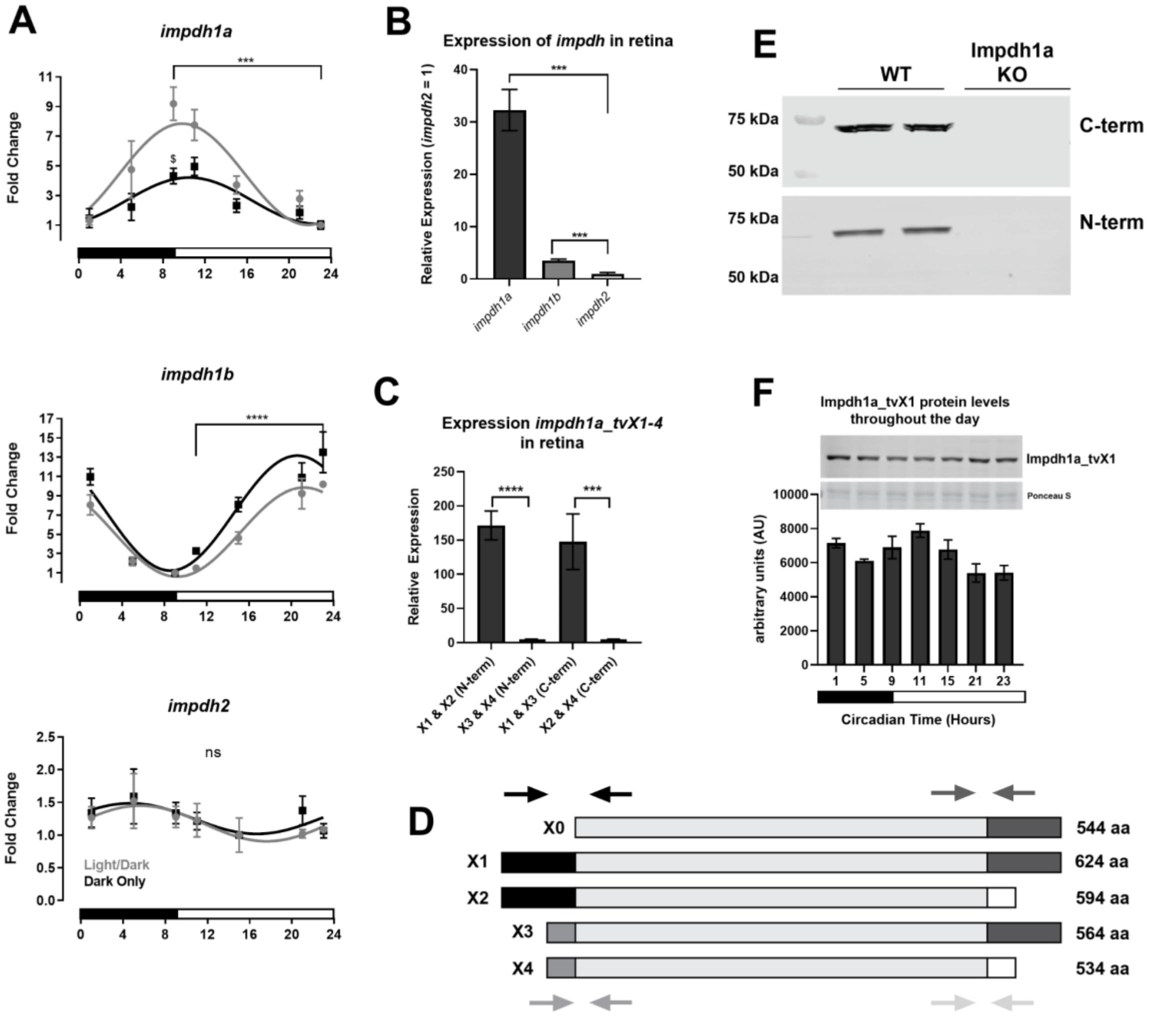

Figure 3.1: *Impdh1a_tv1a* is the predominant variant in the retina

A, relative expression levels of all transcript variants for *impdh1a*, *1b*, and *2* throughout the day. For each graph, minimum expression = 1: *impdh1a* timepoints measured relative to 23:00, *impdh1b* relative to 9:00, and *impdh2* relative to 15:00. The *black* and *white bars* indicate lights on (9:00) and lights out (23:00) for animals under normal light/dark cycle, \$ denotes $p \leq 0.05$ normal light/dark compared with dark only at 9:00. ***B***, comparison of relative maximum expression levels of *impdh1a (9:00)*, *1b (23:00)*, and *2 (5:00)* transcripts. ***C***, comparison of relative expression levels for all *impdh1a* transcripts detected in the retina at 9:00. N = 6 animals, the samples were in triplicate. ***D***, schematic of *impdh1a* transcripts X1 to X4 and 544 (X0, NM_001002177.1); primer location for (*C*) indicated by *arrows* for both C-terminal and N-terminal reactions. See Table 1 for primer/transcript information. ***E***, Western blot of Impdh1a protein in WT and *impdh1a23234* zebrafish retinas using antibodies that recognize either X1 and X3 (C-terminal) or X1 and X2 (N-terminal) N = 2. ***F***, quantification of Impdh1a_tvX1 protein levels throughout the day using the C-terminal antibody, and *inset* shows representative Western blot with Ponceau S used as a loading control. Trend $p = 0.04$, N = 2 animals per time point. N = 3 animals per time/data point for all other panels except where noted. impdh, inosine monophosphate dehydrogenase; tv, transcript variant. ns $p > 0.05$, $* \ p \leq 0.05$, $** \ p \leq 0.01$, $*** \ p \leq 0.001$, $**** \ p \leq 0.0001$.

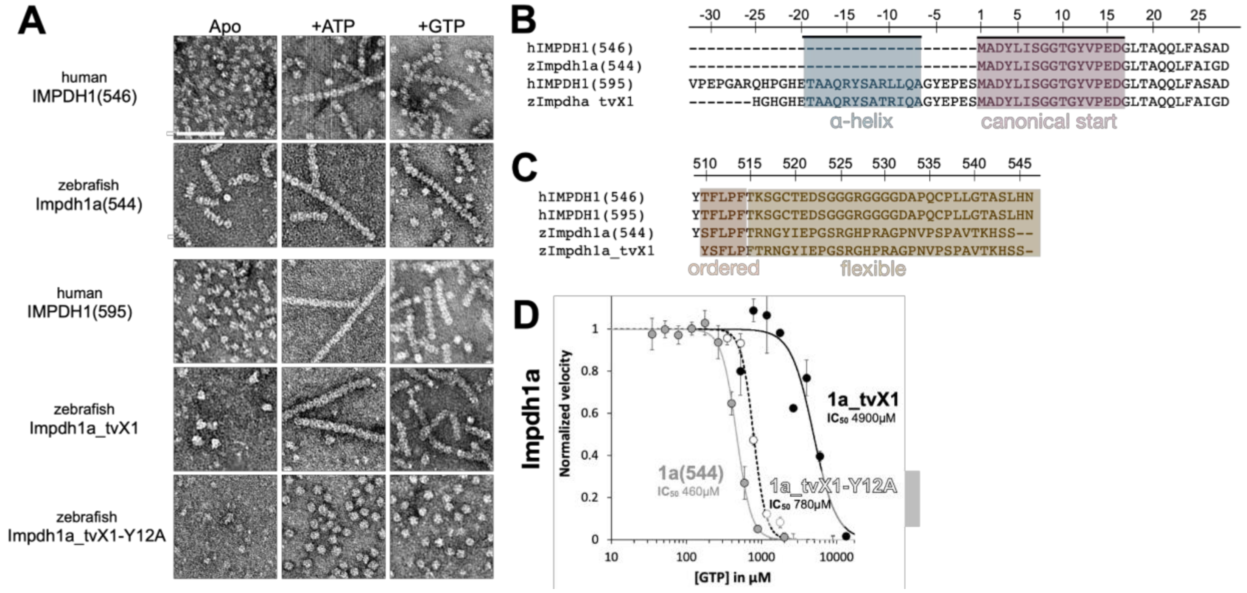

Figure 3.2: Structural & function conservation between zebrafish and human IMPDH1

A, negative stain EM of purified human retinal variants IMPDH1(546) & IMPDH1(595) and zebrafish Impdh1a (544) & Impdh1a_tvX1. The scale bar represents 100 nm. ***B*** and ***C***, sequence alignment of human retinal variants IMPDH1(546) and IMPDH1(595), zebrafish Impdh1a (544) NM_001002177.1, and zebrafish retinal variant Impdh1a_tvX1 (XM_005159007.4). ***B***, conserved N-terminal alpha-helix in *blue* and gene beginning in *pink*. ***C***, residues in *orange* (ordered) are resolved in cryo-EM structures of the human protein (9), remainder of C-terminus in *yellow* is flexible and not resolved in structures (9). ***D***, GTP-inhibition curves of zebrafish Impdh1a (544) (*solid gray line*), Impdh1a_tvX1 (*solid black line*), and non-assembly Y12A protein (*dashed black line*). Each data point represents a triplicate and the error bars are standard deviation. impdh, inosine monophosphate dehydrogenase; tv, transcript variant.

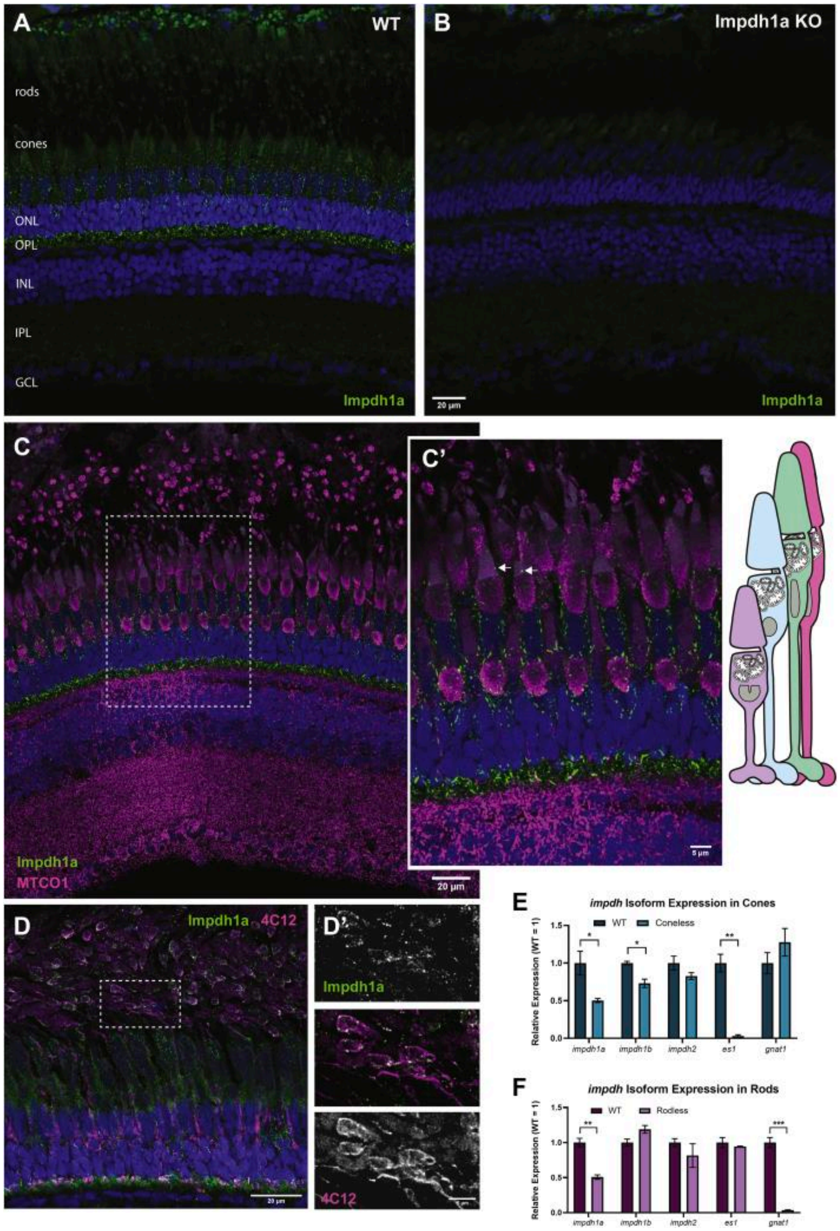

Figure 3.3: *Impdh1a_tvX1* is expressed exclusively in rods and cones
A, representative IHC images showing Impdh1a staining of WT and (***B***) KO adult zebrafish retina at 11:00 AM using the C-terminal antibody. ***C***, Impdh1a (*green*) and MTCO1 (*magenta*) immunostaining of WT-pigmented retina. The nuclei are *blue*. ***C'***, magnified section of image in (***C***) showing Impdh1a filament localization in cones. The *arrows* indicate where Impdh1a filaments appear to form in the OS. Note the tiering of photoreceptors normal in adult zebrafish retina. ***D***, representative Impdh1a staining (*green*) and 4C12 (*magenta*) of bleached retina showing the localization of Impdh1a with known zebrafish rod marker. The nuclei are stained *blue*. ***D'***, magnified section of (***D***) showing overlap of Impdh1a with 4C12 (rod) staining. *E*, qPCR quantification of *impdh1a*, *1b*, and *2* transcripts in coneless retina and (***F***) qPCR analysis of relative *impdh1a*, *1b*, and *2* expression in rodless retina. *es1* and *gnat1* are cone and rod specific genes, respectively. N = 3 animals and the error bars are standard error. IHC,

immunohistochemistry; impdh, inosine monophosphate dehydrogenase. ns $p > 0.05$, * $p \leq 0.05$, ** $p \leq 0.01$, *** $p \leq 0.001$.

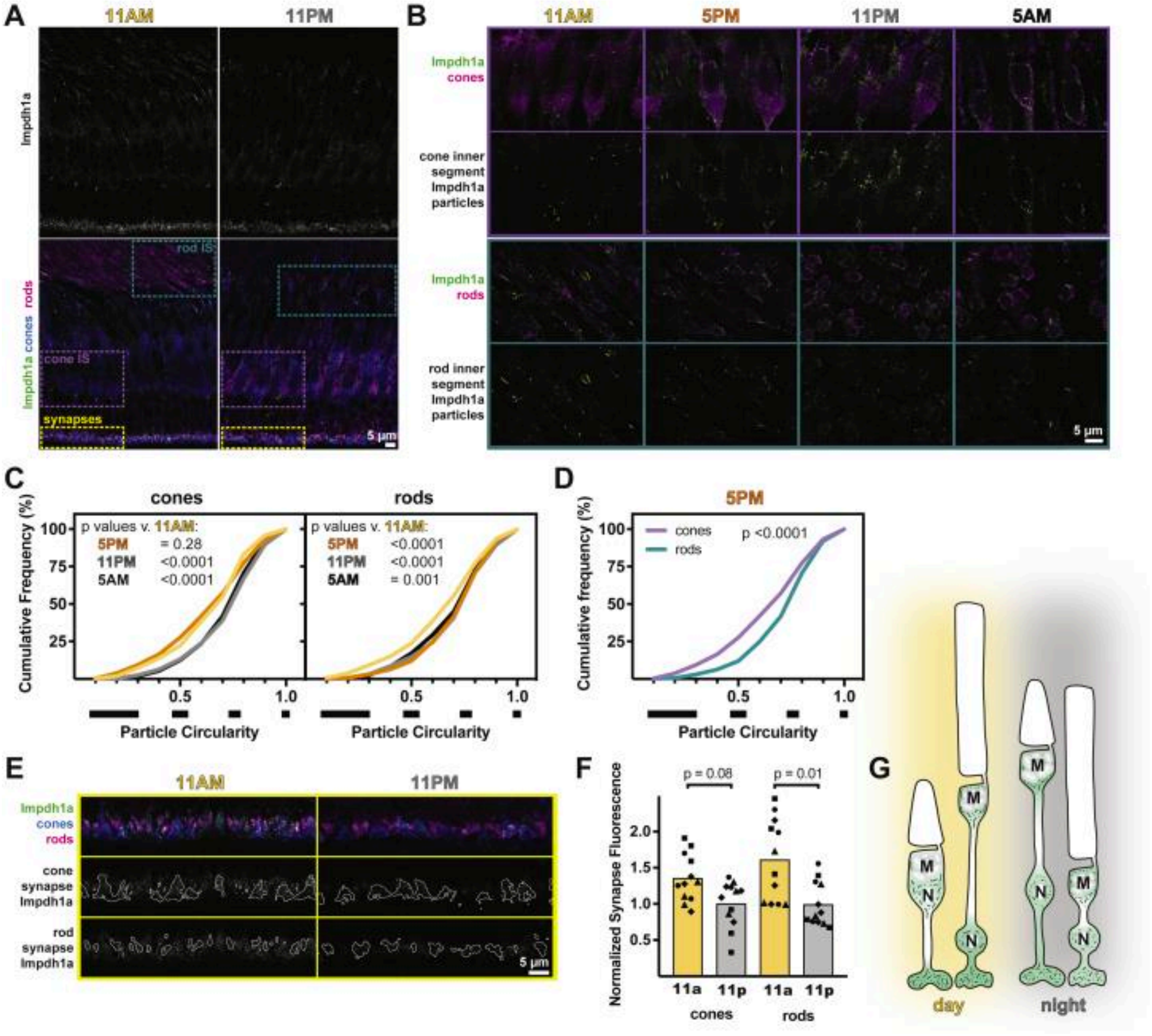

Figure 3.4: *Impdh1a* localization in photoreceptors is dynamic

A, representative IHC images of zebrafish outer retina at 11 AM and 11 PM stained with antibodies against Impdh1a (*top white* and *bottom green*) and colabeled (*bottom panels*) with transgenic cone-targeted GFP (*blue*) and rods (4C12, *magenta*). ***B***, detailed IHC images of photoreceptor inner segments throughout the day. Impdh1a (*green*) counterstained with cone or rod markers (*magenta*). ***C***, cumulative frequency distributions of particle circularity ratios in rods and cones throughout the day. N = 4 animals, three experiments each. ***D***, comparison of particle circularity ratios in cones and rods at 5 PM. *E*, detailed IHC images of photoreceptor synapses at 11 AM and 11 PM. *Top*, Impdh1a (*green*) counterstained with cone (*blue*) or rod (*magenta*) markers. *Middle* and *bottom*, Impdh1a signal overlapping with cone or rod synapse masks, respectively. ***F***, quantification of mean synapse fluorescence in cones and rods at 11 AM and 11 PM, normalized to 11 PM. Each symbol is a different animal, three experiments for each animal.

G, hypothesized model for Impdh1a dynamics throughout the day. In daytime, longer Impdh1a filaments occupy the inner segments, surrounding mitochondrial clusters (M) and nuclei (N). More subtle changes occur at synapses, with slightly reduced Impdh1a immunoreactivity at night. IHC, immunohistochemistry; impdh, inosine monophosphate dehydrogenase.

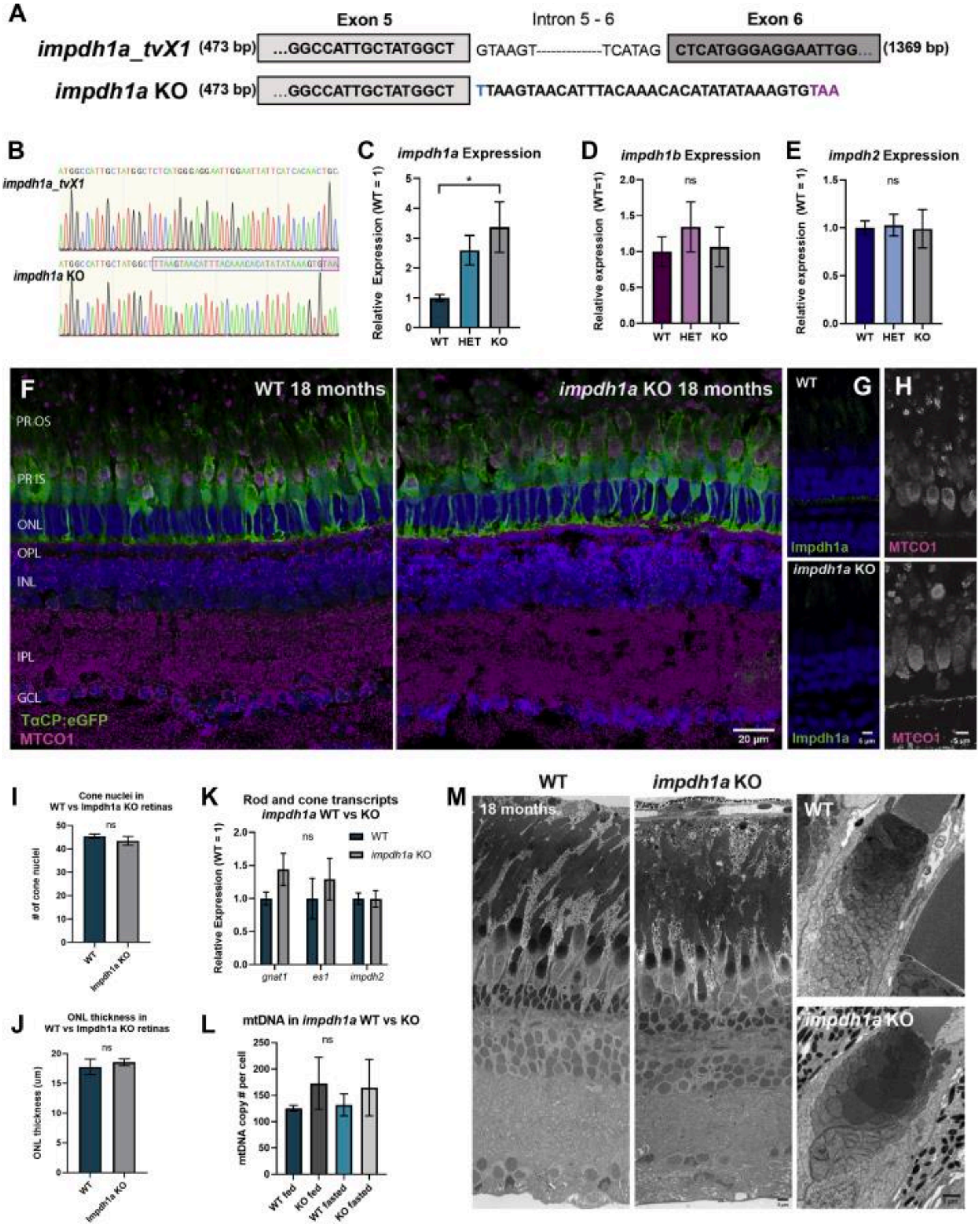

Figure 3.5: Loss of *impdh1a* does not alter the expression of *impdh1b* or *impdh2* and does not cause photoreceptor degeneration

A, schematic of *impdh1a* KO mutation, a G > T mutation at essential splice site between exon 5 and 6 resulting in a premature stop codon 11 amino acids after exon 5. ***B***, primary sequence of *impdh1a*_tvX1 compared with *impdh1a* KO. *Blue* marks start of retained intron, *purple* marks premature stop codon in *impdh1a* KO. qPCR analysis of (***C***) *impdh1a*, (***D***) *impdh1b*, and (***E***) *impdh2* transcripts at 11:00 AM in WT, HET, and *impdh1a* KO retinas. N = 6 for WT and heterozygous animals and N = 5 for KO animals. ***F***, representative IHC images of 18 month old *impdh1a* WT and KO retinas with mitochondria (MTCO1) stained *magenta*. Cone photoreceptors express eGFP under the cone transducin promotor *(TaCP:eGFP)* and are stained with eGFP antibody to visualize cones (*green*). The nuclei are stained in *blue*. The images are maximum intensity projections of 20 stacks 0.3 µm per step. ***G***, control demonstrating lack of Impdh1a protein at 18 months in *impdh1a* KO retinas. ***H***, mitochondrial (MTCO1) staining of *impdh1a* WT and KO retinas showing normal mitochondrial localization and morphology in the KO retina at 18 months. *I*, cone nuclei quantification and (***J***) outer nuclear layer thickness (rod nuclei) comparing *impdh1a* WT and KO zebrafish retinas at 18 months. *K*, rod- (*gnat1*) and cone- (*es1*) specific transcripts in WT compared with KO. *impdh2* transcript, which is not found in rod or cones, used as a control. N = 5 animals for WT and N = 3 animals for KO. *L*, whole retina mtDNA copy number after feeding or after 18 to 24 h fasting; N = 3 for all the samples. *M*, representative TEM images of 18 month old WT and KO retinas showing high resolution morphology of retinal layers (*left* and *middle panel*) and mitochondria (*right*) in 18 months *impdh1a* WT and KO retinas. impdh, inosine monophosphate dehydrogenase; tv, transcript variant. ns $p > 0.05$, $* p \leq 0.05$.

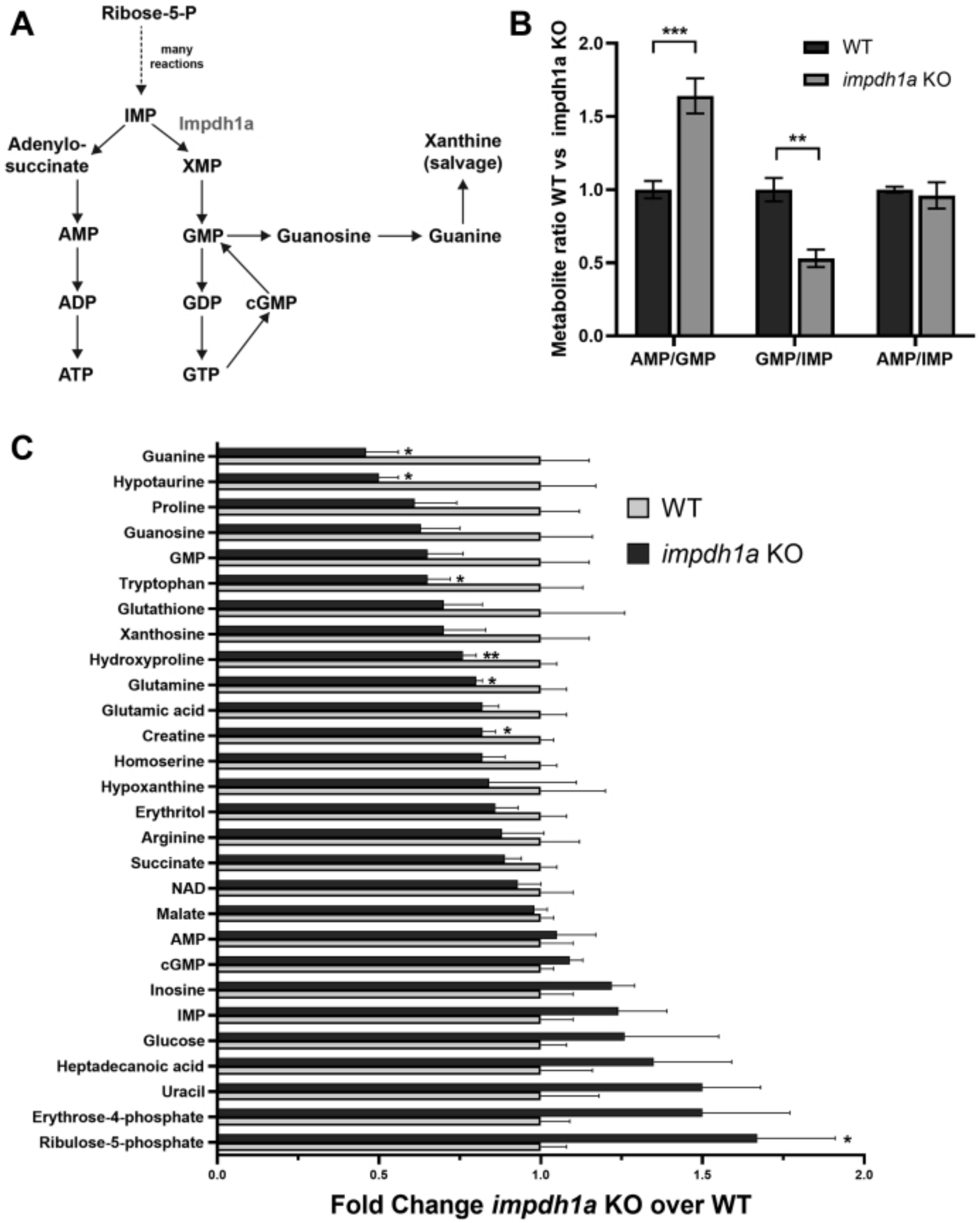

Figure 3.6: Steady state guanine levels are dramatically reduced in *impdh1a* KO retinas
A, a schematic of purine nucleotide synthesis pathway. ***B***, the ratio of metabolites directly connected to Impdh enzyme activity. ***C***, quantification from LC/MS/MS analysis of a subset of relevant metabolites and metabolites at 11:00 AM with significant changes between WT and *impdh1a* KO. The experiment was repeated twice, total N = 5 or 6 animals, and the error bars are standard error. impdh, inosine monophosphate dehydrogenase. ns $p > 0.05$, $* \ p \leq 0.05$, $** \ p \leq 0.01$, $*** \ p \leq 0.001$.

Chapter 4: Molecular mechanism of IMPDH1-associated blindness

4.1 Retinopathy mutations fall into two functional classes

Previous studies have looked at the effect of retinitis pigmentosa mutations in canonical IMPDH1 and disease mutation D226 in both retinal variants and found there is no effect on substrate kinetics[49,68], but a subset of mutations disrupt GTP regulation[14]. Since disease only occurs in the retina, where there is no expression of canonical IMPDH1[102], and given the large differences in GTP regulation we observed with splice variants, we wondered whether the mutations had specific effects in the retinal splice variants. We tested the mutant forms of canonical and retinal IMPDH1 variants for nine known retinitis pigmentosa mutations. Our findings for canonical IMPDH1 confirm the previous results[14]. We repeated these experiments with the retinal variants and found the effects of each mutation were similar in the variants and canonical IMPDH1, with several mutations affecting GTP regulation. Thus, in IMPDH1 splice variants, we can describe two classes of disease mutants. Mutations that are insensitive to GTP inhibition we describe as class I, which consists of five mutations around the third allosteric site that is specific for GTP (Fig. 4.1a-d and Supp. Table 4.1). Class I mutations are N198K, R231P, R224P, D226N and K238E. Class II mutations are located at four positions more distal to the allosteric sites and had a GTP inhibition response nearly identical to WT (Fig. 4.1e-g and Supp. Table 4.1). Class II mutations include R105W, T116M, V268I and H372P. The similar effects of disease mutants in all variants of IMPDH1 suggests that they likely have the same effect at the enzyme level across all tissues expressing IMPDH1.

Class II mutations do not have an effect on biochemical activity, so we wondered whether the reason they cause disease might be instead due to an effect on filament assembly.

We performed negative stain EM in the presence of ATP, substrates and inhibitory concentrations of GTP (Supp. Fig. 4.1). Under this condition, all three WT variants assemble filaments of compressed octamers. Four of the five class I mutants form filaments in all variants, but are made up of extended/flexible octamers, which agrees with their inability to be inhibited by GTP. The only class I mutation that is different is R224P. IMPDH1(514)-R224P forms compressed filaments similar to WT, whereas R224P in both retinal variants does not assemble into filaments (Supp. Fig. 4.1), which agrees with previous findings that IMPDH1(514)-R224P has a reduced propensity for forming ultrastructures in cells[31]. In this condition, the class II mutations form filaments that are indistinguishable from WT in negative stain EM. The lack of obvious in vitro biochemical or structural phenotypes for class II mutations suggests they may lead to misregulation in vivo that is dependent on other cellular factors.

4.2 Transgenic zebrafish development

To understand blindness-associated IMPDH1 mutations in the context of the retina, we developed 5 transgenic zebrafish lines. All lines express Impdh1a_tvX1 including WT, two class I mutations (K238E, D226N), and two class II mutations (V268I, H372P) under the cone promoter TaCP[103].

4.3 Characterization of transgenic lines

For an initial characterization of the transgenic zebrafish lines, we performed IHC to identify any large changes to retina architecture or protein expression (Fig. 4.2). The transgenic line expressing myc tagged Impdh1a_tvX1-WT showed similar retinal architecture and protein distribution compared to a WT sibling (Fig. 4.2A,B) demonstrating that overexpression of Impdh1a_tvX1-WT alone does not cause degeneration. Lines expressing D226N (Fig. 4.2C) and K238E (Fig. 4.2D) show accumulation of Impdh1a-TvX1 in the synapse and large ultrastructures through the cell body. In addition, lines expressing K238E show a marked loss of cones in IHC and Western (Supp. Fig. 5.1) indicating that expression of this mutation leads to cone photoreceptor death recapitulating what is seen in human disease - confirming we have established an animal model to study IMPDH1-associated retinal degeneration.

More thorough characterization of these lines in addition to the class II mutation lines is ongoing.

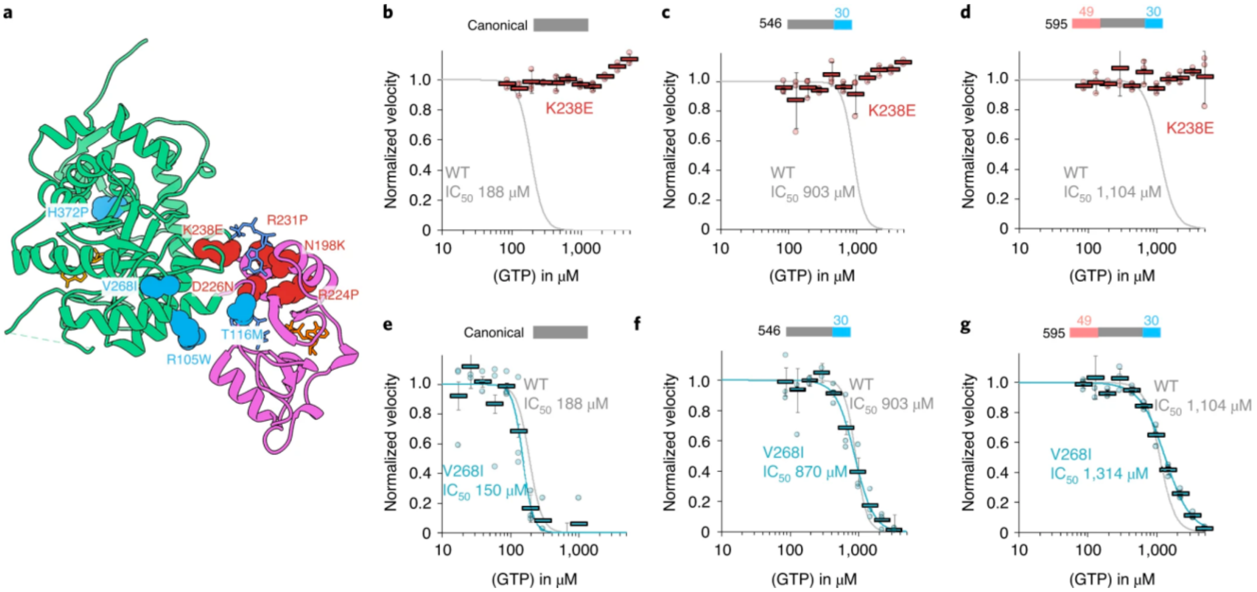

Figure 4.1: IMPDH1 retinopathy mutations fall into two classes.
a, IMPDH1 with catalytic domain (green), regulatory domain (pink), NAD^+ (gold), GTP (blue) and ATP (orange). Class I (defective in GTP regulation) residues colored coral. Class II residues (normal GTP regulation) colored teal. **b–g**, GTP inhibition curves of IMPDH1 retinopathy mutant variants (colored lines) compared to IMPDH1-WT variants (gray lines). Reactions performed with 1 μM protein, 1 mM ATP, 1 mM IMP, 300 μM NAD^+ and varying GTP. Individual data points for mutants are shown as circles. Reactions were performed in triplicate and the average for each concentration is shown as a bold rectangle (gray WT, red K238E, teal V268I). Error bars show the standard deviation for $n = 3$. Individual data points and averages for WT are in Fig. 2.1d. **b**, Canonical IMPDH1(514)-K238E. **c**, Retinal variant IMPDH1(546)-K238E. **d**, Retinal variant IMPDH1(595)-K238E. **e**, Canonical IMPDH1(514)-V268I. **f**, Retinal variant IMPDH1(546)-V268I. **g**, Retinal variant IMPDH1(595)-V268I.

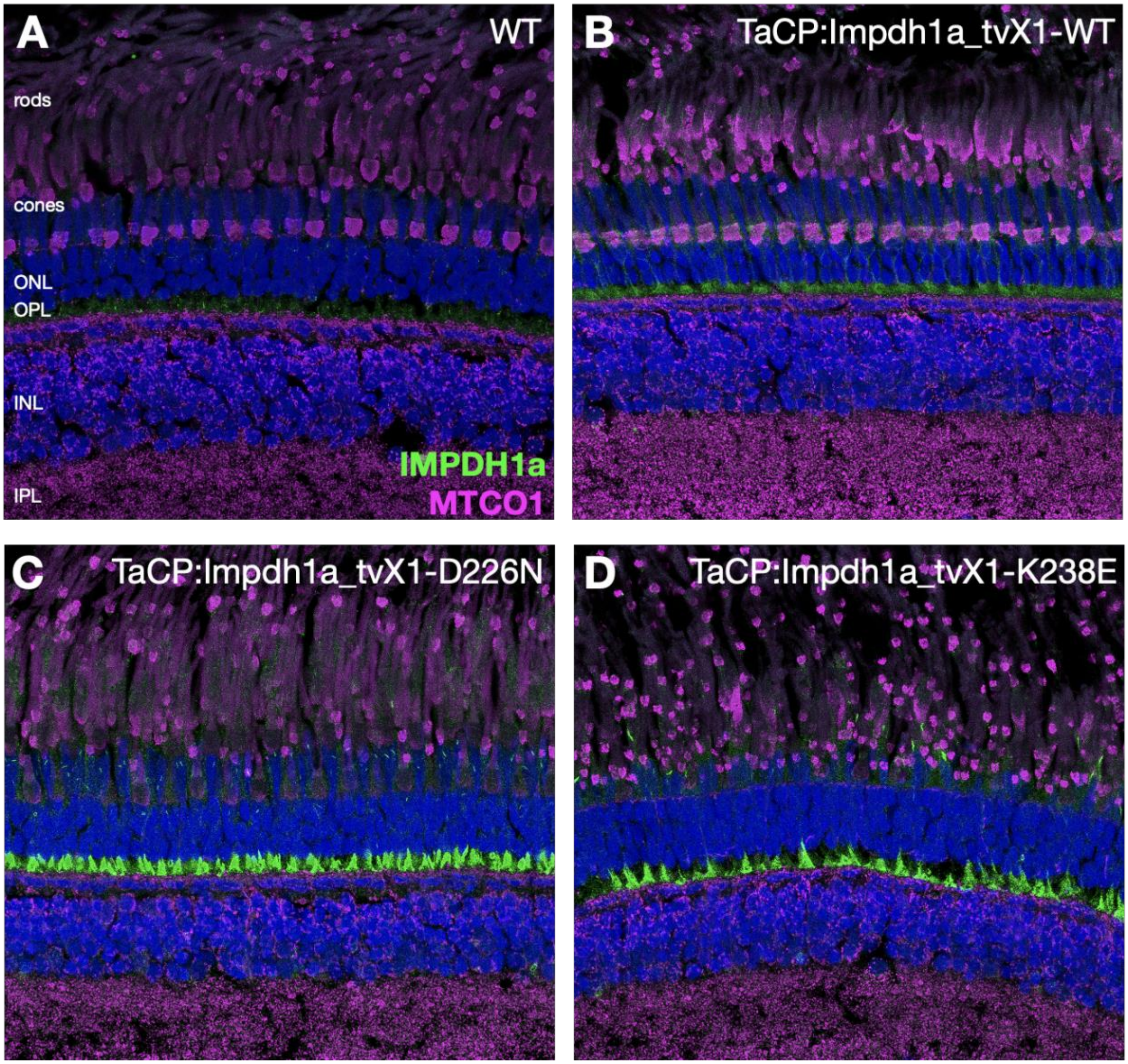

Figure 4.2: Impdh1a_tvX1 protein accumulation in mutant transgenic retinas
Representative IHC images of zebrafish retinas showing Impdh1a (green), MTCO1 (green), and nuclei (blue). **A,** 7.5 month WT sibling of fish in **C. B**, 2.5 month transgenic fish expressing TaCP:Impdh1a_tvX1-WT. **C**, 7.5 month transgenic fish expressing TaCP:Impdh1a_tvX1-D226N. **D**, 4.5 month transgenic fish expressing TaCp:Impdh1a_tvX1-K238E

Chapter 5: Methods

5.1 Recombinant IMPDH expression and purification

Purified IMPDH protein was prepared as described previously[13,15]. BL21 (DE3) *Escherichia coli* were transformed with a pSMT3-Kan vector expressing N-terminal 6xHis-SMT3/SUMO-tagged IMPDH. Cells were cultured in Luria-Bertani medium at 37 °C until reaching an optical density (OD_{600}) of 0.9 then expression induced with addition of isopropyl-β-D-thiogalactoside to 1 mM for 4 h at 30°C and pelleted. The remainder of the purification was performed at 4 °C. Pellets were resuspended in lysis buffer (50 mM KPO_4, 300 mM KCl, 10 mM imidazole, 800 mM urea, pH 8) and lysed with an Emulsiflex-05 homogenizer. Lysate was cleared by centrifugation and SUMO-tagged IMPDH chromatographically purified with HisTrap FF columns (GE Healthcare Life Sciences) and an Äkta Start chromatography system. After on-column washing with lysis buffer and elution (50 mM KPO_4, 300 mM KCl, 500 mM imidazole, pH 8), peak fractions were treated with 1 mg of ULP1 protease [104] per 100 mg IMPDH for 1 h at 4 °C, followed by the addition of 1 mM dithiothreitol (DTT) and 800 mM urea. Protein was then concentrated using a 30,000 molecular weight cutoff Amicon filter and subjected to size-exclusion chromatography using Äkta Pure system and a Superose 6 column pre equilibrated in filtration buffer (20 mM HEPES, 100 mM KCl, 800 mM urea, 1 mM DTT, pH 8). Peak fractions were concentrated using a 10,000 molecular weight cutoff Amicon filter, then flash-frozen in liquid nitrogen and stored at −80 °C.

5.2 IMPDH activity assays

Protein aliquots were diluted in activity buffer (20 mM HEPES, 100 mM KCl, 1 mM DTT, pH 7.0) and pretreated with varying concentrations of ATP, GTP and IMP for 30 min at 20 °C in 96-well ultraviolet transparent plates (Corning model 3635). Reactions (100 µl total) were initiated by addition of varying concentrations of NAD^+. NADH production was measured by optical absorbance (340 nm) in real time using a Varioskan Lux microplate reader (Thermo Scientific) at 25 °C, 1 measurement per min, for 15 min; absorbance was correlated with NADH concentration using a standard curve.

Specific activity was calculated by linear interpretation of the reaction slope for a 4-min window beginning 1 min after reaction initiation. All data points reported are an average of three measurements from the same protein preparation. Error bars are standard deviation. Fits for activity assays were calculated using the Hill–Langmuir equation $V = V_{max} \times [S]n/((K0.5)n + [S]n)$ and IC_{50} was calculated using a modified Hill equation $V = V_{min} \times (V_{max} - V_{min})/(1 + (I/IC_{50})^n$ [105]. Where V = reaction velocity, V_{max} = maximum reaction velocity, V_{min} = minimum reaction velocity, $[S]$ = substrate concentration, $K0.5$ = substrate concentration that gives half velocity of V_{max}, n = Hill coefficient, I = inhibitor concentration, IC_{50} = half-maximum inhibitory concentration.

5.3 Negatively stained EM

Protein samples were applied to glow-discharged continuous carbon EM grids and negatively stained with 2% uranyl formate as previously described[15]. Grids were imaged by transmission EM using an FEI Morgagni at 100 kV acceleration voltage and a Gatan Orius CCD. Micrographs were collected at a nominal x22,000 magnification (pixel size 3.9 Å).

5.4 Cryo-EM sample preparation and data collection

Protein preparations were applied to glow-discharged C-flat holey carbon EM grids (Protochips), blotted and plunge-frozen in liquid ethane using a Vitrobot plunging apparatus (FEI) at 4°C, 100% relative humidity as previously described[15]. High-throughput data collection was performed using an FEI Titan Krios transmission electron microscope operating at 300 kV (equipped with a Gatan image filter and postGatan image filter Gatan K2 or K3 Summit direct electron detector) and an FEI Glacios (equipped with a Gatan K2 Summit direct electron detector) both using the Leginon software package[106].

5.5 Cryo-EM image processing

Videos were collected in super-resolution mode, then aligned and corrected for beam-induced motion using Motioncor2, with 2x Fourier binning and dose compensation applied during motion correction[106,107]. Contrast transfer function (CTF) was estimated using GCTF[108]. Relion v.3.1 was used for all subsequent image processing[109,110]. Each dataset was individually processed but using approximately the same previously published strategy[15], with some variations from dataset to dataset.

First, for most datasets, autopicking templates and initial three-dimensional (3D) references maps were prepared by manually picking and extracting boxed particles from a small subset of micrographs and classifying/refining in two and three dimensions. For a few datasets, Cryosparc Live [111] was used for initial particle selection and two-dimensional (2D) classification. These particle coordinates were imported into Relion for 3D refinement. For these initial 3D refinements, a featureless, soft-edged cylinder was used as a refinement template of filaments. Because IMPDH filament segments possess D4 point-group symmetry, two different locations along filaments may be used as symmetry origins: the centers of canonical octamer segments, or the centers of the assembly interface between segments. For the filament datasets, we prepared and used autopicking templates centered on the filament assembly interface. Due to the expected flexibility of filaments, helical segments were processed as single particles, and at no point was helical symmetry applied during image processing. After template-based autopicking of each complete dataset, picked particles were boxed and extracted from micrographs, and subjected to hierarchical 2D classification to select the best-resolved classes. These selected particles were then auto-refined in 3D as a single class with D4 symmetry applied.

To improve resolution, partial signal subtraction was performed at this stage using a mask that left only the central eight catalytic domains of the filament assembly interface, and then subtracting the poorly resolved Bateman domains and neighboring segments, which often improved resolution after subsequent auto-refinement. Per-particle defocus and per-micrograph astigmatism were then optimized using CTF refinement followed by particle polishing, which generally improved resolution further (Table 2.1).

5.6 Model building and refinement

Initial templates for model building were prepared from hIMPDH2 extended (PDB 6u8N) and compressed octamers (PDB 6u9o) with amino acid mutations to hIMPDH1 sequence made in Coot[112]. Where the N terminus (−22–12) location differed from IMPDH2, it was modeled by hand.

After rigid-body fitting of templates into the cryo-EM densities using UCSF Chimera, repeated cycles of manual fitting with Coot, semiautomated or manual fitting with ISOLDE[113], and automated fitting with phenix.real_space_refine (using rigid-body refinement, NCS constraints, gradient-driven minimization and simulated annealing)[112,114,115]. Data collection parameters and refinement statistics are summarized in Table 2.1. Figures were prepared with UCSF Chimera[114].

The sizes of interacting surfaces between IMPDH protomers were calculated using the PDB ePISA server[116].

5.7 Cell culture and transfection

HEK293 cells were grown in DMEM/10% fetal bovine serum (FBS)/1% L-glutamine on six-well dishes with coverslips in each dish to 50% confluency. They were transfected with 40 µl of Lipofectamine L-2000 (ThermoFisher catalog no. 11668030) and 16 µg of pcDNA3.1 plasmid with either IMPDH1-WT or IMPDH1-Y12A for 6 h and then the media was changed to either new DMEM/10%FBS/1% L-glutamine or DMEM/10%FBS/1% L-glutamine with 10 µM MPA. Twenty-four hours later, the cells were fixed with 4% formaldehyde/PBS for 20 min and immunofluorescence was performed on the coverslips.

5.8 Immunofluorescence

The coverslips with the transfected HEK293 cells were blocked with 2% bovine serum albumin (BSA)/PBS and stained with anti-myc antibody 9e10 DSHB (deposited in the Developmental Studies Hybridoma Bank by J.M. Bishop) diluted 1:50 in 2% BSA/PBS for 1 h at room temperature. Then, cells were incubated with Alexa 488 secondary goat anti-mouse (Invitrogen catalog no. A-11001) diluted 1:200 in 2%BSA/PBS for 30 min at room temperature. Finally, nuclei were stained with 4,6-diamidino-2-phenylindole (DAPI) for 10 min at room temperature and coverslips were mounted with Vectashield mounting medium (Vector Laboratories). The cells were imaged on a Nikon Eclipse TE2000-U with a x40 Nikon plan fluorescence objective and pictures were taken with Ocular QImaging software v.1.1 using a QImaging Retiga R1 CCD camera.

5.9 Zebrafish maintenance and retina collection

Zebrafish were maintained and used in accordance with the guidelines of experimental protocols approved by the IACUC of the University of Washington in Seattle (protocol number: 3113-02). The strains used were AB, AB/roy^{a9} [117], the transgenic strain *Tg(gnat2:EGFP)*[103] and *IMPDH1a*sa23234, which was obtained from the Zebrafish International Research Center. For experiments with *IMPDH1asa23234*, controls were sibling WT fish. *IMPDH1asa23234* fish were identified by genotyping (Table 3.1). Coneless and rodless strains were *Tg(gnat2:mcu-2A-RFP)*w248Tg[86] and *rho*fl9[87], respectively. To ensure that all cones had degenerated *Tg(gnat2:mcu-2A-RFP)*w248Tg, fish were between 12 and 18 months old. Males and females were used in equal numbers for all experiments, and no differences due to sex were noted. Fish ages were between 4 and 12 months old unless stated otherwise.

Fish were maintained in the University of Washington ISCRM aquatics facility at 27.5°C on a 14-h/10-h light/dark cycle, with broad-spectrum white light and daily feedings around 10 AM, 12 PM, and 5 PM 18 to 24 h before experimental timepoints, the fish siblings were fasted to minimize effects of feeding on IMPDH distribution and nucleotide metabolism. The fish were euthanized in an ice bath after cervical dislocation and enucleation; for dark timepoints, euthanasia and dissections were performed under infrared light.

5.10 Immunohistochemistry

Eyes from transgenic adult zebrafish in the AB or AB/roy^{a9} background were placed into fixative (4% paraformaldehyde in PBS, pH 7.3) at room temperature (RT), pierced across the cornea with a needle, and the vitreous cavity was flushed with fixative. After incubation for 1 to 2 h at RT, the eyes were stored for up to 48 h at 4°C, rinsed in PBS, and then cryoprotected in a 20% sucrose gradient overnight. For experiments measuring rod photoreceptors, the eyes were bleached with 10% H_2O_2 in PBS overnight at 37°C before sucrose gradient to remove pigmentation of the retinal pigment epithelium. The following day, the anterior halves of the eye were dissected away, and eyecups were embedded and frozen in OCT cryomolds. The eyecups were cryosectioned at 14 µm; for time point analyses, the sections from all animals were arranged on slides for parallel staining and analysis. The sections were washed in PBS, then blocked for 30 min in blocking buffer (2% normal donkey serum, 2 mg/ml bovine serum albumin, and 0.3% Triton X-100 in PBS). Primary antibodies diluted in the blocking buffer were then applied to cryosections overnight at 4 °C. The antibodies and stains are reported in Table 3.2. Secondary antibodies conjugated to AlexaFluor dyes were diluted at 1:2000 in blocking buffer and incubated on sections for 1 h in darkness at RT.

5.11 IHC imaging and analysis

Imaging was performed on a Leica SP8 confocal microscope with a 20x or 63x oil objective and 12 bit depth using Leica LAS-X software (RRID:SCR_013673). For quantitative imaging with the 63× objective, Z-stack images of photoreceptor regions 100 to 200 µm from the optic nerve were acquired every 0.3 µm at 5000 × 625 pixel resolution for synapses and 4096 × 2048 pixel resolution for inner segments. The Z-stacks from each animal and region were blindly analyzed using Image J software (RRID:SCR_002285). For all, the cone and rod IMPDH1a signals were isolated by creating masks with either cone *Tg(gnat2:eGFP)* (RRID:ZDB-GENO-070829-1,[117]) or the rod marker 4C12 (ZDB-ATB-090506-2). Three technical replicates of staining and imaging were performed for each animal. Representative images were post processed with Leica Lightning deconvolution; brightness and contrast were adjusted equally to ease visualization.

5.12 Antibodies

The company Pacific Immunology (https://www.pacificimmunology.com) generated polyclonal antibodies in rabbits from the following N and C terminal sequences (N terminus ERYVDGDREGYQIDYRRIVGD-Cys and C terminus Cys-TRNGYIEPGSRGHPRAGPNVPSPAVTKHSS). The antibodies were provided affinity purified. Western blots were conducted, as previously described [118]. After Western blot transfer, the membranes were stained with Ponceau S (Sigma #P7170), washed with water, and imaged as a loading control.

5.13 Metabolomics

Fish were fasted for 18 to 24 h. The retinas were rapidly dissected from eyes, rinsed in Krebs–Ringer bicarbonate buffer (98.5 mM NaCl, 4.9 mM KCl, 1.2 mM KH_2PO_4, 1.2 mM $MGSO_4$–$7H_2O$, 20 mM Hepes, 2.6 mM CaCl–$2H_2O$, and 25.9 mM $NaHCO_3$) and then immediately frozen. The retina samples were homogenized in 140 µl cold 80% methanol (methanol:water (80:20 V/V)) using a microtube homogenizer. The samples were stored on dry ice for 30 min, then centrifuged at 15,000 RPM for 15 min. The supernatant was dried by the gel pump (Savant), and then the dried extract was reconstituted with 100 µl of mobile phase (a mixture of A:B at 30:70 in V/V) for targeted metabolomics, as reported [119,120]. The metabolite extracts were analyzed by a Shimadzu LC Nexera X2 UHPLC coupled with a QTRAP 5500 LC-MS/MS (AB Sciex). An ACQUITY UPLC BEH Amide analytic column (2.1 × 50 mm, 1.7 µm) (Waters Corp) was used for chromatographic separation. The mobile phase was (A) water with 10 mM ammonium acetate (pH 8.9) and (B) acetonitrile/water (95/5) with 10 mM ammonium acetate (pH 8.2) (All solvents were LC–MS Optima grade from Fisher Scientific). The total run time was 11 min with a flow rate of 0.5 ml/min and an injection volume of 5 µl. The gradient elution was 95 to 61% B in 6 min, 61 to 44% B at 8 min, 61 to 27% B at 8.2 min, and 27 to 95% B at 9 min. The column was equilibrated with 95% B at the end of each run. The source and collision gas was N2. The ion source conditions in positive and negative mode were as follows: curtain gas (CUR) = 25 psi, collision gas (CAD) = high, ion spray voltage (IS) = 3800/−3800 V, temperature (TEM) = 500 °C, ion source gas 1 (GS1) = 50 psi, and ion source gas 2 (GS2) = 40 psi. Each metabolite was tuned with standards for optimal transitions. D4-nicotinamide (Cambridge Isotope Laboratories) was used as an internal standard. The extracted MRM peaks were integrated using MultiQuant 3.0.3 software (AB Sciex).

5.14 qRT-PCR and identification of transcripts

Extraction of RNA, cDNA synthesis, and qRT-PCR amplification were conducted, as previously described using TATA-box binding protein as a reference gene [86,121]. The primers are listed in Table 3.1. For *IMPDH1b* amplification, primer set 1 was used for Figures 3.1A,B and 3.55C, and primer set 2 was used for Figures 3.3F,G and 3.55C. Mitochondrial DNA quantification was performed, as described[122].

5.15 Zebrafish models

For generation of the Tg(*TαCP*:*IMPDH1a_tvX1*-mutant) line, plasmids were assembled using the Gateway-Tol2 system[123]. Expression of Impdh1a_tvX1 was driven by the cone transducin alpha promoter (TαCP, gnat2)[103]. A destination vector with a RFP heart marker for aid in transgenic identification was used. The fully assembled construct was injected into embryos at the 1-cell stage with Tol2 transposase mRNA. Larvae mosaic for the transgene were raised to adulthood to identify founder carriers. A single *F*0 founder was used to generate *F*1 fish that were screened for a single insertion of the transgene; *F*2 fish from two *F*1 substrains with a single insertion were used for analysis in this study.

5.16 Immunoblotting

Samples were loaded into wells on 10% acrylamide gel (BioRad, 4561033 or 4561036). After running the gel at 200 V for 35 min, gels were transferred onto PVDF membranes (Millipore, IPFL00010) and blocked for 1 h at room temperature in LI-COR Odyssey Blocking Buffer (LI-COR, 927–40,000). Primary antibodies were diluted in blocking buffer at specified concentrations and incubated overnight at 4°C. Membranes were washed with PBST, then incubated with secondary antibody for 1 h at 25°C and washed again with PBST before imaging. Membranes were imaged and bands were quantified using the LI-COR Odyssey CLx Imaging System (RRID:SCR_014579). Gels were repeated a minimum of twice, with images from one representative experiment.

Supplemental

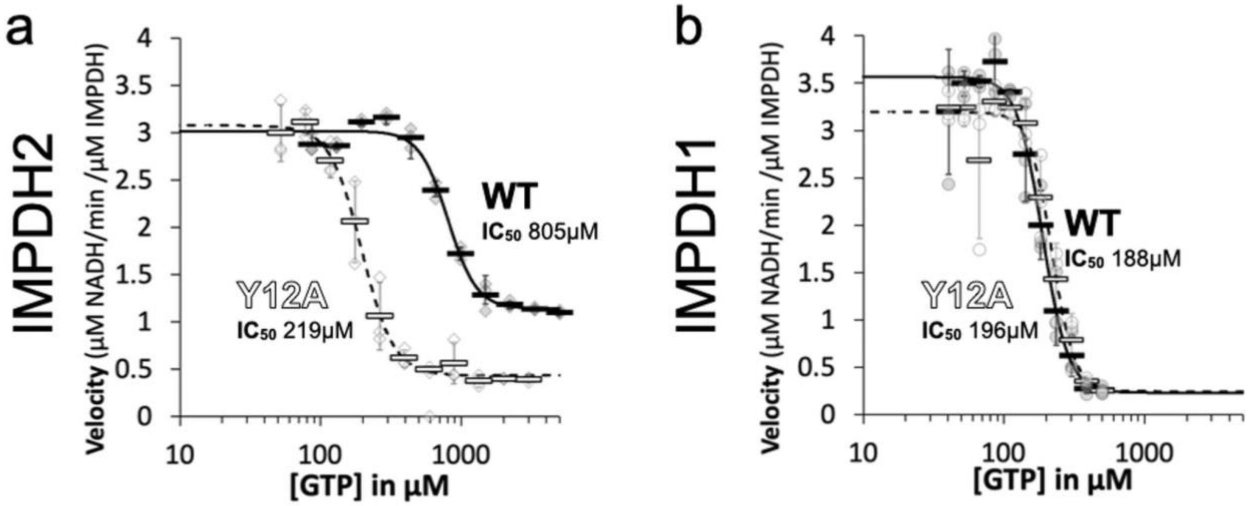

Supplemental Figure 2.1: IMPDH2-WT Filaments Resist GTP Inhibition
a,b, GTP inhibition curves of IMPDH2 or IMPDH1-WT (solid line) and the respective non-assembly Y12A protein (dashed line). Individual data points are shown as diamonds (IMPDH2) or circles (IMPDH1), where filled are WT and empty Y12A. Reactions were performed in triplicate and the average for each concentration is shown as a bold rectangle (filled is WT, empty is Y12A). Error bars are standard deviation calculated from n = 3. Reactions performed with 1 µM protein, 1 mM ATP, 1 mM IMP, 300 µM NAD^+, and varying GTP.

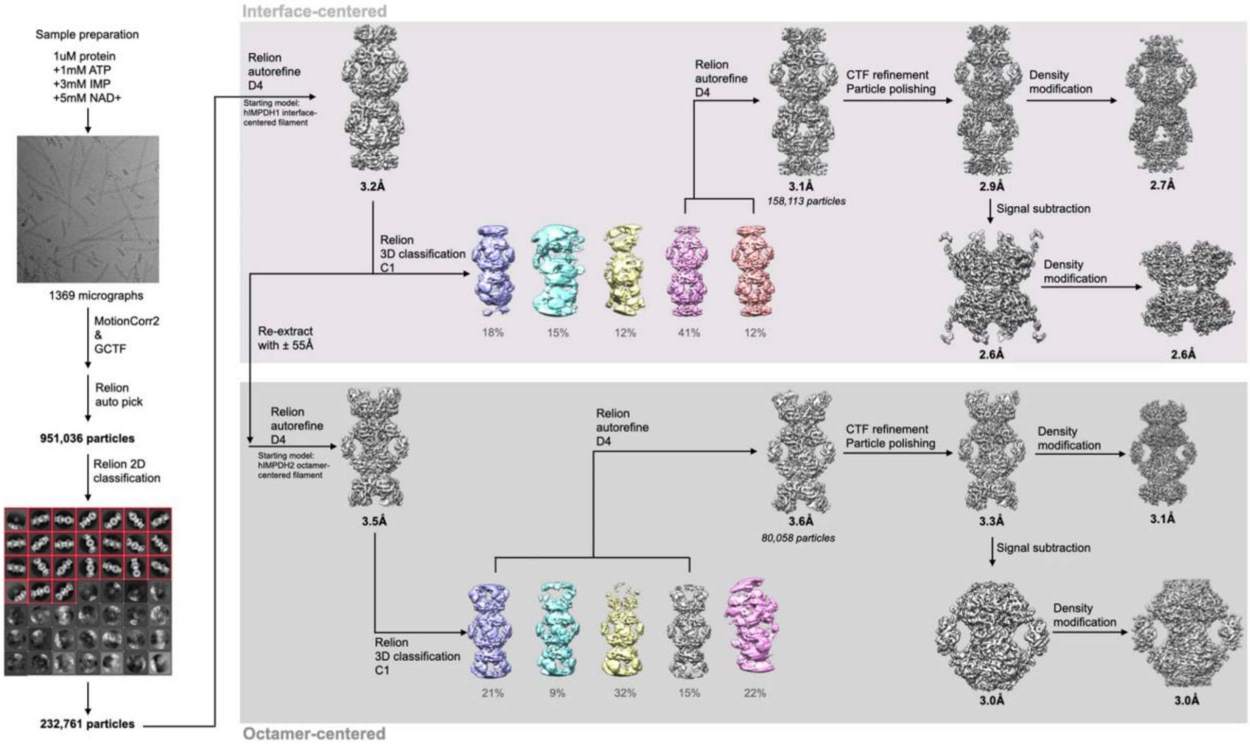

Supplemental Figure 2.2: Cryo-EM workflow
Flow chart summarizing data processing strategy for IMPDH1+ ATP/IMP/NAD$^+$.

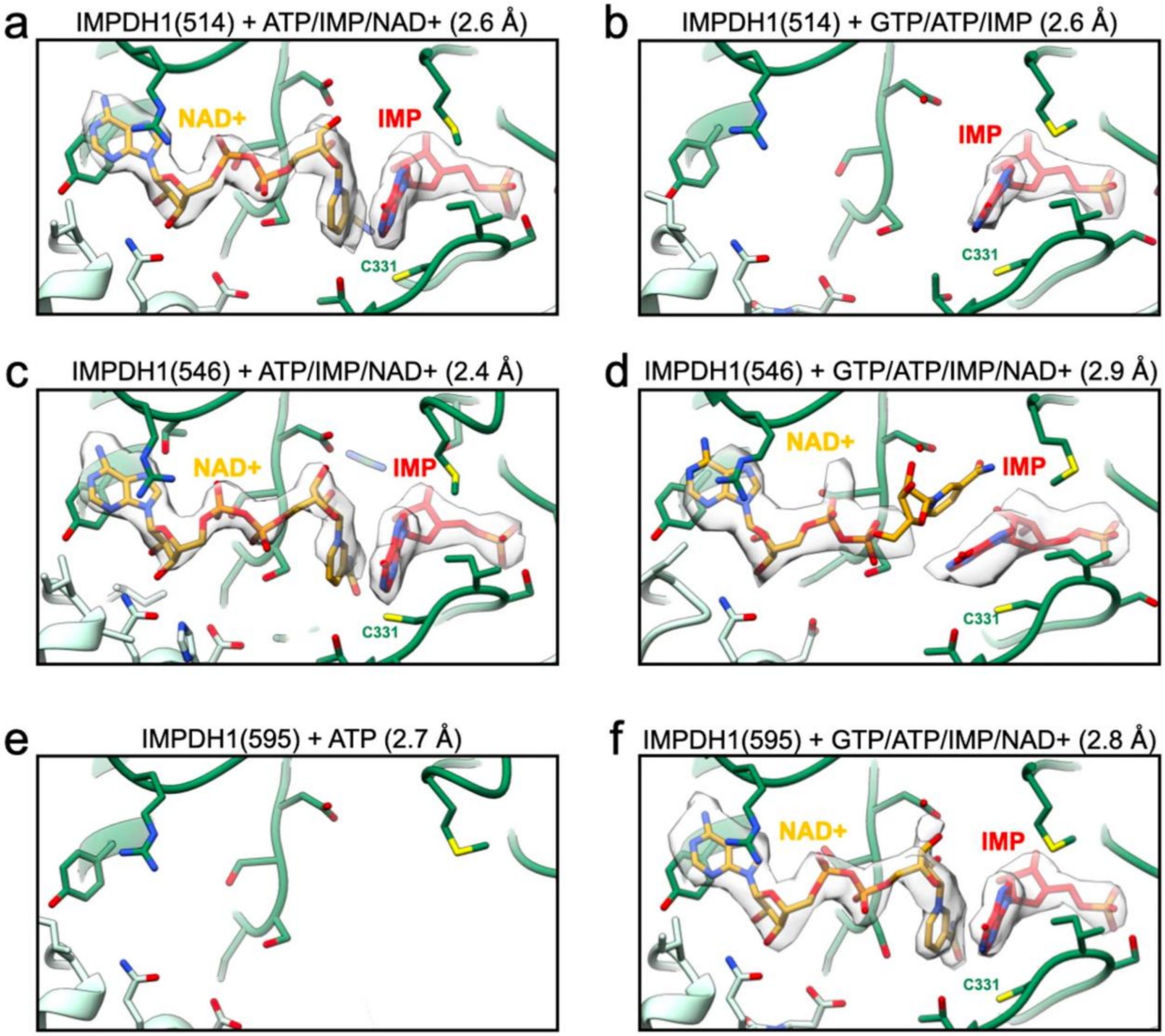

Supplemental Figure 2.3: IMPDH1 active site map and model
a-f, Cartoon representation of the active site. Side chains around the active site are shown as sticks. Chain A is dark green while the neighboring chain is light green. NAD^+ is yellow and IMP red. Density for the ligand(s) is shown as a surface. a, IMPDH1(514) bound to ATP/IMP/NAD^+. **b**, IMPDH1(514) bound to GTP/ATP/IMP. **c**, IMPDH1(546) bound to ATP/IMP/NAD^+. **d**, IMPDH1(546) bound to GTP/ATP/IMP/NAD^+. **e**, IMPDH1(595) bound to ATP. **f**, IMPDH1(595) bound to GTP/ATP/IMP/NAD^+.

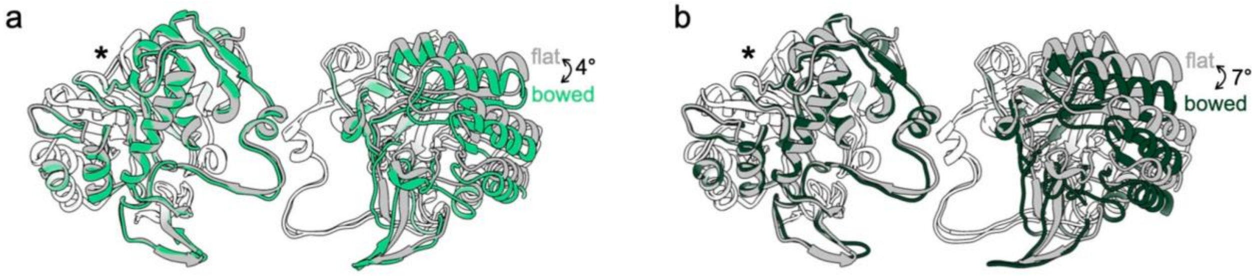

inhibited IMPDH2 (filament) vs inhibited IMPDH2 (free octamer)

inhibited IMPDH2 (filament) vs inhibited IMPDH1

Supplemental Figure 2.4: Inhibited IMPDH1-WT tetramer is in a bowed conformation

a, Comparison of the catalytic tetramers of inhibited IMPDH2 filament (gray; 6u8s) to inhibited IMPDH2 free octamer (6uaj). Aligned on monomers with asterisk, other monomer pair has an alpha carbon RMSD of 2.1 Å. **b**, Comparison of the catalytic tetramers of inhibited IMPDH2 filament (gray; 6u8s) to inhibited IMPDH1 filament. Aligned on monomers with asterisk, other monomer pair has an alpha carbon RMSD of 3.7 Å.

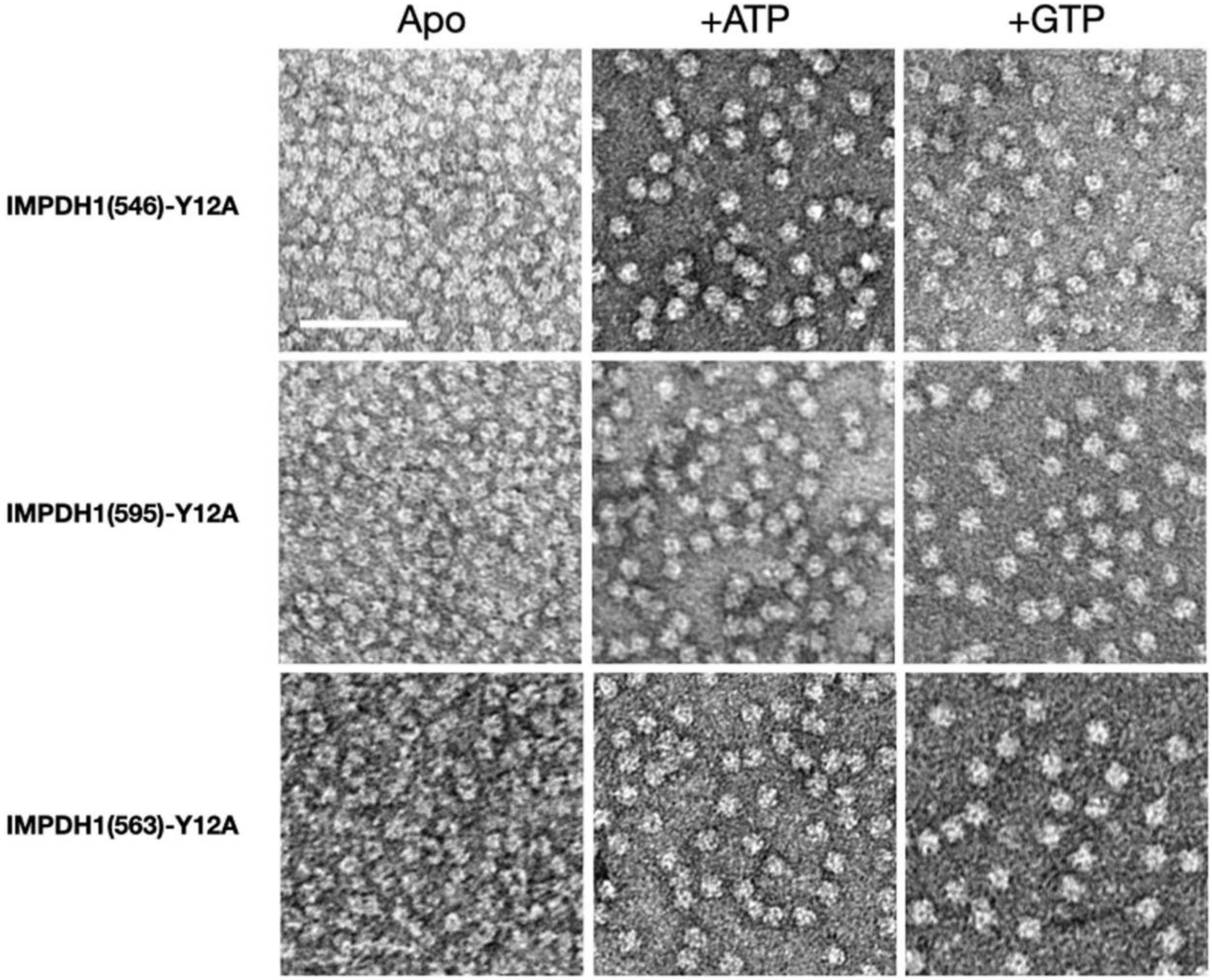

Supplemental Figure 2.5: Y12A non-assembly mutation prevents assembly in all IMPDH1 variants

Negative stain EM of purified human IMPDH1. Non-assembly mutation Y12A breaks both ATP- and GTP-dependent assembly. Scale bar 100 nm. Reactions performed with 1 µM protein, 1 mM ATP if used, 1 mM GTP if used.

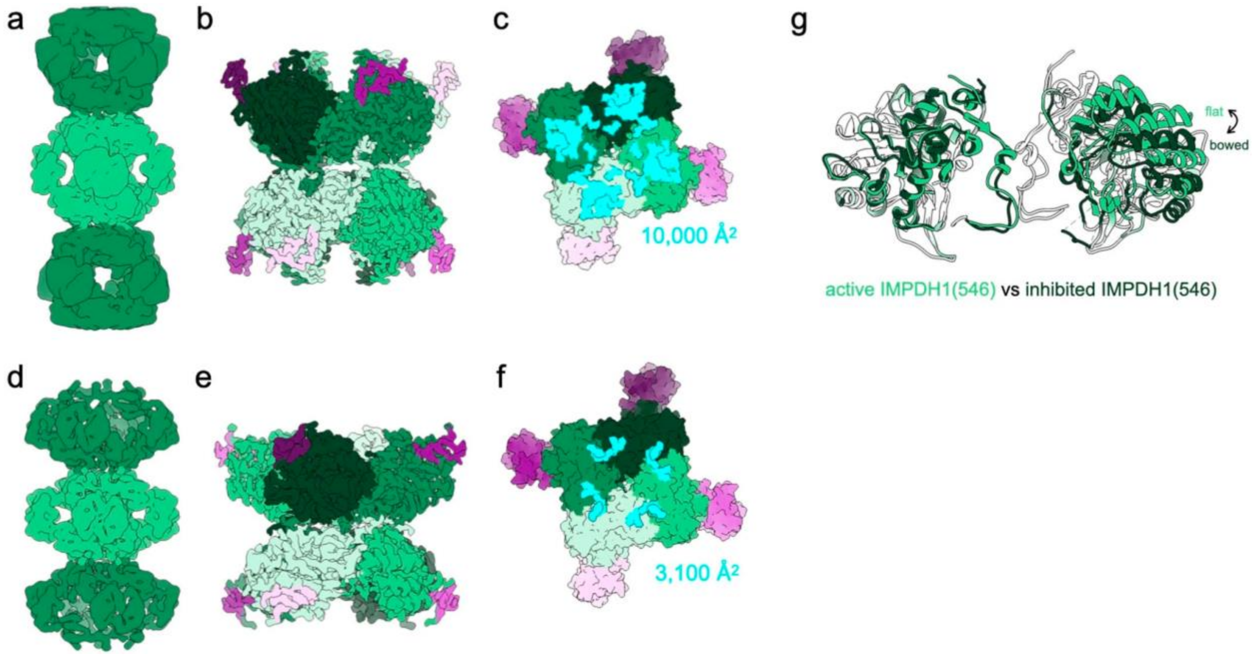

Supplemental Figure 2.6: IMPDH1 retinal variant (546) is similar to canonical IMPDH1
a-c, Active IMPDH1(546) filament bound to ATP, IMP, NAD$^+$. **a**, Low-pass filtered cryo-EM reconstruction **b**, Interface-focused cryo-EM reconstruction. 8 monomers are colored by catalytic domain (green) and regulatory domain (pink). **c**, View of the top of an octamer from inside the filament. The surface area buried by the octamer interface is in aqua with the indicated total buried surface area. (Surface representation of the atomic model at the assembly interface, with buried residues in cyan). d-f, Inhibited IMPDH1(546) filament bound to GTP, ATP, IMP, NAD$^+$. **d**, Low-pass filtered cryo-EM reconstruction **e**, Interface-focused cryo-EM reconstruction. 8 monomers are colored by catalytic domain (green) and regulatory domain (pink). f, View of the top of an octamer from inside the filament. The surface area buried by the octamer interface is in aqua with the indicated total buried surface area. (Surface representation of the atomic model at the assembly interface, with buried residues in cyan).

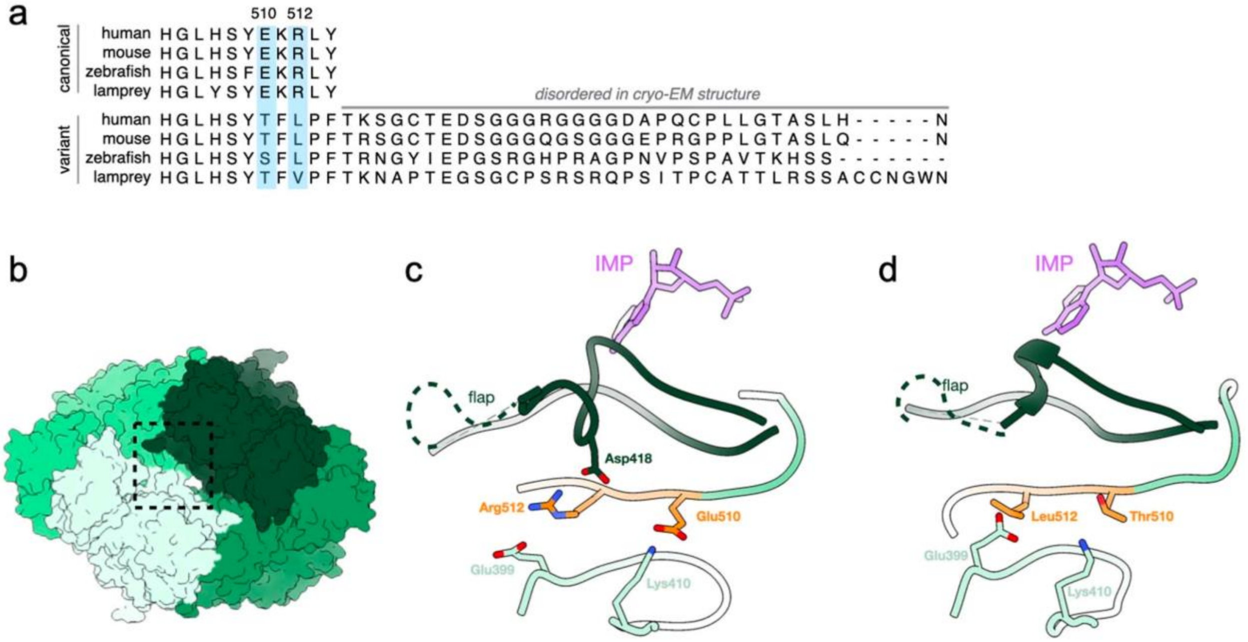

Supplemental Figure 2.7: IMPDH1 retinal variant C-term disrupts interactions
a, Evolutionary conservation of the C-terminus in canonical IMPDH1 and both retinal splice variants. **b**, Surface representation of octamer side view. Dotted box indicates the region shown in **c-d**. **c-d**, Each chain is a different color green, C-term residues 510–512 in orange, and IMP in purple. c, inhibited canonical IMPDH1. **d**, Inhibited retinal variant IMPDH1(546).

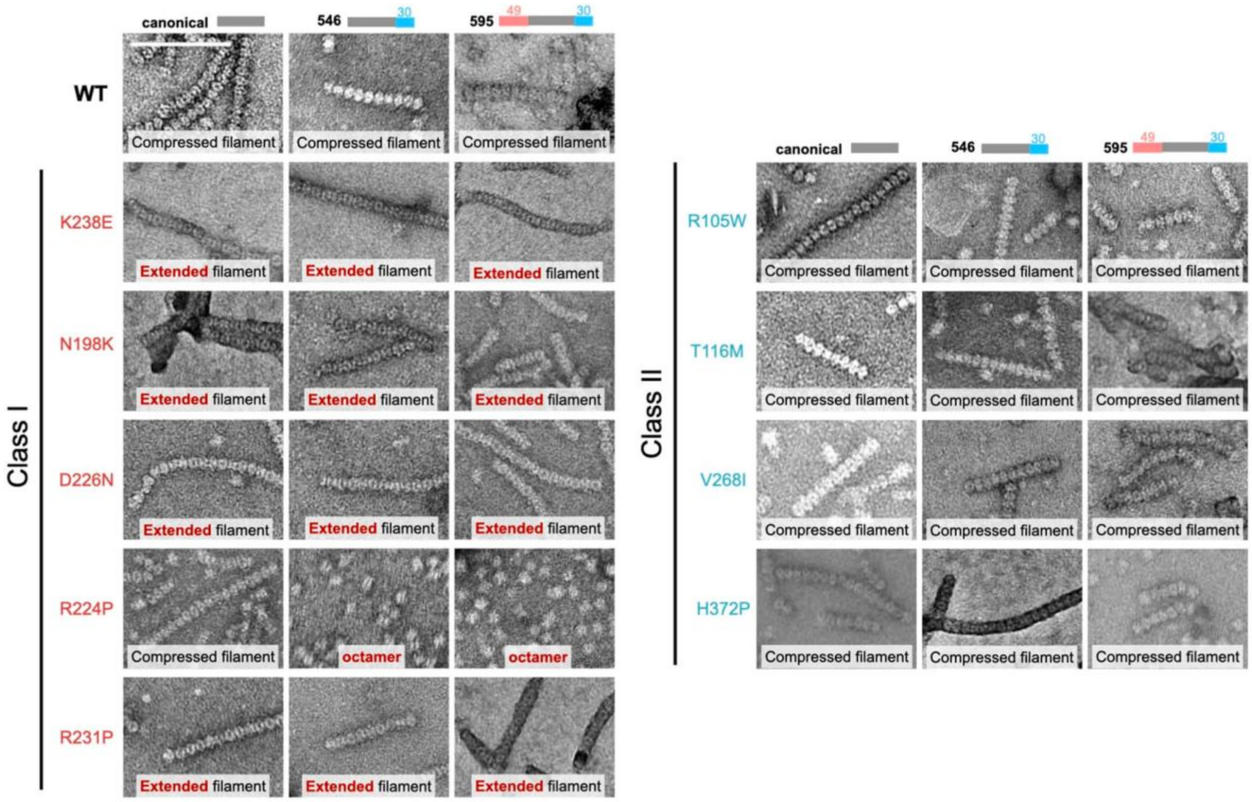

Supplemental Figure 4.1: IMPDH1 disease mutants have a variety of assembly phenotypes
Negative stain EM of purified human IMPDH1. Scale bar 100 nm. Reactions performed with 1 μM protein, 1 mM ATP, 5 mM GTP, 3 mM IMP, 5 mM NAD$^+$.

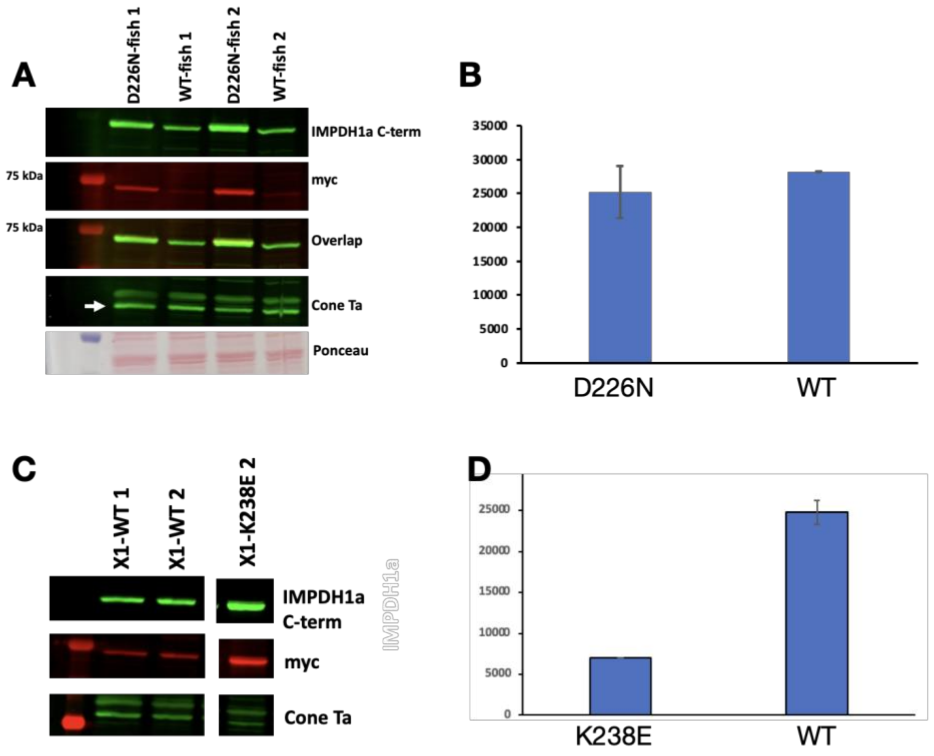

Supplemental Figure 5.1: Cone degeneration depends on RP mutation
A, Representative western blot with transgenic zebrafish expressing TaCP:Impdh1a_tvX1-D226N and WT siblings probing for Impdh1a, myc, and cone transducin (Table 3.2) **B**, Quantification of western blots show no change in transducin levels **C,** Representative western blot with transgenic zebrafish expressing TaCP:Impdh1a_tvX1-K238E and WT siblings probing for Impdh1a, myc, and cone transducin (Table 3.2) **D**, Quantification of western blots show decrease in cone transducin in transgenic fish

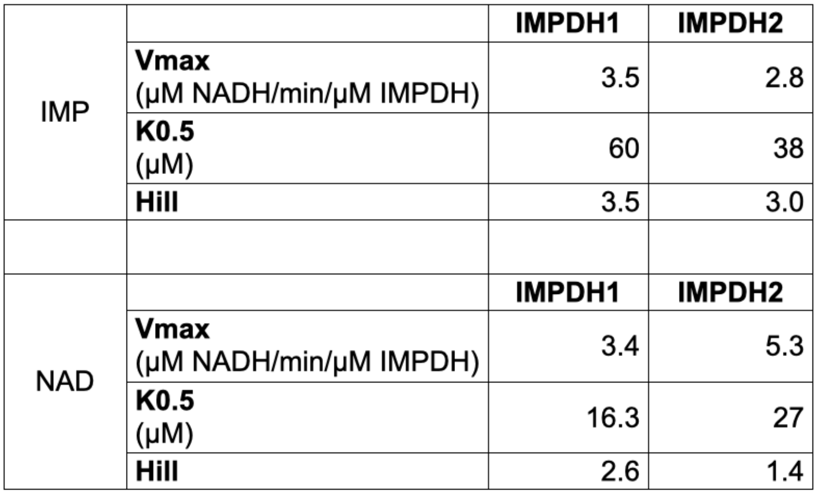

		IMPDH1	**IMPDH2**
IMP	**Vmax** (µM NADH/min/µM IMPDH)	3.5	2.8
	K0.5 (µM)	60	38
	Hill	3.5	3.0
NAD		**IMPDH1**	**IMPDH2**
	Vmax (µM NADH/min/µM IMPDH)	3.4	5.3
	K0.5 (µM)	16.3	27
	Hill	2.6	1.4

Supplemental Table 2.1 IMPDH1 and IMPDH2 have similar kinetics
Table comparing Vmax, K0.5, and Hill coefficients for IMP and NAD^+ for IMPDH1 and IMPDH2. Reactions performed with 1 µM protein, 1 mM ATP, 1 mM or varying IMP, and 300 µM or varying NAD^+. All data points reported are an average of 3 measurements from the same protein preparation. Fits for activity assays were calculated using the Hill-Langmuir equation V = Vmax*[S] [105]

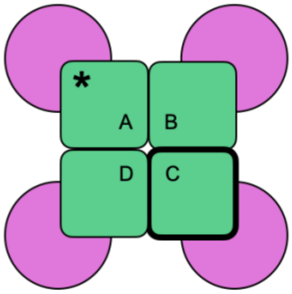

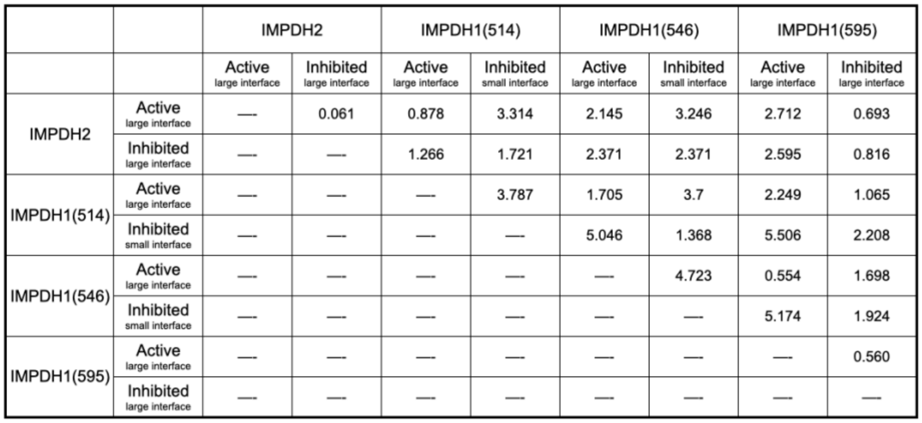

		IMPDH2		IMPDH1(514)		IMPDH1(546)		IMPDH1(595)	
		Active large interface	Inhibited large interface	Active large interface	Inhibited small interface	Active large interface	Inhibited small interface	Active large interface	Inhibited large interface
IMPDH2	Active large interface	—	0.061	0.878	3.314	2.145	3.246	2.712	0.693
	Inhibited large interface	—	—	1.266	1.721	2.371	2.371	2.595	0.816
IMPDH1(514)	Active large interface	—	—	—	3.787	1.705	3.7	2.249	1.065
	Inhibited small interface	—	—	—	—	5.046	1.368	5.506	2.208
IMPDH1(546)	Active large interface	—	—	—	—	—	4.723	0.554	1.698
	Inhibited small interface	—	—	—	—	—	—	5.174	1.924
IMPDH1(595)	Active large interface	—	—	—	—	—	—	—	0.560
	Inhibited large interface	—	—	—	—	—	—	—	—

Supplemental Table 2.2 RMSD between catalytic domains of models

Top-down view of tetramer with catalytic domains (green) and regulatory domains (pink). Models are aligned on catalytic domain with asterisk and alpha carbon RMSD is calculated by catalytic domain outlined in bold. IMPDH2 active is 6u8n, IMPDH2 inactive is 6u8s RMSD to determine how tetramer flexing (bent/flat) compares.

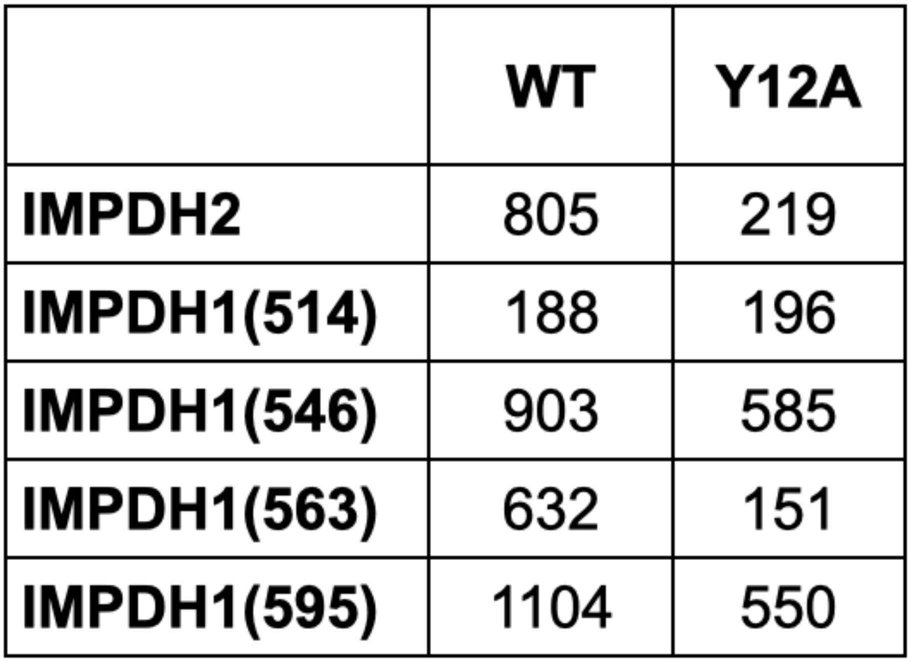

	WT	Y12A
IMPDH2	805	219
IMPDH1(514)	188	196
IMPDH1(546)	903	585
IMPDH1(563)	632	151
IMPDH1(595)	1104	550

Supplemental Table 2.3 IMPDH1 and IMPDH2 IC$_{50}$ for GTP in µM

a

		WT	R105W	T116M	N198K	R224P	D226N	R231P	K238E	V268I	H372P
514	Vmax	3.4	3.7	3.4	3.4	3.2	3.4	4.2	5.3	4.6	4.4
	K0.5	16.3	15.5	9.3	10.8	9.9	8.8	12.9	20.7	16.9	16.2
	Hill	2.6	3.1	1.7	3.2	1.9	1.7	2.1	2.7	2.4	3.2
546		WT	R105W	T116M	N198K	R224P	D226N	R231P	K238E	V268I	H372P
	Vmax	5.5	5.3	4.2	5.1	6.4	5.1	5.8	5.4	6.0	8.8
	K0.5	32.9	22.8	19.5	31.0	31.5	26.2	31.9	22.5	24.9	46.9
	Hill	1.9	1.1	1.3	1.0	1.0	1.1	0.9	1.0	0.9	1.1
595		WT	R105W	T116M	N198K	R224P	D226N	R231P	K238E	V268I	H372P
	Vmax	5.2	5.3	4.0	4.8	1.5	5.5	6.8	26.9	5.1	7.4
	Km	30.4	32.6	28.8	36.7	28.1	23.1	39.6	1.6	36.7	66.2
	Hill	1.2	1.0	1.1	0.6	0.7	0.9	1.1	0.9	1.3	1.3

b

		WT	R105W	T116M	N198K	R224P	D226N	R231P	K238E	V268I	H372P
514	Vmax	3.5	4.2	2.5	3.0	3.1	2.6	3.5	5.0	3.3	3.5
	K0.5	59.5	13.6	28.0	19.9	12.3	10.0	20.2	17.9	25.4	25.0
	Hill	3.5	2.7	2.7	2.1	2.0	1.9	2.2	2.0	2.5	3.0
546		WT	R105W	T116M	N198K	R224P	D226N	R231P	K238E	V268I	H372P
	Vmax	4.8	5.3	4.7	4.7	4.5	4.6	4.5	4.5	4.8	6.1
	K0.5	33.0	23.3	34.4	34.4	27.6	22.6	17.9	26.8	39.2	45.1
	Hill	1.3	1.0	0.8	0.8	1.3	1.1	1.2	1.5	1.4	1.3
595		WT	R105W	T116M	N198K	R224P	D226N	R231P	K238E	V268I	H372P
	Vmax	5.2	4.9	3.6	3.7	5.0	4.6	6.0	6.2	5.0	7.1
	K0.5	27.9	20.4	23.4	18.9	22.3	22.6	26.0	35.8	20.3	28.6
	Hill	1.4	1.5	1.6	1.2	1.1	1.1	1.3	1.5	1.3	1.5

c

		WT	R105W	T116M	N198K	R224P	D226N	R231P	K238E	V268I	H372P
514	Vmax	3.6	4.1	2.7	3.0	2.8	2.2	3.2	4.5	3.1	3.3
	K0.5	187.8	15.9	132.4	N/A	N/A	134.0	N/A	N/A	150.8	151.2
	Hill	4.7	25.2	3.0	N/A	N/A	32.1	N/A	N/A	5.7	2.6
546		WT	R105W	T116M	N198K	R224P	D226N	R231P	K238E	V268I	H372P
	Vmax	4.4	4.8	4.4	3.9	5.2	4.5	3.9	4.5	5.3	7.3
	K0.5	903.4	759.6	888.3	N/A	N/A	N/A	N/A	N/A	870.9	630.8
	Hill	5.3	2.7	3.8	N/A	N/A	N/A	N/A	N/A	3.2	5.4
595		WT	R105W	T116M	N198K	R224P	D226N	R231P	K238E	V268I	H372P
	Vmax	4.5	4.9	4.1	3.6	4.9	4.5	5.0	6.0	5.2	7.4
	K0.5	1104.0	1274.4	1760.5	N/A	N/A	N/A	N/A	N/A	1313.9	1843.0
	Hill	3.9	2.4	3.5	N/A	N/A	N/A	N/A	N/A	2.4	1.8

Supplemental Table 4.1. IMPDH1 RP mutations do not change NAD^+ or IMP kinetics in any variants

a-c, V_{max} (µM NADH/min/µM IMPDH), K0.5 (µM), and Hill coefficient for NAD^+ for WT and RP mutants in all variants. **a**, For NAD^+. Reactions performed with 1 µM protein, 1 mM ATP, 1 mM IMP, and varying NAD^+. **b**, For IMP. Reactions performed with 1 µM protein, 1 mM ATP, 300 µM NAD^+, and varying IMP. **c**, For GTP. Reactions performed with 1 µM protein, 1 mM ATP, 1 mM IMP, 300 µM NAD^+, and varying GTP. All data points reported are an average of 3 measurements from the same protein preparation. Fits for activity assays were calculated using the HillLangmuir equation $V = V_{max}*[S]n/((K0.5)n+[S]n)$ and IC_{50} was calculated using a modified Hill equation $V=V_{min}*(V_{max}-V_{min})/(1+(I/IC_{50})hill$ [105]**.**

References

1. Chitrakar, I., Kim-Holzapfel, D. M., Zhou, W. & French, J. B. Higher order structures in purine and pyrimidine metabolism. *J. Struct. Biol.* **197**, 354–364 (2017).
2. Jin, M. *et al.* Glycolytic Enzymes Coalesce in G Bodies under Hypoxic Stress. *Cell Rep.* **20**, 895–908 (2017).
3. Park, C. K. & Horton, N. C. Structures, functions, and mechanisms of filament forming enzymes: a renaissance of enzyme filamentation. *Biophys. Rev.* **11**, 927–994 (2019).
4. Lynch, E. M., Kollman, J. M. & Webb, B. A. Filament formation by metabolic enzymes—A new twist on regulation. *Curr. Opin. Cell Biol.* **66**, 28–33 (2020).
5. Garcia-Seisdedos, H., Empereur-Mot, C., Elad, N. & Levy, E. D. Proteins evolve on the edge of supramolecular self-assembly. *Nature* vol. 548 244–247 (2017).
6. Garcia Seisdedos, H., Levin, T., Shapira, G., Freud, S. & Levy, E. D. Mutant libraries reveal negative design shielding proteins from supramolecular self-assembly and relocalization in cells. *Proc. Natl. Acad. Sci. U. S. A.* **119**, (2022).
7. Noree, C., Sato, B. K., Broyer, R. M. & Wilhelm, J. E. Identification of novel filament-forming proteins in Saccharomyces cerevisiae and Drosophila melanogaster. *J. Cell Biol.* **190**, 541–551 (2010).
8. O'Connell, J. D. *et al.* A proteomic survey of widespread protein aggregation in yeast. *Mol. Biosyst.* **10**, 851–861 (2014).
9. Shen, Q.-J. *et al.* Filamentation of Metabolic Enzymes in Saccharomyces cerevisiae. *J. Genet. Genomics* **43**, 393–404 (2016).
10. Noree, C. *et al.* A quantitative screen for metabolic enzyme structures reveals patterns of assembly across the yeast metabolic network. *Mol. Biol. Cell* **30**, 2721–2736 (2019).
11. Hedstrom, L. IMP dehydrogenase: structure, mechanism, and inhibition. *Chem. Rev.* **109**, 2903–2928 (2009).
12. Buey, R. M. *et al.* Guanine nucleotide binding to the Bateman domain mediates the

allosteric inhibition of eukaryotic IMP dehydrogenases. *Nat. Commun.* **6**, 8923 (2015).

13. Anthony, S. A. *et al.* Reconstituted IMPDH polymers accommodate both catalytically active and inactive conformations. *Mol. Biol. Cell* (2017) doi:10.1091/mbc.E17-04-0263.
14. Fernández-Justel, D. *et al.* A Nucleotide-Dependent Conformational Switch Controls the Polymerization of Human IMP Dehydrogenases to Modulate their Catalytic Activity. *J. Mol. Biol.* **431**, 956–969 (2019).
15. Johnson, M. C. & Kollman, J. M. Cryo-EM structures demonstrate human IMPDH2 filament assembly tunes allosteric regulation. *Elife* **9**, (2020).
16. Burrell, A. L. *et al.* IMPDH1 retinal variants control filament architecture to tune allosteric regulation. *Nat. Struct.* (2022) doi:10.1038/s41594-021-00706-2.
17. Jackson, R. C., Weber, G. & Morris, H. P. IMP dehydrogenase, an enzyme linked with proliferation and malignancy. *Nature* **256**, 331–333 (1975).
18. Carr, S. F., Papp, E., Wu, J. C. & Natsumeda, Y. Characterization of human type I and type II IMP dehydrogenases. *J. Biol. Chem.* **268**, 27286–27290 (1993).
19. Senda, M. & Natsumeda, Y. Tissue-differential expression of two distinct genes for human IMP dehydrogenase (E.C.1.1.1.205). *Life Sci.* **54**, 1917–1926 (1994).
20. Jain, J. *et al.* Regulation of inosine monophosphate dehydrogenase type I and type II isoforms in human lymphocytes. *Biochem. Pharmacol.* **67**, 767–776 (2004).
21. Bowne, S. J. *et al.* Why do mutations in the ubiquitously expressed housekeeping gene IMPDH1 cause retina-specific photoreceptor degeneration? *Invest. Ophthalmol. Vis. Sci.* **47**, 3754–3765 (2006).
22. Zhang, R. *et al.* Characteristics and crystal structure of bacterial inosine-5'-monophosphate dehydrogenase. *Biochemistry* **38**, 4691–4700 (1999).
23. Fernández-Justel, D., Peláez, R., Revuelta, J. L. & Buey, R. M. The Bateman domain of IMP dehydrogenase is a binding target for dinucleoside polyphosphates. *J. Biol. Chem.* **294**, 14768–14775 (2019).

24. Buey, R. M. *et al.* A nucleotide-controlled conformational switch modulates the activity of eukaryotic IMP dehydrogenases. *Sci. Rep.* **7**, 2648 (2017).

25. Ji, Y., Gu, J., Makhov, A. M., Griffith, J. D. & Mitchell, B. S. Regulation of the interaction of inosine monophosphate dehydrogenase with mycophenolic Acid by GTP. *J. Biol. Chem.* **281**, 206–212 (2006).

26. Carcamo, W. C., Calise, S. J., von Mühlen, C. A., Satoh, M. & Chan, E. K. L. Molecular cell biology and immunobiology of mammalian rod/ring structures. *Int. Rev. Cell Mol. Biol.* **308**, 35–74 (2014).

27. Calise, S. J. *et al.* Glutamine deprivation initiates reversible assembly of mammalian rods and rings. *Cell. Mol. Life Sci.* **71**, 2963–2973 (2014).

28. Calise, S. J., Abboud, G., Kasahara, H., Morel, L. & Chan, E. K. L. Immune Response-Dependent Assembly of IMP Dehydrogenase Filaments. *Front. Immunol.* **9**, 2789 (2018).

29. Duong-Ly, K. C. *et al.* T cell activation triggers reversible inosine-5′-monophosphate dehydrogenase assembly. *Journal of Cell Science* (2018) doi:10.1242/jcs.223289.

30. Carcamo, W. C. *et al.* Induction of Cytoplasmic Rods and Rings Structures by Inhibition of the CTP and GTP Synthetic Pathway in Mammalian Cells. *PLoS ONE* vol. 6 e29690 (2011).

31. Thomas, E. C. *et al.* Different characteristics and nucleotide binding properties of inosine monophosphate dehydrogenase (IMPDH) isoforms. *PLoS One* **7**, e51096 (2012).

32. Keppeke, G. D., Andrade, L. E. C., Grieshaber, S. S. & Chan, E. K. L. Microinjection of specific anti-IMPDH2 antibodies induces disassembly of cytoplasmic rods/rings that are primarily stationary and stable structures. *Cell Biosci.* **5**, 1 (2015).

33. Keppeke, G. D., Calise, S. J., Chan, E. K. L. & Andrade, L. E. C. Assembly of IMPDH2-based, CTPS-based, and mixed rod/ring structures is dependent on cell type and conditions of induction. *J. Genet. Genomics* **42**, 287–299 (2015).

34. Chang, C.-C. *et al.* Cytoophidium assembly reflects upregulation of IMPDH activity. *J. Cell*

Sci. **128**, 3550–3555 (2015).

35. Ruan, H. *et al.* IMPDH1/YB-1 Positive Feedback Loop Assembles Cytoophidia and Represents a Therapeutic Target in Metastatic Tumors. *Mol. Ther.* **28**, 1299–1313 (2020).
36. Calise, S. J. & Chan, E. K. L. Anti-rods/rings autoantibody and IMPDH filaments: an update after fifteen years of discovery. *Autoimmun. Rev.* **19**, 102643 (2020).
37. Juda, P., Smigová, J., Kováčik, L., Bártová, E. & Raška, I. Ultrastructure of cytoplasmic and nuclear inosine-5'-monophosphate dehydrogenase 2 'rods and rings' inclusions. *J. Histochem. Cytochem.* **62**, 739–750 (2014).
38. Ahangari, N. *et al.* Nuclear IMPDH Filaments in Human Gliomas. *J. Neuropathol. Exp. Neurol.* (2021) doi:10.1093/jnen/nlab090.
39. Labesse, G. *et al.* MgATP regulates allostery and fiber formation in IMPDHs. *Structure* **21**, 975–985 (2013).
40. Li, T. *et al.* SARS-CoV-2 Nsp14 activates NF-κB signaling and induces IL-8 upregulation. *bioRxiv* (2021) doi:10.1101/2021.05.26.445787.
41. Gordon, D. E. *et al.* A SARS-CoV-2 protein interaction map reveals targets for drug repurposing. *Nature* **583**, 459–468 (2020).
42. Lee, Y. *et al.* ANKRD9 is associated with tumor suppression as a substrate receptor subunit of ubiquitin ligase. *Biochim. Biophys. Acta Mol. Basis Dis.* **1864**, 3145–3153 (2018).
43. Hayward, D. *et al.* ANKRD9 is a metabolically-controlled regulator of IMPDH2 abundance and macro-assembly. *J. Biol. Chem.* **294**, 14454–14466 (2019).
44. Pua, K. H., Stiles, D. T., Sowa, M. E. & Verdine, G. L. IMPDH2 Is an Intracellular Target of the Cyclophilin A and Sanglifehrin A Complex. *Cell Rep.* **18**, 432–442 (2017).
45. Bianchi-Smiraglia, A. *et al.* Regulation of local GTP availability controls RAC1 activity and cell invasion. *Nat. Commun.* **12**, 6091 (2021).
46. Chang, C., Keppeke, G. D., Sung, L. & Liu, J. Interfilament interaction between IMPDH and CTPS cytoophidia. *The FEBS Journal* vol. 285 3753–3768 (2018).

47. Hedstrom, L. IMP dehydrogenase-linked retinitis pigmentosa. *Nucleosides Nucleotides Nucleic Acids* **27**, 839–849 (2008).
48. Kennan, A. *et al.* Identification of an IMPDH1 mutation in autosomal dominant retinitis pigmentosa (RP10) revealed following comparative microarray analysis of transcripts derived from retinas of wild-type and Rho(-/-) mice. *Hum. Mol. Genet.* **11**, 547–557 (2002).
49. Aherne, A. *et al.* On the molecular pathology of neurodegeneration in IMPDH1-based retinitis pigmentosa. *Hum. Mol. Genet.* **13**, 641–650 (2004).
50. Grover, S., Fishman, G. A. & Stone, E. M. A novel IMPDH1 mutation (Arg231Pro) in a family with a severe form of autosomal dominant retinitis pigmentosa. *Ophthalmology* **111**, 1910–1916 (2004).
51. Bowne, S. J. *et al.* Spectrum and frequency of mutations in IMPDH1 associated with autosomal dominant retinitis pigmentosa and leber congenital amaurosis. *Invest. Ophthalmol. Vis. Sci.* **47**, 34–42 (2006).
52. Plana-Bonamaisó, A. *et al.* Post-translational regulation of retinal IMPDH1 in vivo to adjust GTP synthesis to illumination conditions. *Elife* **9**, (2020).
53. Mortimer, S. E. *et al.* IMP dehydrogenase type 1 associates with polyribosomes translating rhodopsin mRNA. *J. Biol. Chem.* **283**, 36354–36360 (2008).
54. Sullivan, L. S. *et al.* Prevalence of disease-causing mutations in families with autosomal dominant retinitis pigmentosa: a screen of known genes in 200 families. *Invest. Ophthalmol. Vis. Sci.* **47**, 3052–3064 (2006).
55. Mortimer, S. E. & Hedstrom, L. Autosomal dominant retinitis pigmentosa mutations in inosine 5′-monophosphate dehydrogenase type I disrupt nucleic acid binding. *Biochem. J* **390**, 41–47 (2005).
56. Wong-Riley, M. T. T. Energy metabolism of the visual system. *Eye Brain* **2**, 99–116 (2010).
57. Country, M. W. Retinal metabolism: A comparative look at energetics in the retina. *Brain Res.* **1672**, 50–57 (2017).

58. Arshavsky, V. Y. & Burns, M. E. Photoreceptor signaling: supporting vision across a wide range of light intensities. *J. Biol. Chem.* **287**, 1620–1626 (2012).

59. Luo, D.-G., Xue, T. & Yau, K.-W. How vision begins: an odyssey. *Proc. Natl. Acad. Sci. U. S. A.* **105**, 9855–9862 (2008).

60. Palczewski, K. Chemistry and biology of the initial steps in vision: the Friedenwald lecture. *Invest. Ophthalmol. Vis. Sci.* **55**, 6651–6672 (2014).

61. Du, J., An, J., Linton, J. D., Wang, Y. & Hurley, J. B. How Excessive cGMP Impacts Metabolic Proteins in Retinas at the Onset of Degeneration. *Adv. Exp. Med. Biol.* **1074**, 289–295 (2018).

62. Charish, J. cAMP and Photoreceptor Cell Death in Retinal Degeneration. *Adv. Exp. Med. Biol.* **1185**, 301–304 (2019).

63. Spellicy, C. J. *et al.* Characterization of retinal inosine monophosphate dehydrogenase 1 in several mammalian species. *Mol. Vis.* **13**, 1866–1872 (2007).

64. Gunter, J. H. *et al.* Characterisation of inosine monophosphate dehydrogenase expression during retinal development: differences between variants and isoforms. *Int. J. Biochem. Cell Biol.* **40**, 1716–1728 (2008).

65. Andashti, B., Yazdanparast, R., Barzegari, E. & Galehdari, H. The functional impact of the C/N-terminal extensions of the mouse retinal IMPDH1 isoforms: a kinetic evaluation. *Mol. Cell. Biochem.* **465**, 155–164 (2020).

66. Andashti, B., Yazdanparast, R., Motahar, M., Barzegari, E. & Galehdari, H. Terminal Peptide Extensions Augment the Retinal IMPDH1 Catalytic Activity and Attenuate the ATP-induced Fibrillation Events. *Cell Biochem. Biophys.* **79**, 221–229 (2021).

67. Keppeke, G. D. *et al.* IMP/GTP balance modulates cytoophidium assembly and IMPDH activity. *Cell Div.* **13**, 5 (2018).

68. Xu, D. *et al.* Retinal isoforms of inosine 5′-monophosphate dehydrogenase type 1 are poor nucleic acid binding proteins. *Arch. Biochem. Biophys.* **472**, 100–104 (2008).

69. Lynch, E. M. & Kollman, J. M. Coupled structural transitions enable highly cooperative regulation of human CTPS2 filaments. *Nat. Struct. Mol. Biol.* **27**, 42–48 (2020).
70. Zhao, H. *et al.* Quantitative Analysis of Purine Nucleotides Indicates That Purinosomes Increase de Novo Purine Biosynthesis. *Journal of Biological Chemistry* vol. 290 6705–6713 (2015).
71. Hunkeler, M. *et al.* Structural basis for regulation of human acetyl-CoA carboxylase. *Nature* vol. 558 470–474 (2018).
72. Simonet, J. C., Burrell, A. L., Kollman, J. M. & Peterson, J. R. Freedom of assembly: metabolic enzymes come together. *Mol. Biol. Cell* **31**, 1201–1205 (2020).
73. Lynch, E. M. *et al.* Human CTP synthase filament structure reveals the active enzyme conformation. *Nature Structural & Molecular Biology* vol. 24 507–514 (2017).
74. Stoddard, P. R. *et al.* Polymerization in the actin ATPase clan regulates hexokinase activity in yeast. *Science* **367**, 1039–1042 (2020).
75. Hunkeler, M. *et al.* Citrate-induced acetyl-CoA carboxylase (ACC-Cit) filament at 5.4 A resolution. (2018) doi:10.2210/pdb6g2d/pdb.
76. Stearns, G., Evangelista, M., Fadool, J. M. & Brockerhoff, S. E. A mutation in the cone-specific pde6 gene causes rapid cone photoreceptor degeneration in zebrafish. *J. Neurosci.* **27**, 13866–13874 (2007).
77. Nishiwaki, Y. *et al.* Mutation of cGMP phosphodiesterase 6α′-subunit gene causes progressive degeneration of cone photoreceptors in zebrafish. *Mechanisms of Development* vol. 125 932–946 (2008).
78. Link, B. A. & Collery, R. F. Zebrafish Models of Retinal Disease. *Annu Rev Vis Sci* **1**, 125–153 (2015).
79. Baye, L. M. *et al.* The N-terminal region of centrosomal protein 290 (CEP290) restores vision in a zebrafish model of human blindness. *Hum. Mol. Genet.* **20**, 1467–1477 (2011).
80. Minegishi, Y. *et al.* CCT2 Mutations Evoke Leber Congenital Amaurosis due to Chaperone

Complex Instability. *Sci. Rep.* **6**, 33742 (2016).

81. Lessieur, E. M., Fogerty, J., Gaivin, R. J., Song, P. & Perkins, B. D. The Ciliopathy Gene ahi1 Is Required for Zebrafish Cone Photoreceptor Outer Segment Morphogenesis and Survival. *Invest. Ophthalmol. Vis. Sci.* **58**, 448–460 (2017).
82. Liu, F. *et al.* Pathogenic mutations in retinitis pigmentosa 2 predominantly result in loss of RP2 protein stability in humans and zebrafish. *J. Biol. Chem.* **292**, 6225–6239 (2017).
83. Raghupathy, R. K. *et al.* Rpgrip1 is required for rod outer segment development and ciliary protein trafficking in zebrafish. *Sci. Rep.* **7**, 16881 (2017).
84. Kettleborough, R. N. W. *et al.* A systematic genome-wide analysis of zebrafish protein-coding gene function. *Nature* **496**, 494–497 (2013).
85. Keppeke, G. D. *et al.* IMPDH forms the cytoophidium in zebrafish. *Dev. Biol.* **478**, 89–101 (2021).
86. Hutto, R. A. *et al.* Increasing Ca2+ in photoreceptor mitochondria alters metabolites, accelerates photoresponse recovery, and reveals adaptations to mitochondrial stress. *Cell Death Differ.* **27**, 1067–1085 (2020).
87. Zelinka, C. P., Sotolongo-Lopez, M. & Fadool, J. M. Targeted disruption of the endogenous zebrafish rhodopsin locus as models of rapid rod photoreceptor degeneration. *Mol. Vis.* **24**, 587–602 (2018).
88. Glesne, D. A., Collart, F. R. & Huberman, E. Regulation of IMP dehydrogenase gene expression by its end products, guanine nucleotides. *Molecular and Cellular Biology* vol. 11 5417–5425 (1991).
89. Wang, J.-S. & Kefalov, V. J. The Cone-specific visual cycle. *Progress in Retinal and Eye Research* vol. 30 115–128 (2011).
90. Hoon, M., Okawa, H., Della Santina, L. & Wong, R. O. L. Functional architecture of the retina: development and disease. *Prog. Retin. Eye Res.* **42**, 44–84 (2014).
91. Li, Y. *et al.* Integrative Analysis of Circadian Transcriptome and Metabolic Network Reveals

the Role of De Novo Purine Synthesis in Circadian Control of Cell Cycle. *PLOS Computational Biology* vol. 11 e1004086 (2015).

92. Higdon, C. W., Mitra, R. D. & Johnson, S. L. Gene Expression Analysis of Zebrafish Melanocytes, Iridophores, and Retinal Pigmented Epithelium Reveals Indicators of Biological Function and Developmental Origin. *PLoS ONE* vol. 8 e67801 (2013).
93. Gao, X. *et al.* Splice Isoforms of Phosducin-like Protein Control the Expression of Heterotrimeric G Proteins. *Journal of Biological Chemistry* vol. 288 25760–25768 (2013).
94. Murphy, D., Cieply, B., Carstens, R., Ramamurthy, V. & Stoilov, P. The Musashi 1 Controls the Splicing of Photoreceptor-Specific Exons in the Vertebrate Retina. *PLOS Genetics* vol. 12 e1006256 (2016).
95. Force, A. *et al.* Preservation of duplicate genes by complementary, degenerative mutations. *Genetics* **151**, 1531–1545 (1999).
96. Liu, Y., Beyer, A. & Aebersold, R. On the Dependency of Cellular Protein Levels on mRNA Abundance. *Cell* **165**, 535–550 (2016).
97. Papermaster, D. S., Schneider, B. G., DeFoe, D. & Besharse, J. C. Biosynthesis and vectorial transport of opsin on vesicles in retinal rod photoreceptors. *J. Histochem. Cytochem.* **34**, 5–16 (1986).
98. Sterling, P. & Matthews, G. Structure and function of ribbon synapses. *Trends in Neurosciences* vol. 28 20–29 (2005).
99. Ingram, N. T., Sampath, A. P. & Fain, G. L. Why are rods more sensitive than cones? *The Journal of Physiology* vol. 594 5415–5426 (2016).
100. Emran, F. & Dowling, J. E. Larval zebrafish turn off their photoreceptors at night. *Communicative & Integrative Biology* vol. 3 430–432 (2010).
101. Becker, M. A. & Kim, M. Regulation of purine synthesis de novo in human fibroblasts by purine nucleotides and phosphoribosylpyrophosphate. *Journal of Biological Chemistry* vol. 262 14531–14537 (1987).

102. Bowne, S. J. *et al.* Mutations in the inosine monophosphate dehydrogenase 1 gene (IMPDH1) cause the RP10 form of autosomal dominant retinitis pigmentosa. *Hum. Mol. Genet.* **11**, 559–568 (2002).
103. Kennedy, B. N. *et al.* Identification of a Zebrafish Cone Photoreceptor–Specific Promoter and Genetic Rescue of Achromatopsia in the nof Mutant. *Invest. Ophthalmol. Vis. Sci.* **48**, 522–529 (2007).
104. Mossessova, E. & Lima, C. D. Ulp1-SUMO crystal structure and genetic analysis reveal conserved interactions and a regulatory element essential for cell growth in yeast. *Mol. Cell* **5**, 865–876 (2000).
105. Volpe, D. A., Hamed, S. S. & Zhang, L. K. Use of Different Parameters and Equations for Calculation of IC50 Values in Efflux Assays: Potential Sources of Variability in IC50 Determination. *The AAPS Journal* vol. 16 172–180 (2014).
106. Suloway, C. *et al.* Fully automated, sequential tilt-series acquisition with Leginon. *J. Struct. Biol.* **167**, 11–18 (2009).
107. Zheng, S. Q. *et al.* MotionCor2: anisotropic correction of beam-induced motion for improved cryo-electron microscopy. *Nat. Methods* **14**, 331–332 (2017).
108. Zhang, K. Gctf: Real-time CTF determination and correction. *J. Struct. Biol.* **193**, 1–12 (2016).
109. Zivanov, J. *et al.* New tools for automated high-resolution cryo-EM structure determination in RELION-3. *Elife* **7**, (2018).
110. Scheres, S. H. W. RELION: implementation of a Bayesian approach to cryo-EM structure determination. *J. Struct. Biol.* **180**, 519–530 (2012).
111. Punjani, A. Algorithmic Advances in Single Particle Cryo-EM Data Processing Using CryoSPARC. *Microsc. Microanal.* **26**, 2322–2323 (2020).
112. Emsley, P., Lohkamp, B., Scott, W. G. & Cowtan, K. Features and development of Coot. *Acta Crystallogr. D Biol. Crystallogr.* **66**, 486–501 (2010).

113. Croll, T. I. ISOLDE: a physically realistic environment for model building into low-resolution electron-density maps. *Acta Crystallogr D Struct Biol* **74**, 519–530 (2018).

114. Pettersen, E. F. *et al.* UCSF Chimera--a visualization system for exploratory research and analysis. *J. Comput. Chem.* **25**, 1605–1612 (2004).

115. Adams, P. D. *et al.* PHENIX: a comprehensive Python-based system for macromolecular structure solution. *International Tables for Crystallography* 539–547 (2012) doi:10.1107/97809553602060000865.

116. Krissinel, E. & Henrick, K. Inference of macromolecular assemblies from crystalline state. *J. Mol. Biol.* **372**, 774–797 (2007).

117. D'Agati, G. *et al.* A defect in the mitochondrial protein Mpv17 underlies the transparent casper zebrafish. *Dev. Biol.* **430**, 11–17 (2017).

118. Bisbach, C. M. *et al.* Mitochondrial Calcium Uniporter (MCU) deficiency reveals an alternate path for Ca2+ uptake in photoreceptor mitochondria. *Sci. Rep.* **10**, 16041 (2020).

119. Grenell, A. *et al.* Loss of MPC1 reprograms retinal metabolism to impair visual function. *Proc. Natl. Acad. Sci. U. S. A.* **116**, 3530–3535 (2019).

120. Li, B. *et al.* Metabolic Features of Mouse and Human Retinas: Rods versus Cones, Macula versus Periphery, Retina versus RPE. *iScience* **23**, 101672 (2020).

121. Giarmarco, M. M. *et al.* Daily mitochondrial dynamics in cone photoreceptors. *Proc. Natl. Acad. Sci. U. S. A.* **117**, 28816–28827 (2020).

122. Artuso, L. *et al.* Mitochondrial DNA metabolism in early development of zebrafish (Danio rerio). *Biochim. Biophys. Acta* **1817**, 1002–1011 (2012).

123. Villefranc, J. A., Amigo, J. & Lawson, N. D. Gateway compatible vectors for analysis of gene function in the zebrafish. *Dev. Dyn.* **236**, 3077–3087 (2007).